

Progress of Particle Flow, Fluid/Solid Mechanics, and Heat Transfer in Advanced Gas/Water Nuclear Reactors

Guest Editors: Nan Gui, Xiangdong Li, and Xin Tu





**Progress of Particle Flow, Fluid/Solid
Mechanics, and Heat Transfer in Advanced
Gas/Water Nuclear Reactors**

Science and Technology of Nuclear Installations

**Progress of Particle Flow, Fluid/Solid
Mechanics, and Heat Transfer in Advanced
Gas/Water Nuclear Reactors**

Guest Editors: Nan Gui, Xiangdong Li, and Xin Tu



Copyright © 2016 Hindawi Publishing Corporation. All rights reserved.

This is a special issue published in “Science and Technology of Nuclear Installations.” All articles are open access articles distributed under the Creative Commons Attribution License, which permits unrestricted use, distribution, and reproduction in any medium, provided the original work is properly cited.

Editorial Board

Nusret Aksan, Switzerland
Won P. Baek, Republic of Korea
Stephen M. Bajorek, USA
George Bakos, Greece
Jozsef Banati, Sweden
Giovanni B. Bruna, France
Nikola Čavlina, Croatia
Leon Cizelj, Slovenia
Alejandro Clausse, Argentina
Francesco D' Auria, Italy
Marcos P. de Abreu, Brazil
Mark Deinert, USA
Giovanni Dell'Orco, France
Cesare Frepoli, USA
Michel Giot, Belgium
Valerio Giusti, Italy
Horst Glaeser, Germany
Ali Hainoun, Syria
Tim Haste, France

Keith E. Holbert, USA
Toshimitsu Homma, Japan
Yacine Kadi, Republic of Korea
Tomasz Kozlowski, USA
Tomoaki Kunugi, Japan
Mike Kuznetsov, Germany
Jérôme Lamontagne, France
Jiri Macek, Czech Republic
Annalisa Manera, USA
Borut Mavko, Slovenia
Oleg Melikhov, Russia
Rafael Miró, Spain
Jozef Misak, Czech Republic
Michio Murase, Japan
Rahim Nabbi, Germany
Michael I. Ojovan, UK
D. Paladino, Switzerland
Manmohan Pandey, India
Yuriy Parfenov, Russia

L. Podofillini, Switzerland
Yves Pontillon, France
Nik Popov, Canada
Piero Ravetto, Italy
Enrico Sartori, France
Carlo Sborchia, France
Massimo Sepielli, Italy
Arkady Serikov, Germany
James F. Stubbins, USA
Iztok Tiselj, Slovenia
Rizwan Uddin, USA
E. Ušpuras, Lithuania
Hidemasa Yamano, Japan
Yanko Yanev, Bulgaria
Enrico Zio, Italy
Massimo Zucchetti, Italy
Hyeong-Yeon Lee, Republic of Korea

Contents

Progress of Particle Flow, Fluid/Solid Mechanics, and Heat Transfer in Advanced Gas/Water Nuclear Reactors

Nan Gui, Xiangdong Li, and Xin Tu
Volume 2016, Article ID 2512634, 2 pages

Thermal Analysis for the Dense Granular Target of CIADS

Kang Chen, Yongwei Yang, and Yucui Gao
Volume 2016, Article ID 5158610, 7 pages

Numerical Investigation on Bubble Growth and Sliding Process of Subcooled Flow Boiling in Narrow Rectangular Channel

De-wen Yuan, Zejun Xiao, Deqi Chen, Yunke Zhong, Xiao Yan, Jianjun Xu, and Yanping Huang
Volume 2016, Article ID 7253907, 12 pages

Wave Characteristics of Falling Film on Inclination Plate at Moderate Reynolds Number

Chuan Lu, Sheng-Yao Jiang, and Ri-Qiang Duan
Volume 2016, Article ID 6586097, 7 pages

Parametric Investigation and Thermoeconomic Optimization of a Combined Cycle for Recovering the Waste Heat from Nuclear Closed Brayton Cycle

Lihuang Luo, Hong Gao, Chao Liu, and Xiaoxiao Xu
Volume 2016, Article ID 6790576, 12 pages

A Study on the Instantaneous Turbulent Flow Field in a 90-Degree Elbow Pipe with Circular Section

Shiming Wang, Cheng Ren, Yangfei Sun, Xingtuan Yang, and Jiyuan Tu
Volume 2016, Article ID 5265748, 8 pages

A Calculation Method for the Sloshing Impact Pressure Imposed on the Roof of a Passive Water Storage Tank of AP1000

Daogang Lu, Xiaojia Zeng, Junjie Dang, and Yu Liu
Volume 2016, Article ID 1613989, 8 pages

Assessment of Prediction Capabilities of COCOSYS and CFX Code for Simplified Containment

Jia Zhu, Xiaohui Zhang, and Xu Cheng
Volume 2016, Article ID 9542121, 8 pages

Editorial

Progress of Particle Flow, Fluid/Solid Mechanics, and Heat Transfer in Advanced Gas/Water Nuclear Reactors

Nan Gui,¹ Xiangdong Li,² and Xin Tu³

¹*Institute of Nuclear and New Energy Technology, Tsinghua University, Beijing, China*

²*School of Engineering, RMIT University, Melbourne, VIC, Australia*

³*University of Liverpool, Liverpool, UK*

Correspondence should be addressed to Nan Gui; guinan@mail.tsinghua.edu.cn

Received 14 November 2016; Accepted 15 November 2016

Copyright © 2016 Nan Gui et al. This is an open access article distributed under the Creative Commons Attribution License, which permits unrestricted use, distribution, and reproduction in any medium, provided the original work is properly cited.

Particle flow, fluid/solid mechanics, and heat transfer are very important to many technologies and applications of the advanced gas/water nuclear reactors. To better understand the relevant knowledge of particle flow, complex interactions (including multiphase thermal hydraulics), flow mechanics, and heat transfer certainly help improve the development of advanced nuclear reactors.

An introductory review of the accepted papers is presented here. In the paper entitled “A Calculation Method for the Sloshing Impact Pressure Imposed on the Roof of a Passive Water Storage Tank of AP 1000,” to estimate the impact pressure imposed on the roof of water storage tank of AP 1000, a simplified method was proposed to approximate the difference between maximum wave height and roof height as the impact pressure head. By experimental validation, this method may overpredict the impact pressure. But the error is no more than 35%. In the paper entitled “Thermal Analysis for the Dense Granular Target of CIADS,” a new concept of a dense granular spallation target is proposed for which the tungsten granules are chosen as the target material for the China Initiative Accelerator Driven Reactor System (CIADS). After being bombarded by the accelerated protons from the accelerator, the tungsten granules with high temperature flow out of the subcritical reactor and the heat is removed by the heat exchanger. In the paper entitled “A Study on the Instantaneous Turbulent Flow Field in a 90-Degree Elbow Pipe with Circular Section,” large eddy simulation was adopted to predict instantaneous flow field in the 90-degree elbow pipe. Instantaneous pressure

information and velocity field were analyzed at specific monitoring points. In the paper entitled “Wave Characteristics of Falling Film on Inclination Plate at Moderate Reynolds Number,” falling water film on an inclined plane is studied by shadowgraphy with different inclination angle and the film Reynolds number. Three distinctive regimes and three characteristic parameters of two-dimensional solitary wave pattern are examined, which are significant in engineering applications for estimation of heat and mass transfer on film flow. In the paper entitled “Parametric Investigation and Thermoeconomic Optimization of a Combined Cycle for Recovering the Waste Heat from Nuclear Closed Brayton Cycle,” a combined cycle that combines an AWM cycle with a nuclear closed Brayton cycle is proposed to recover the waste heat rejected from the pre-cooler of a nuclear closed Brayton cycle. The effects of several important parameters are investigated and the combined cycle performance is optimized based on a multiobjective function. In the paper entitled “Numerical Investigation on Bubble Growth and Sliding Process of Subcooled Flow Boiling in Narrow Rectangular Channel,” a boiling phase change model in subcooled flow boiling is proposed, and VOF model combined with phase change model is adopted to simulate the single bubble growth and movement. Finally, in the paper entitled “Assessment of Prediction Capabilities of COCOSYS and CFX Code for Simplified Containment,” the actual capability of CFX tool and COCOSYS code is assessed in prototypical geometries for simplified physical process-plume under adiabatic and convection boundary condition, respectively.

Acknowledgments

We would like to thank all the contributors of this special issue for their support and cooperation. The evaluation of paper's quality by qualified reviewers is greatly appreciated as well. The work of Nan Gui was supported under the National Natural Science Foundation of China (Grant no. 51576211).

Nan Gui
Xiangdong Li
Xin Tu

Research Article

Thermal Analysis for the Dense Granular Target of CIADS

Kang Chen,^{1,2} Yongwei Yang,¹ and Yucui Gao¹

¹*Institute of Modern Physics, Chinese Academy of Sciences, 509 Nanchang Rd., Lanzhou 730000, China*

²*University of Chinese Academy of Sciences, Beijing 100049, China*

Correspondence should be addressed to Yongwei Yang; yangyongwei@impcas.ac.cn

Received 20 June 2016; Revised 21 September 2016; Accepted 13 October 2016

Academic Editor: Xiangdong Li

Copyright © 2016 Kang Chen et al. This is an open access article distributed under the Creative Commons Attribution License, which permits unrestricted use, distribution, and reproduction in any medium, provided the original work is properly cited.

For the China Initiative Accelerator Driven System (CIADS), the energy of the protons is 250 MeV, and the current intensity will reach 10 milliamperes. A new concept of a dense granular spallation target is proposed for which the tungsten granules are chosen as the target material. After being bombarded with the accelerated protons from the accelerator, the tungsten granules with high-temperature flow out of the subcritical reactor and the heat is removed by the heat exchanger. One key issue of the target is to remove the 2.5 MW heat deposition safely. Another one is the heat exchange between the target and the subcritical reactor. Based on the model of effective thermal conductivity, a new thermal code is developed in Matlab. The new code is used to calculate the temperature field of the target area near active zone and it is partly verified by commercial CFD code Fluent. The result shows that the peak temperature of the target zone is nearly 740°C and the reactor and the target are proved to be uncoupled in thermal process.

1. Introduction

China Initiative Accelerator Driven System (CIADS) is a project proposed by Chinese Academy of Science (CAS) [1]. It consists of three subsystems: accelerator, spallation target, and subcritical reactor (Figure 1). Among them, the spallation target is responsible for generating neutrons, which are used to drive the subcritical reactor [2]. For CIADS, a new concept of spallation target is proposed which is called dense granular target [3].

In present design, the target material is a large collection of discrete tungsten (W) granules. The container for the granules is a hopper and W alloy grains flow into the spallation region under gravity from the upper annular duct where the beam pipe is located. Then a proton beam from the accelerator will interact with the flowing W grains below the pipe. The grains will pass through the spallation region quickly and discharge from the orifice of the hopper to avoid being melted down. What is more, a circuit, including a heat exchanger, grain filter, grain elevator, grain storage, and cover gas (helium) system, will guarantee the normal circulation of the working medium in the entire system.

The proton beam from the accelerator with an energy of 250 MeV and a current of 10 mA reacts with the tungsten

nuclei, and approximately 2.5 MW of heat is deposited in the target zone, which must be removed by circulating the granules. As the granules flow through the center channel of the subcritical reactor, if the target and the reactor are decoupled in heat transfer, the safety review for the spallation target can be simplified. Therefore, it is necessary to know the temperature field of the target. Furthermore, as the target and the reactor are mainly coupled by neutron near the active zone and the heat is mainly deposited there, we focus our attention on the target area near the active zone in present study (Figure 2).

Though granular material is one of the most common forms in existence, there has been no comprehensive theory that can reliably predict the behavior of such materials in technical devices [4]. The discrete element method (DEM) is now a popular method of simulating granular material but it needs a great amount of calculation to simulate the target and it can hardly calculate the temperature field. In this paper, a new thermal code based on the model of effective thermal conductivity is developed in Matlab which places smaller demands on calculation capability. The commercial CFD code Fluent is used to verify the new code. The result calculated from the new code and Fluent is nearly the same.

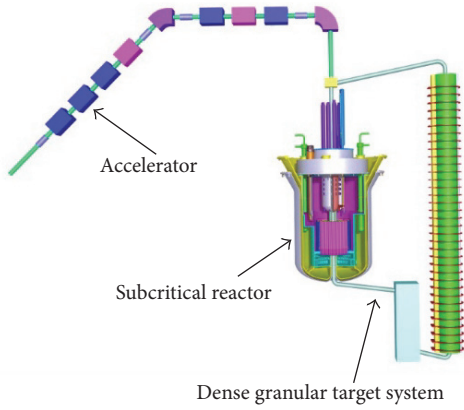


FIGURE 1: Schematic of CIADS.

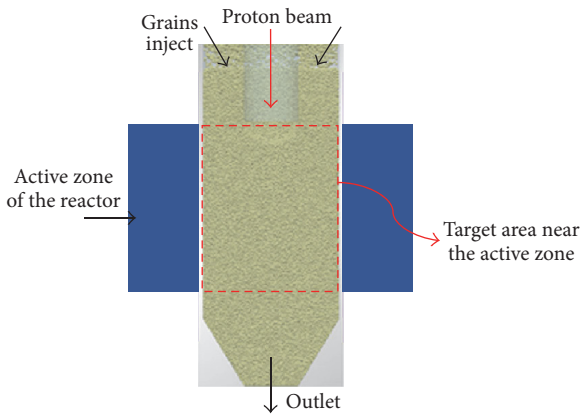


FIGURE 2: Schematic of the granular target.

Moreover, the result shows that the heat exchange between the target and the reactor can be neglected.

2. Computational Model

Concentrating on the target area near the active zone, the model is simplified to a cylinder with a diameter of 28 cm and a height of 80 cm (Figure 3). The tungsten granules flow into the spallation region with a velocity of 0.5 m/s and a temperature of 250°C. A cylinder with a radius of 14 cm and a height of 5 mm is chosen as the control volume. By tracking it, the flow of the granules can be simulated. As to the control volume, it can be seen as stagnant helium-saturated porous beds of spheres and the heat transfer in the radial direction can be calculated based on the model of effective thermal conductivity. The heat transfer in the axial direction is taken into consideration through source correction.

2.1. Governing Equations. Because of the symmetric condition, a two-dimensional model is established. The height of the control volume is set as 5 mm (Figure 4) and the time step size is set as 0.01s to match with the velocity of the granular flow. Meanwhile, the number of time steps is set as 160 to match with the height of 80 cm. By means of the first boundary condition, the effect of the reactor on the heat

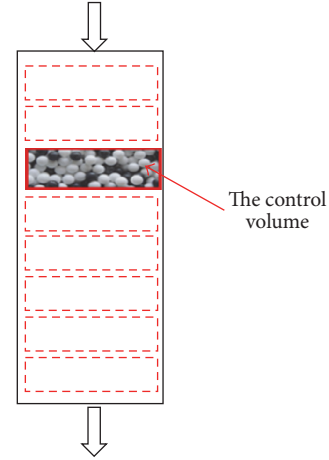


FIGURE 3: Schematic of the whole computational model.

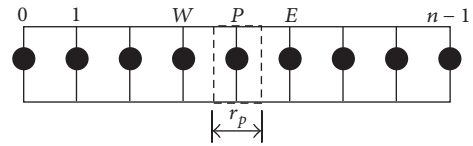


FIGURE 4: Computational model of the control volume.

transfer is taken into consideration to realize the coupling of target and reactor. The temperature field of the whole model can be obtained by putting the temperature fields of control volume at different time together depending on the relationship between time and height.

In the control volume, based on the model of effective thermal conductivity, it is simplified to be a one-dimensional transient heat conduction problem. The governing equation can be seen as follows [5]:

$$\begin{aligned} \rho c \frac{\partial T}{\partial t} &= \frac{1}{r} \frac{\partial}{\partial r} \left(\lambda r \frac{\partial T}{\partial r} \right) + S, \quad 0 < r \leq b, \\ T &= 250, \quad t = 0, \quad 0 < r \leq b, \\ T &= T_t, \quad r = b, \\ \frac{\partial T}{\partial r} &= 0, \quad r = 0, \end{aligned} \quad (1)$$

where 250°C is the designed inlet temperature, ρ is the average density, c is the average special heat capacity, λ is the effective thermal conductivity and will be explained in Section 2.2, and S is the heat source. The explicit time integration between t and $t + \Delta t$ is performed in this equation. Then, the discrete form for the equation can be obtained as follows:

$$\begin{aligned} a_p T_p^{t+\Delta t} &= a_e T_e^t + (a_p - a_e - a_w) T_p^t + a_w T_w^t + b, \\ T &= 250, \quad t = 0, \quad 0 < r \leq b, \\ T_{n-1} &= T(Y), \quad r = b, \\ T_0 &= T_1, \quad r = 0, \end{aligned} \quad (2)$$

where

$$\begin{aligned} a_p &= \frac{\rho c r_p \Delta r}{\Delta t}, \\ a_w &= \frac{\lambda r_w}{\Delta r}, \\ a_e &= \frac{\lambda r_e}{\Delta r}, \\ b &= r_p S \Delta r, \end{aligned} \quad (3)$$

and $T(Y)$ changes from 300°C to 385°C [6], which is the designed temperature of the reactor.

2.2. Effective Thermal Conductivity. The control volume can be seen as stagnant helium-saturated porous beds of spheres and there are three main processes of heat transfer in the control volume: the radiant heat transfer in the gaps, the conductive heat transfer between the tungsten granules, and the conductive heat transfer of the helium. The present research converts the practical heat transfer in porous media into equivalent heat conduction of common solid materials which satisfies the heat conduction equations, and thus it becomes a one-dimensional transient heat conduction problem.

Effective thermal conductivity is an important physical quantity describing the heat conduction in porous media. Based on a one-dimensional heat flow model for conduction through a packed bed of spherical particles, Zehner and Schlunder presented a correlation (Z-S formula) for the stagnant effective thermal conductivity [7] as follows:

$$\begin{aligned} \frac{\lambda_{eg}}{\lambda_f} &= 1 - \sqrt{1 - \varepsilon} + \frac{2\sqrt{1 - \varepsilon}}{1 - \lambda B} \left[\frac{(1 - \lambda) B}{(1 - \lambda B)^2} \ln \left(\frac{1}{\lambda B} \right) \right. \\ &\quad \left. - \frac{B + 1}{2} - \frac{B - 1}{1 - \lambda B} \right], \end{aligned} \quad (4)$$

where

$$\begin{aligned} \lambda &= \frac{\lambda_f}{\lambda_s}, \\ B &= 1.25 \left(\frac{1 - \varepsilon}{\varepsilon} \right)^{10/9}. \end{aligned} \quad (5)$$

The equations had been verified against experimental data obtained by Kladias and Bandyopadhyaya's experiment [8] in which various combinations of solid and fluid are used to produce the porous media. The stagnant thermal conductivities measured by them agreed reasonably well with the predictions made by Zehner and Schlunder as long as the conductivity ratio is not too high.

2.3. The Correction of Heat Transfer in the Axial Direction. In the previous governing equation, only the heat transfer in the radial direction is taken into consideration. To consider the axial heat transfer, the heat source is modified in every step during iteration (Figure 5). The following equation is

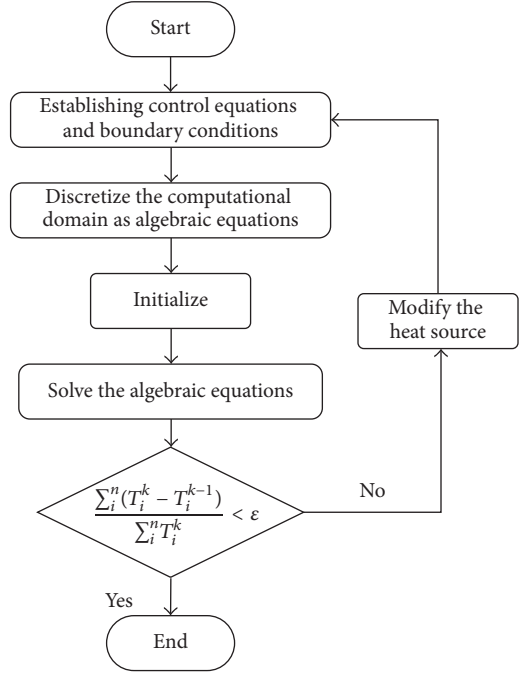


FIGURE 5: Procedure for the correction of axial heat transfer.

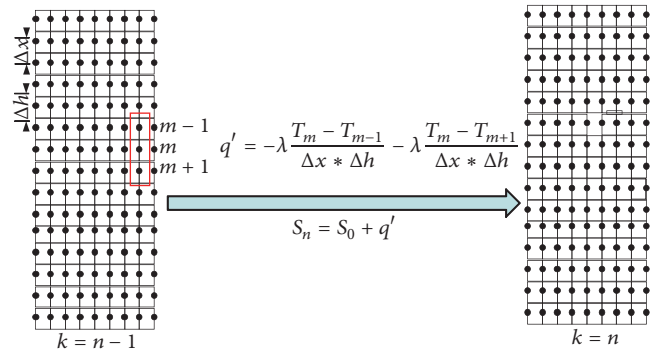


FIGURE 6: Schematic of the calculation of the axial heat transfer.

used to calculate the heat source which needs to be modified (Figure 6):

$$\begin{aligned} q &= -\lambda \frac{\Delta T}{\Delta x * \Delta h}, \\ q' &= -\lambda \frac{T_m - T_{m-1}}{\Delta x * \Delta h} - \lambda \frac{T_m - T_{m+1}}{\Delta x * \Delta h}, \\ S_n &= S_0 + q', \end{aligned} \quad (6)$$

where ΔT is the temperature difference between the same node in successive time, Δh is the height of the control volume, Δx is the distance of the same node in successive time, q' is the heat transfer to be modified, S_n is the heat source after being modified, and S_0 is the heat transfer calculated by neutronics.

2.4. Heat Deposition and Material Properties. The heat deposition is calculated by neutronics code and the proton beam

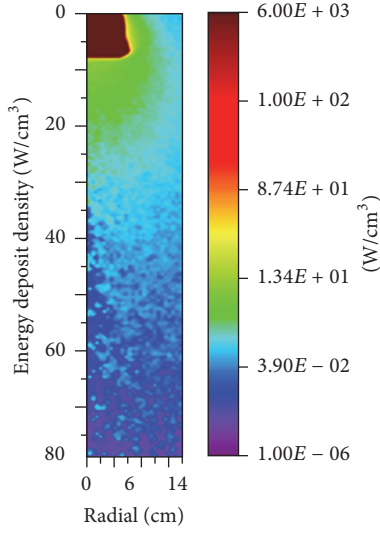


FIGURE 7: Heat deposition in the target zone.

TABLE 1: The material properties of tungsten granules and helium.

Symbol	Property	Value
d	Diameter (mm)	1
ε	Porosity	0.52
λ_h	Thermal conductivity of helium ($\text{W}\cdot\text{m}^{-1}\cdot\text{K}^{-1}$)	0.1426
ρ_h	Density of helium ($\text{Kg}\cdot\text{m}^{-3}$)	0.1785
c_h	Specific heat of helium ($\text{J}\cdot\text{Kg}^{-1}\cdot\text{K}^{-1}$)	3213.7
λ_t	Thermal conductivity of tungsten ($\text{W}\cdot\text{m}^{-1}\cdot\text{K}^{-1}$)	174
ρ_t	Density of tungsten ($\text{Kg}\cdot\text{m}^{-3}$)	19350
c_t	Specific heat of tungsten ($\text{J}\cdot\text{Kg}^{-1}\cdot\text{K}^{-1}$)	130

has a radius of 5 cm with Gaussian distribution. Figure 7 shows the energy distribution in the target zone. The maximum energy density reaches 6000 W/cm^3 , appearing near the inlet area.

The material properties of tungsten and helium are listed in Table 1.

The average special heat capacity can be calculated by the following equation:

$$c = P_t \cdot c_t + (1 - P_t) \cdot c_h, \quad (7)$$

where

$$P_t = \frac{m_t}{m}. \quad (8)$$

Inserting ε , ρ_t , c_t , ρ_h , and c_h into the equation,

$$P_t = \frac{0.52 \cdot 19350}{0.52 \cdot 19350 + 0.48 \cdot 0.1785} \approx 1. \quad (9)$$

$$c = 130 \text{ J} \cdot \text{Kg}^{-1} \cdot \text{K}^{-1}$$

The average density can be calculated by the following equation:

$$\rho = \varepsilon \cdot \rho_t + (1 - \varepsilon) \cdot \rho_h. \quad (10)$$

TABLE 2: Quantities calculated by Z-S formula.

Symbol	Definition	Value
λ	Conductivity ratio	$8.2e - 4$
λ_e	Effective thermal conductivity ($\text{W}\cdot\text{m}^{-1}\cdot\text{K}^{-1}$)	1.176



FIGURE 8: Mesh of the control volume.

Inserting ε , ρ_t , and ρ_h into the equation,

$$\rho = 0.52 \cdot 19350 + 0.48 \cdot 0.1785 = 10062 \text{ Kg} \cdot \text{m}^{-3}. \quad (11)$$

Inserting λ_h , λ_t , and ε in Z-S formula, the effective thermal conductivity of the spallation target can be calculated. The results are listed in Table 2.

3. Results and Discussion

To validate the solver in the new code, the commercial CFD code Fluent is used, in which the heat transfer in the axial direction can hardly be considered. And then, taking the axial heat transfer into consideration, the new thermal code developed in Matlab is used to calculate the temperature field of the target area near active zone. The effect of the axial heat transfer is also analyzed.

3.1. Code Validation. Neglecting the correction of the axial heat transfer, the new code and Fluent were used to calculate the temperature field of the target because in Fluent the axial heat transfer can hardly be taken into consideration. In Fluent and the new code, the same physics model is adopted.

In Fluent, the granular flow is also considered to be solid because the momentum equation for the fluid in Fluent is not suitable. The same control volume whose height is 5 mm and width is 14 cm is chosen by tracking which flow of the tungsten granules is simulated. The mesh of the control volume can be seen in Figure 8. The two-dimensional transient solver is chosen. The time step size is set as 0.01 s and the number of time steps is 160 s. The initial temperature is set as 250°C . The upper and lower boundaries are set as adiabatic. The left boundary is set as the axis and the right boundary adopts the first boundary condition. The temperature of the right boundary changes from 380°C to 300°C . Moreover, the heat deposition in Section 2.4 is imported to Fluent with the help of UDF.

The result shows that the temperature field calculated by these two codes is almost the same (Figure 9). The temperature changes greatly near the inlet area and tends to keep unchanged in the following flow because the heat source concentrates near the inlet. Moreover, the peak temperature is 740.5°C calculated by the new code and 739.5°C calculated by Fluent. The result validates the governing equations and the discretization methods in the new code.

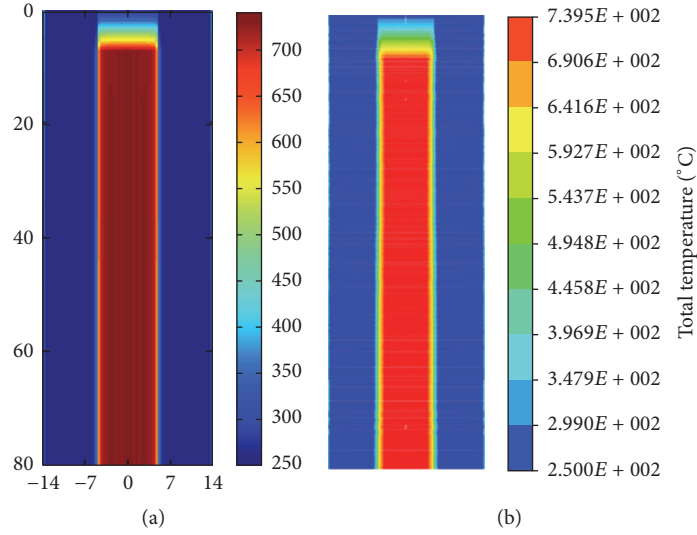


FIGURE 9: Temperature field of the target area (neglecting the axial heat transfer). ((a) is calculated by the new code and (b) is calculated by Fluent.)

TABLE 3: Iterative process of the axial heat transfer correction.

Iteration number	ee^*	δ	Peak temperature ($^{\circ}\text{C}$)
1		$1.0e - 08$	740.4897
2	$1.5748e - 05$	$1.0e - 08$	740.4912
3	$7.2384e - 08$	$1.0e - 08$	740.4913
4	$2.8562e - 11$	$1.0e - 08$	740.4913

* $ee = \sum_i^n (T_i^k - T_i^{k-1}) / \sum_i^n T_i^k$ and δ is set as $1.0e - 08$.

The average outlet temperature calculated by these two codes is 314°C . For the control volume, the average temperatures at the very beginning and the eighth second are 250°C and 314°C , respectively. To verify the heat source, the heat removed by the target is calculated by the following equation:

$$\Delta Q = c * m * \Delta T = c * \rho * \pi * r^2 * h * \Delta T. \quad (12)$$

Inserting values into the equation,

$$\begin{aligned} \Delta Q &= 130 * 10062 * 3.14 * 0.14^2 * 0.005 \\ &* (314 - 250) = 25761 \text{ J}, \end{aligned} \quad (13)$$

$$P = \frac{\Delta Q}{\Delta t} = \frac{25761}{0.01} = 2.58 \text{ MW}.$$

The result shows that the heat removed in the present model is 2.58 MW which is similar to the design index: 2.5 MW.

3.2. Temperature Field of the Target Area near the Active Zone. Considering the correction of the axial heat transfer, the new code is used to calculate temperature field of the target zone again. Figure 10 shows the new temperature field. The peak temperature is also 740.5°C and the average outlet temperature is also 314°C . Table 3 shows the iterative process

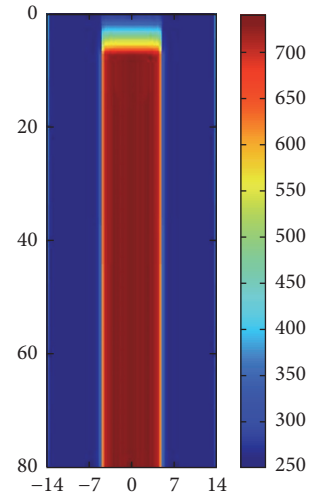


FIGURE 10: Temperature field of the target area (considering the axial heat transfer).

of the axial heat transfer correction. By 4 times of iteration, the results satisfy the demand. The results reveal that the axial heat transfer has a little effect on the temperature field. It is easy to understand because the temperature difference between successive time is small, as well as the effective thermal conductivity.

Figure 11 shows the temperature distribution in radial direction at different distance. The high-temperature zone lies in the middle of the model and the heat transferred from the reactor is limited to the boundary area, which is mainly due to the low effective thermal conductivity. And thus, it reveals that the reactor and the target are uncoupled in thermal process.

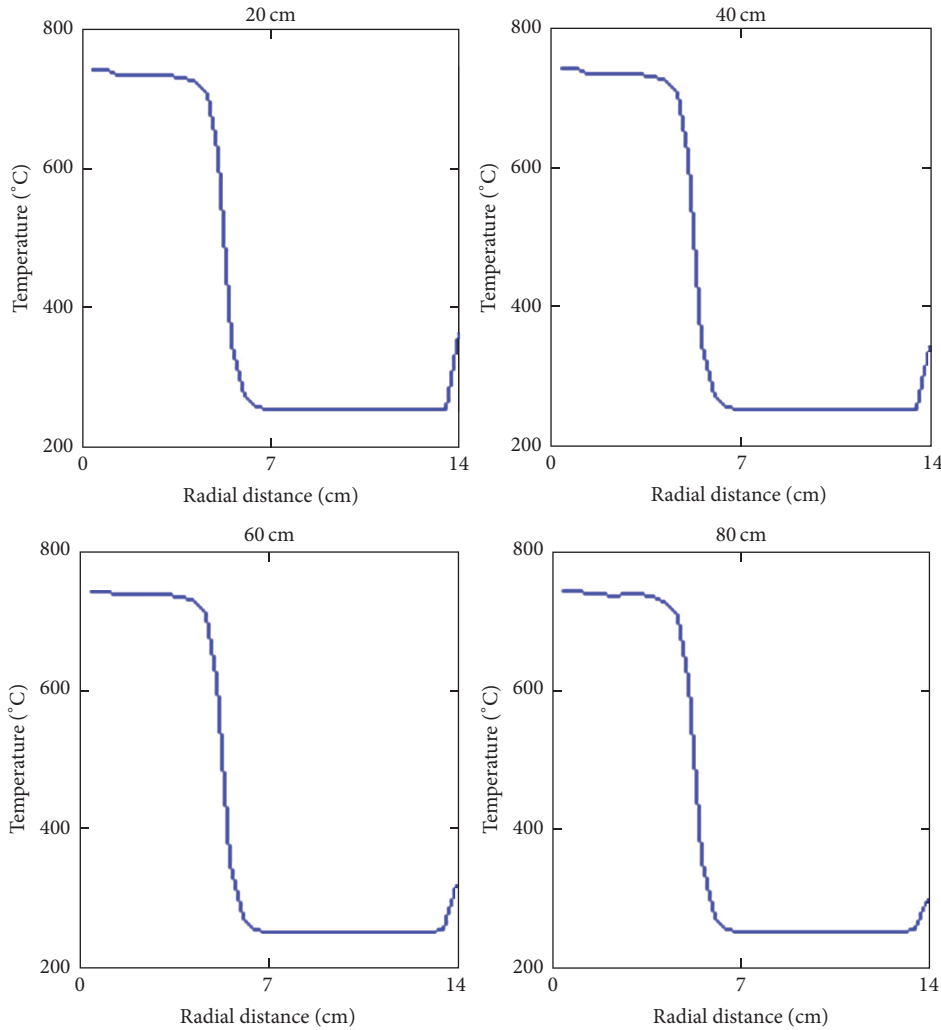


FIGURE 11: Temperature distribution in radial direction at 20 cm, 40 cm, 60 cm, and 80 cm.

4. Conclusions and Perspective

The dense granular target is a new concept for a high-power spallation target. In present work, a new thermal code based on the effective thermal conductivity model is developed to simulate its temperature field.

- (i) Neglecting the axial heat transfer correction, the solver of the new code is validated by Fluent.
- (ii) The target can remove 2.58 MW heat deposition with the peak temperature 740°C.
- (iii) The axial heat transfer has a little effect on the temperature field.
- (iv) The heat deposition in the target can hardly be transferred to the subcritical reactor and the heat transferred from the reactor is limited to the boundary area of the target, which means that the heat exchange between the target and the reactor can be neglected.

More work needs to be done in the following studies:

- (i) Experiment could be carried out to measure the stagnant thermal conductivity of helium-saturated porous beds of tungsten granules. Zhao and Yao [9] have done some similar experiments to measure the stagnant thermal conductivity of porous beds, which shows that the experiment may not be very complex or expensive.
- (ii) The whole target can be taken into consideration, not only the area near active zone.

Competing Interests

There is no conflict of interests regarding the publication of this paper.

Acknowledgments

This work is financially supported by the “Strategic Priority Research Program” of Chinese Academy of Sciences (Grant no. XDA03030102).

References

- [1] W. Zhan and H. Xu, “advanced fission energy program—ads transmutation system,” *Bulletin of the Chinese Academy of Sciences*, vol. 27, no. 3, pp. 375–380, 2012.
- [2] T. V. Dury, “CFD design support at PSI for the international MEGAPIE liquid-metal spallation target,” *Journal of Nuclear Science and Technology*, vol. 41, no. 3, pp. 285–295, 2004.
- [3] L. Yang and W. Zhan, “New concept for ADS spallation target: gravity-driven dense granular flow target,” *Science China Technological Sciences*, vol. 58, no. 10, pp. 1705–1711, 2015.
- [4] P. G. De Gennes, “Granular matter: a tentative view,” *Reviews of Modern Physics*, vol. 71, no. 2, pp. S374–S382, 1999.
- [5] W. Q. Tao, *Numerical Heat Transfer*, Xi’an Jiaotong University Press, Xi’an, China, 2013 (Chinese).
- [6] H. Chen, Z. Chen, T. Zhou et al., “Preliminary thermal-hydraulic design and analysis of china lead alloy cooled research reactor (clear-i),” in *Proceedings of the 9th International Topical Meeting on Nuclear Thermal-hydraulics Fr13, Operation and Safety [nuthos-9]*, Kaohsiung, Taiwan, 2012.
- [7] P. Zehner and E. U. Schlunder, “Thermal conductivity of granular materials at moderate temperatures,” *Chemie Ingenieur Technik*, vol. 42, pp. 933–941, 1970 (German).
- [8] V. Prasad, N. Kladas, A. Bandyopadhyaya, and Q. Tian, “Evaluation of correlations for stagnant thermal conductivity of liquid-saturated porous beds of spheres,” *International Journal of Heat and Mass Transfer*, vol. 32, no. 9, pp. 1793–1796, 1989.
- [9] X. L. Zhao and S. Yao, *The Research of Effective Conductivity in the Porous Media*, Dalian University of Technology, Dalian, China, 2009.

Research Article

Numerical Investigation on Bubble Growth and Sliding Process of Subcooled Flow Boiling in Narrow Rectangular Channel

De-wen Yuan,¹ Zejun Xiao,¹ Deqi Chen,² Yunke Zhong,² Xiao Yan,¹
Jianjun Xu,¹ and Yanping Huang¹

¹CNNC Key Laboratory on Nuclear Reactor Thermal Hydraulics Technology, Nuclear Power Institute of China, Chengdu 610041, China

²Key Laboratory of Low-Grade Energy Utilization Technologies and Systems, Chongqing University, Chongqing 400044, China

Correspondence should be addressed to De-wen Yuan; yuandewen2002@sina.com and Deqi Chen; chendeqi@cqu.edu.cn

Received 17 April 2016; Revised 23 June 2016; Accepted 25 July 2016

Academic Editor: Xiangdong Li

Copyright © 2016 De-wen Yuan et al. This is an open access article distributed under the Creative Commons Attribution License, which permits unrestricted use, distribution, and reproduction in any medium, provided the original work is properly cited.

In order to investigate single bubble evolution, a boiling phase change model in subcooled flow boiling is proposed in this paper, and VOF model combined with phase change model is adopted to simulate the single bubble growth and movement. The effects of flow velocity, liquid subcooling, wall superheat, and vapor-liquid contact angle are considered in this model. The predicted bubble growth curve agrees well with the experimental result. Based on the analysis of bubble shape evolution and temperature field, it is found that the average bubble growth rate, flow velocity, and dynamic contact angle have significant effect on the bubble shape evolution during the bubble growth and movement while the temperature gradient in superheated liquid does not change with bubble growing. The character of dynamic contact angle during bubble growth and movement is also obtained in different working condition.

1. Introduction

In order to understand and optimize the process of boiling heat transfer, it is vital to understand the mechanism of bubble nucleation, growth, and departure. As a complex process, the investigation of model for bubble formation and disappearance has gotten only limited success. In recent years, there are some investigations about single bubble growth model for nucleate boiling.

Many researches about the bubble growth have been done using numerical methods, such as Mei et al. [1], Welch [2], and Heo et al. [3]. Mei et al. [1] have performed a numerical analysis to study the bubble growth under the condition of saturated heterogeneous boiling. The simultaneous energy transfer between vapor bubble and liquid micro-layer or heating wall was considered having effects on the bubble growth. Welch [2] carried out a study on the growth of axis-symmetric vapor bubble. The moving unstructured grid was considered by using the interface tracking method with the combination of the finite volume method. The control volume continuity, momentum, and energy equations were modified to include

surface tension and discontinuous pressure and velocity. The flow-directional local grid (MPS-MAFL) method has been used by Heo et al. [3] to do the numerical study about the growth of bubble in transient pool boiling through moving particle semi-implicit with meshless advection. The growth process of a bubble with different initial radii was calculated under the condition of high heat flux and high subcooling condition.

Besides, some new models were used to study the bubble growth. A new understanding was provided by Li et al. [4] to study the bubble which was about the interfacial transport characteristics of inviscid spherical bubble with different geometric parameters, rising in a stagnant hot or bisolution liquid. The flow and temperature fields around bubbles and similarly sized rigid spheroids were computed numerically while the development of the physical model for vapor bubble growth in the condition of saturated boiling was provided by Liao et al. [5], including heat transfer through the micro-layer and the surrounding foam body superheated liquid and bubble growth. Both asymptotic and numerical methods were carried out to study the liquid temperature

field surrounding a hemispherical bubble and it indicated that there was a thin unsteady thermal boundary layer existing adjacent to the bubble dome. During the early stages of bubble growth, heat transfer to the bubble dome through the unsteady thermal boundary layer constituted a substantial contribution to vapor bubble growth.

The region around a single growing bubble was considered to be subdivided into three subregions by Genske and Stephan [6], which were micro-region, bubble area, and surrounding liquid. Their results showed that the flow pattern in the liquid around a growing vapor bubble was determined by not only the movement of the bubble surface, but also the vapor flow that fled inside the bubble. Heat conduction would be the dominant factor on the bubble growth in the regions away from the bubble. Except that, the contact angle has effects on bubble growing. A static contact angle model and a dynamic contact angle model were proposed by Mukherjee and Kandlikar [7], which were based on the contact line velocity and the sign of the contact line velocity which was used to sign the dynamic contact angle model on the heating wall. The effects of dynamic contact angle on bubble dynamics and vapor volume growth rate were compared with results obtained with the static contact angle model.

The heterogeneous boiling on a horizontal plate in stagnant and slowly flowing fluid was simulated by Hazi and Markus [8] by using the method of lattice-Boltzmann approach. The study has found that, in a stagnant fluid, the bubble departure diameter was proportional to $g^{1/2}$ while the release frequency scales with $g^{3/4}$ where g was the gravitational acceleration. According to the simulation results, it is found that there was no correlation between the bubble departure diameter and the static contact angle, but with the increase of the static contact angle, the release frequency increases exponentially.

Numerical researches about bubble growth are mostly based on the pool boiling. However, the character of bubble growth in subcooled flow boiling is quite different from that of the pool boiling. The bubble growth process in subcooled flow boiling is affected by the thermal characteristics of heating wall and mainstream liquid and so forth. Due to the existence of the mainstream liquid velocity, the motion characteristic of bubble interface and the flow field around the bubble are more complex than those of pool boiling. Thus, distortion and deformation of the bubble may occur which will lead to characterized features during the growth.

In the present paper, based on the characteristic of bubble growth process in subcooled flow boiling, a bubble growth model is proposed and a numerical simulation is performed to understand the process of bubble growth. The simulation results reflect bubble growth process as well as a dynamic result of evaporation and condensation which agree the experimental results very well and the relationship between the vapor-liquid interface motion and velocity field inside the bubble presented here. The character of dynamic contact angle during bubble growth and movement process is also obtained in different working condition.

2. Numerical Simulation Methods

The VOF formulation relies on the fact that two or more fluids (or phases) are not interpenetrating. For each additional phase that was added to model, a variable is introduced: the volume fraction of the phase in the computational cell. In each control volume, the volume fractions of all phases sum to unity. The fields for all variables and properties are shared by the phases and represent volume-averaged values, as long as the volume fraction of each of the phases is known at each location. This paper investigates the bubble growth process by VOF model [9, 10] and UDF interface of the CFD software Fluent.

2.1. VOF Model. Generally, a VOF algorithm [10] solves the problem of updating the phase volume fraction field given the fixed grid, the velocity field, and the phase volume fraction are determined in previous time step. In two-dimensional problem, the interface is considered to be a continuous and piecewise smooth line. The problem is reduced to the reconstruction of an approximation of the interface in each cell, knowing only the volume fraction of each phase in the cell itself and in the neighboring cells.

During all simulation cases in present work, a piecewise linear interface calculation (PLIC) [12] interface reconstruction method has been used for interpolation in a cell. In the existing CFD code, this scheme is the most accurate one and it is applicable for general unstructured meshes as used here; this interpolation scheme assumes that the interface between two fluids has a linear slope within each cell and this linear shape is used for the calculation of the advection of the fluid through the cell interfaces.

In VOF model, the k th fluid's volume fraction in the cell is denoted as α_k and then the following three conditions are possible:

$\alpha_k = 0$: the cell does not contain the k th fluid;

$\alpha_k = 1$: the cell is full of the k th fluid;

$0 < \alpha_k < 1$: the cell contains the interface between the k th fluid and one or more other fluids.

In present model, there are two phases: vapor and liquid. When $\alpha_v = 1$, it represents vapor bubble region; when $\alpha_l = 1$, it is liquid region. When $0 < \alpha_v < 1$, $0 < \alpha_l < 1$, there is a bubble interface existing in this region. Based on the local value of α_k , the appropriate properties and variables will be assigned to each control volume within the domain.

2.1.1. Continuity Equation. In VOF model, the volume fraction of each fluid α_k is calculated by tracking the interface between different phases throughout the solution domain. Tracking of the interfaces between different phases present in the system is accomplished by solving continuity equations of the phase volume fraction for phases. A physical interpretation can be given by various terms in this continuity equation. For the vapor phase, this equation has the following form:

$$\frac{\partial \alpha_q}{\partial t} + \vec{u} \cdot \nabla \alpha_q = \frac{S_{m,q}}{\rho_q}, \quad (1)$$

where $S_{m,q}$ is the mass source term of vapor in the bubble growth process, which can be estimated by (8) and (10) through the UDF interface.

2.1.2. Momentum Equations

$$\frac{\partial}{\partial t} (\rho \vec{u}) + \nabla \cdot (\rho \vec{u} \vec{u}) = -\nabla p + \nabla \cdot [\mu (\nabla \vec{u} + \nabla \vec{u}^T)] + \rho \vec{g} + \vec{F}, \quad (2)$$

where \vec{F} is the surface tension force, which can be estimated through CSF (continuum surface force) model [13] as follows:

$$\vec{F} = \sigma \frac{\rho \kappa_i \nabla \alpha_i}{(1/2)(\rho_i + \rho_j)}. \quad (3)$$

2.1.3. Energy Equation

$$\frac{\partial}{\partial t} (\rho E) + \nabla \cdot (\vec{u} (\rho E + p)) = \nabla \cdot (\lambda \nabla T) + S_{E,q}. \quad (4)$$

The physical properties of ρ and λ (effective thermal conductivity) are shared by both of the two phases. Source term S'_v contains contributions from all other volumetric heat sources.

2.1.4. Vapor-Liquid Interfacial Density. The properties appearing in the transport equations are determined by the presence of the component phases in each control volume [9]. In a two-phase system, for example, if the phases are represented by the vapor and liquid and if the volume fraction of the second phase has been tracked, the density in each cell would be given by

$$\rho = \alpha \rho_l + (1 - \alpha) \rho_v. \quad (5)$$

2.2. UDF Procedures. The User Defined Functions (UDF) interface of the commercial CFD code of Fluent [9] is employed to simulate the heat and mass transfer of the phase change. UDF subroutine allows us to customize Fluent to fit particular modeling needs. UDF is a function that user program can be dynamically loaded with the Fluent solver to enhance the standard features of the code. They are defined by DEFINE macros which are supplied by Fluent Inc. They can access data from the Fluent solver using predefined macros and functions. Present UDF programs are based on following described bubble generation theories of micro-layer evaporation to simulate the bubble growth.

3. Bubble Growth Physical Models in Subcooled Flow Boiling

3.1. Bubbles Growth Process in Subcooled Flow Boiling. Figure 1 shows the schematic diagram of bubble growth process on heating wall in subcooled flow boiling. The channel is vertically arranged, and the fluid flows vertically from bottom

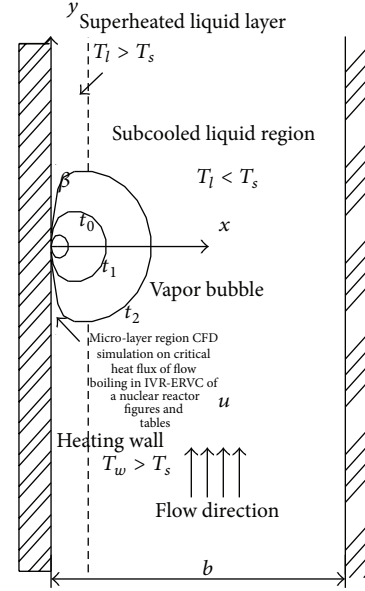


FIGURE 1: Schematic diagram of bubble growth model.

in y -direction. The temperature of the mainstream region T_l is lower than that of the liquid saturation temperature T_s corresponding to local pressure. T_w is the temperature of single-side heated wall which is higher than T_s . There is a temperature boundary layer close to heating wall. In this region, the liquid temperature is higher than saturation temperature but lower than the heating wall temperature, that is, $T_s < T_l < T_w$. There is a liquid micro-layer region near the bottom of bubble whose temperature is higher than T_s . β is the contact angle of the bubble with the heating wall. The growth times sequence of bubble is t_0 , t_1 , and t_2 .

At the initial time, t_0 , bubble radius is relatively small. The whole bubble is submerged in superheating liquid layer. The heat and mass supplied for bubble growth are derived from the liquid micro-layer evaporation at the bottom of bubble and superheating liquid around bubble surface. As the bubble diameter increases, at the time of t_1 , the top of bubble passes through the superheating boundary layer and enters the subcooled mainstream region. Consequently, the condensation will occur at the top of the bubble. At this period, as the mass into the bubble caused by evaporation at the bottom and the interface exceeds the condensation mass at the bubble top, the bubble continues to grow up. At the time of t_2 , the bubble diameter is greatly larger. Because a large portion of bubble top region is submerged in subcooled mainstream liquid, condensation effect becomes significant and bubble growth rate will be gradually slow. When the condensation mass of vapor is approximately equivalent to the mass added to the bubble by evaporation at the bottom and the interface, the bubble growth rate will slow down to zero and bubble diameter remains unchanged.

3.2. Bubble Growth Model. Based on above analysis, there are four assumptions in current model: (i) there is a very small initial bubble existing on the heating wall in which

the radii will be estimated through classic bubble nucleation theory; (ii) the vapor in the growing bubble is ideal gas; (iii) the temperature at the initial bubble growth time is equal to saturation temperature T_s corresponding to the working pressure; (iv) the pressure in the initial bubble is based on Young-Laplace equation:

$$p_v = p_l + \frac{2\sigma}{r}, \quad (6)$$

where σ is surface tension coefficient, N/m.

3.2.1. Micro-Layer Liquid Evaporation Model on the Bottom of Growing Bubble. Experimental results [14] showed that there is a liquid micro-layer existing at the bottom of bubble during bubble growth, and it is very important to the process. The convective heat transfer through this layer can be ignored due to its small thickness. Thus, the heat flux through the micro-layer liquid can be estimated as

$$q = \lambda \frac{T_w - T_v}{\delta}, \quad (7)$$

where λ is the thermal conductivity of the liquid, W/(m·K); T_w is the temperature of the heating wall, K; T_v is the vapor temperature of growing bubble, K; δ is the micro-layer thickness under the bubble bottom, m.

The micro-layer thickness for growing bubble on nucleation site was calculated by [15]

$$\delta = \frac{\pi}{8\sqrt{3}} \frac{\rho_v h_{fg} d}{\rho_l c_{pl} \Delta T_w} \text{Pr}^{1/2}, \quad (8)$$

where ρ_v is vapor density, kg/m³; h_{fg} is latent heat of vaporization, kJ/kg; c_{pl} is the specific heat at constant pressure, kJ/(kg·K); ρ_l is liquid density, kg/m³; ΔT_w is wall superheated, K; d is bubble diameter, m; Pr is the liquid Prandtl number.

The micro-layer thickness for sliding bubble on nucleation site was calculated by [16]

$$\delta = 1.3 \left(\frac{\nu_l H}{u} \right)^{1/2}, \quad (9)$$

where ν_l is liquid dynamic viscosity, m²/s; H is the height of sliding bubble, m; u is the velocity of bubble slide, m/s.

The mass transferring from the micro-liquid layer to vapor bubble can be estimated by

$$G = \frac{q}{h_{fg}}, \quad (10)$$

where h_{fg} is the latent heat, kJ/kg; q is the heat flux through the micro-layer, kW/m². G is the net mass flow rate per unit area, kg/(m²·s).

Because Fluent is the CFD software which is based on the FVM (finite volume method), the mass source which is added to the continuity equation is the mass flow rate per volume, kg/(m³·s),

$$m_j = \frac{\alpha_v S_j}{\sum_j \alpha_v \times V_j} G, \quad (11)$$

where m_j is the mass transfer rate proportional to vapor bubble volume fraction in the j th cell of vapor-liquid interface region. S_j is the area of the j th grid. V_j is the volume of the j th grid.

3.2.2. Interfacial Bubble Heat and Mass Transfer Model. Vapor-liquid interface is quite important for bubble growth. When the radius of bubble is relatively small, the whole bubble is submerged in superheated liquid layer. Heat will transfer to bubble from the superheated liquids through the bubble interface, and the diameter will be increased consequently. When the diameter of bubble increases to a certain scale, the bubble interfacial area will be divided into two parts; one is submerged in the superheated liquid layer where the heat would be transferred from the superheated liquid to the bubble; the other one is submerged in subcooled liquid where the vapor in the top of bubble would be condensed and the heat would be transferred from bubble to the subcooled liquid through the interfacial areas.

According to classical analysis of the evaporation and condensation [15], the net mass flux at the phases interface could be estimated by Hertz-Knudsen-Schrage Equation [16]:

$$G = \frac{2}{2 - \sigma_c} \sqrt{\frac{M}{2\pi R}} \left(\sigma_e \frac{p_s(T_l)}{\sqrt{T_l}} - \sigma_c \frac{p_v}{\sqrt{T_v}} \right), \quad (12)$$

where G is the net mass flow rate per unit area, kg/(m²·s); R is the universal gas constant, J/(mol·K); M is the mass per mole, (kg/mol); T_l is the liquid temperature of the vapor-liquid interface, K; p_s is the saturation liquid pressure corresponding to T_l , Pa; T_v is the vapor temperature within bubble, K; p_v is the vapor pressure in the growing bubble, σ_e is the evaporation coefficient of the vapor-liquid interface, and σ_c is the condensation coefficient of the vapor-liquid interface, respectively.

Under the conditions of thermodynamic equilibrium, the mass transfer mechanism representing evaporation coefficient will be not distinguished from the ones of the condensation coefficient; and ones often have the simplification of $\sigma_e = \sigma_c$ [17]. For a curved interface, an analogous equation can be deduced [18–20]:

$$G = \frac{4\sigma_e}{4 - 3\sigma_e} \sqrt{\frac{M}{2\pi R}} \left(\frac{p_s(T_l)}{\sqrt{T_l}} - \frac{p_v}{\sqrt{T_v}} \right). \quad (13)$$

When $G > 0$, the net mass from liquid will enter into the bubble through the vapor-liquid interface; when $G < 0$, the net mass from bubble will enter into the liquid through the interface.

The heat flux due to the phase change in the j th cell of vapor-liquid interface region can be defined by

$$q_j = m_j \cdot h_{fg}. \quad (14)$$

It should be known that m_j is the mass source term of the continuity equation and the heat flux q is the energy source term of the energy equation according to VOF model, W/m³.

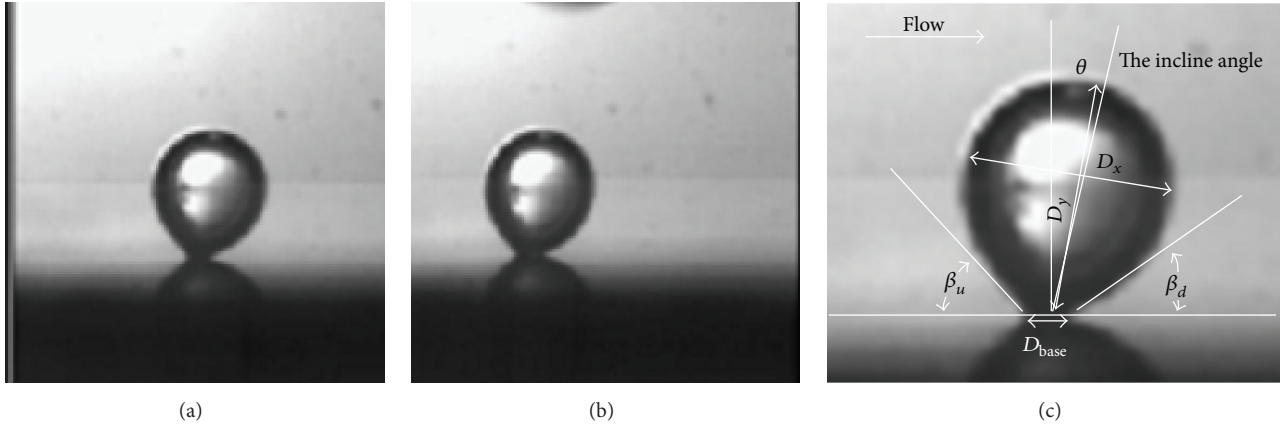


FIGURE 2: Dynamic contact angle at bubble base during flow boiling [23].

3.2.3. The Dynamic Contact Angle Model. The three-phase moving contact line is a fundamental problem in multiphase flow. A material contact angle (given by Young's equation) can be defined at a position microscopically close to the contact line. Due to the hysteresis, there are many stable contact angles for a given system, of which the largest is called the advancing angle and the smallest the receding angle. When the contact line is moving, the dynamic contact angle differs from its equilibrium counterpart and can be beyond the range limited by the static advancing and receding angles β_{re} . The apparent contact angle is generally used as an auxiliary concept in studying the contact line dynamics, which is the angle formed between the wall and a line tangent to the interface at a certain distance from the apparent contact line.

Contact angle is important for flow boiling, including static contact angle and dynamic contact angle. The static contact angle reflects wetting property of fluid. When one fluid on the wall was displaced by another, the relationship between the contact angle and wet property becomes very complex due to the contact angle hysteresis phenomenon, this time the contact angle named dynamic angle, which was influenced by fluid property, wall property, and the velocity of three-phase moving contact line. The contact angle was continued to be studied, while there are still no certain correlations for analysis [21–23].

Dynamic contact angle at bubble base during nucleate pool boiling was discussed in many present papers, while dynamic contact angle in the flow boiling was less studied. Because of the quasi-steady drag in the flow direction and buoyancy force, the character dynamic contact angle in flow boiling is very different from that in pool boiling. Figure 2 shows the dynamic contact angle in flow boiling. β_u and β_d were the dynamic contact angles of bubble behavior on the flow boiling [24]; θ was the incline angle. In bubble detachment heating wall, the contact area at bottom of growing bubble reduces and the three-phase contact line moves towards vapor phase, the contact angle named advancing contact angle, $\beta_u = \beta_d$, while it can be seen that the receding contact angle and advancing contact angle at different time are $\beta_u \neq \beta_d$ in the flow boiling system.

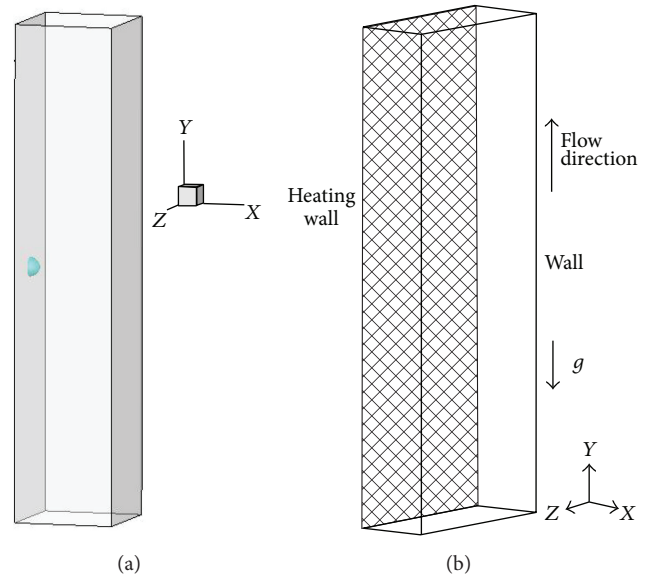


FIGURE 3: Schematic of the mesh structure.

3.3. Geometry, Boundary Conditions, and Working Conditions.

In present work, a single bubble growth process has been simulated in subcooled flow boiling in a narrow channel. Due to the symmetrical characteristic in the wide side of the bubbles, it can be simplified to a three-dimensional geometry structure Figure 3(a). In the simulation geometry structure model, the vertical rectangular narrow channel has an inlet section of $2 \text{ mm} \times 2 \text{ mm}$ and a length of $L = 10 \text{ mm}$.

Based on the assumption of the bubble growth model, there is a small bubble on heating wall at the initial stage of the simulation. The diameter of the small bubble is calculated by the Han and Griffith correlation equation [11]

$$r_{\min} = \frac{\delta(T_w - T_s)}{3(T_w - T_l)} \left[1 - \sqrt{1 - \frac{12(T_w - T_l)\sigma T_s}{\delta(T_w - T_s)^2 h_{fg} \rho_v}} \right]. \quad (15)$$

TABLE 1: Typical working condition.

Case number	Pressure/MPa	Bulk velocity $u/\text{m}\cdot\text{s}^{-1}$	Wall superheated $\Delta T_w/\text{K}$	Subcooling $\Delta T_{\text{sub}}/\text{K}$	Dynamic contact angle $\beta_{\text{re}}/\beta_{\text{ad}}(^{\circ})$
1	0.1	0.05	10	10	70/35
2	0.1	0.05	10	20	70/35
3	0.1	0.1	15	20	70/45
4	0.1	0.1	10	5	65/25
5	0.6	0.17	6	20	65/15

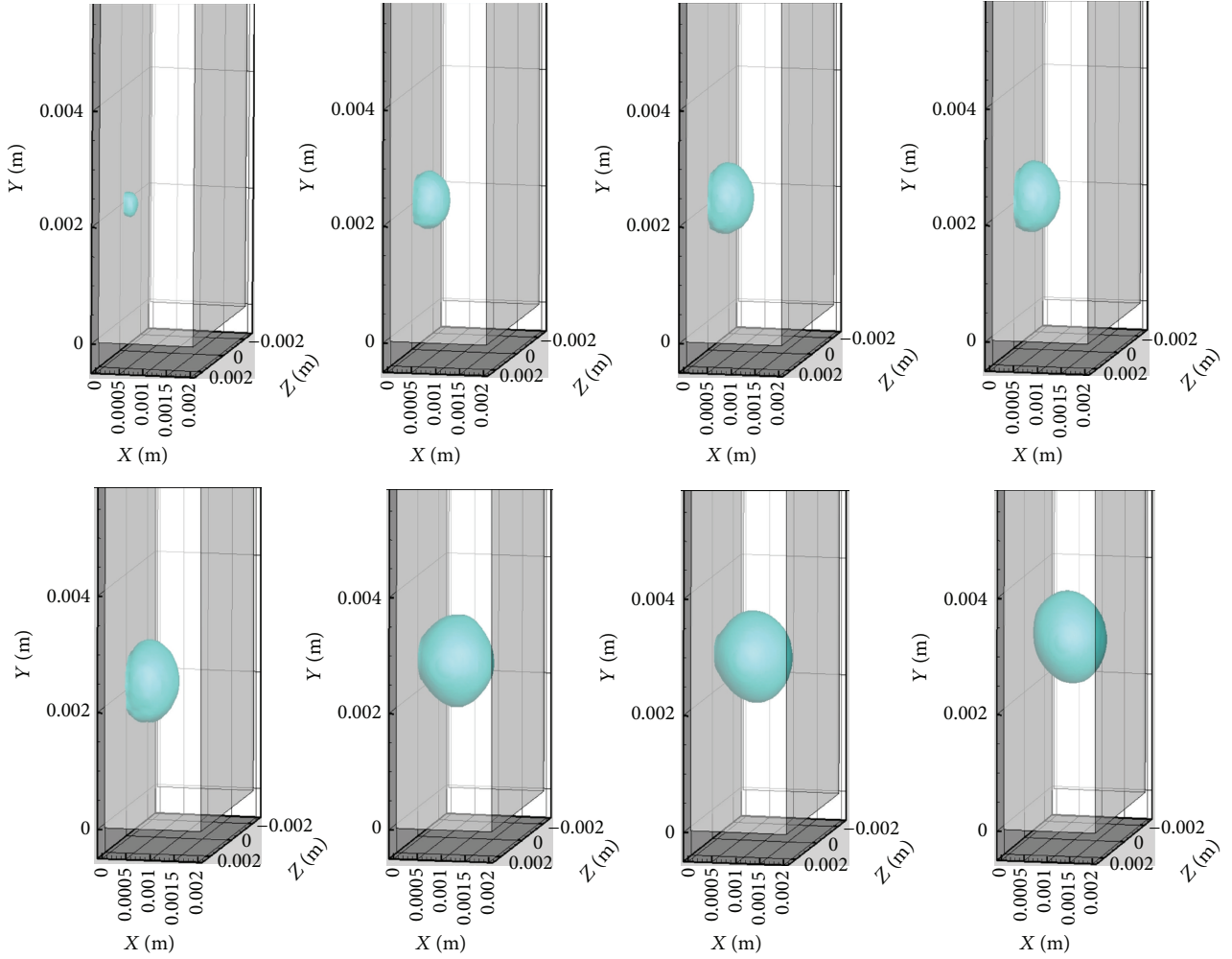


FIGURE 4: The evolution of bubble shape in bubble growth and detachment process on case 1.

In this paper, r_{min} is ranged from $20\ \mu\text{m}$ to $50\ \mu\text{m}$ in the subcooled flow boiling.

Mesh around the bubble has been refined to obtain the details of bubble growth; Figure 3(b) shows the mesh through the center of bubble in XY plane. According to mesh sensitivity testing, the number of meshes (120000) is suitable for simulation. The heating wall temperature keeps constant while the other wall is adiabatic. The inlet of the channel is set as velocity-inlet condition, and the outlet is set as pressure-outlet condition. The viscous model is the laminar model. Table 1 is the working conditions as flowing.

4. Results and Discussion

4.1. Bubble Growth Process

4.1.1. Bubble Shape Evolution during Bubble Growth and Detachment Process. The evolution of bubble shape in subcooled flow boiling would be impacted by a couple of factors. Figure 4 shows the evolution process on case 1. Figure 5(a) is the curve of bubble diameter in the time of bubble growth and detachment. Figure 5(b) is the comparison of simulation results with experimental results obtained by Chen et al.

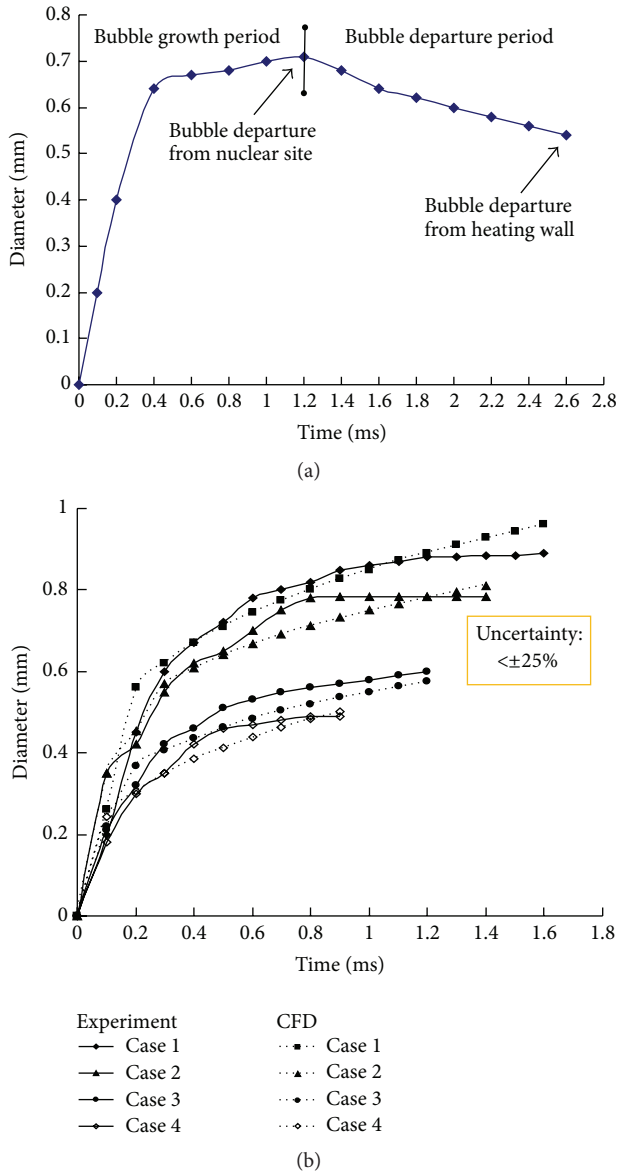


FIGURE 5: (a) The bubble diameter in bubble growth and detachment process on case 1. (b) Comparison between simulation and experimental results of bubble grow cures.

[25], and it is found that the bubble growth curves based on CFD simulation agree well with the experimental results with uncertainty less than $\pm 25\%$. Figure 6 is typical images of bubble shape in bubble growth and detachment process in forced convective subcooled flow boiling [26].

As shown in Figure 4, there is a growing bubble at the nucleation site on the heating wall. The nucleation site coordinates are $x = 0.0$ m, $y = 0.005$ m. At the initial time of bubble growth (0.1–0.4 ms), due to high pressure in the bubble, bubble growth is in the stage of inertial control. A large amount of heat and mass is transferred from the micro-layer to the bubble. The bubble grows fast as a hemisphere. The value of bubble diameter increases from 0.2 mm to 0.54 mm. After 0.4 ms, the pressure inside bubble

decreases quickly; bubble growth in the stage is the thermal diffusion control. As the condensation intensity gradually enhances at the top of bubble, bubble growth rate becomes much slower than that of the former. From 0.6 ms to 0.8 ms, bubble expands slowly in hemisphere shape. However, with increased bubble diameter, the force balance acting on the growing bubble has been broken. As a result, the shape of bubble evolves from a hemisphere to an ellipse at the time of $t = 1.0$ ms. At $t = 1.2$ ms, bubble diameter increases to the maximum value 0.71 mm. After that bubble begins to detach from nucleation point. From 1.2 ms to 2.6 ms, the shape of bubble evolves from ellipse to sphere and bubble diameter decreased gradually. Bubble remains as a rough sphere until it lifts off from the heating wall.

4.1.2. *Pressure Distribution Evolution during Bubble Growth.* Figure 7 is the pressure distribution of bubble growth at 0.4 ms and 1.0 ms on case 1. As shown in Figure 6, in the bubble growth process, the pressure is identical in different regions inside vapor bubble. The pressure inside the bubble is higher than that of the flow liquid around the bubble. Farther away from the bubble, the pressure of the flow liquid becomes much higher. At $t = 0.4$ ms, the value of gauge pressure inside bubble is 1930 Pa. Away from the top of bubble, there is a flow liquid region with the minimum pressure, whose gauge pressure value is 1880 Pa. At $t = 1.0$ ms, the value of gauge pressure inside bubble is 1539 Pa. The minimum pressure of flow liquid region is at the two sides of the growing bubble.

Figure 8 presents the pressure evolution inside a bubble during bubble growth and detachment on case 1. As a whole trend, the pressure inside the bubble is decreased continuously. From 0.1 ms to 0.6 ms, the bubble growth is in the inertial control stage. Bubble expands rapidly leading to the dramatic pressure drop inside bubble. From 0.6 ms to 1.2 ms, the bubble growth is in the thermal diffusion control stage. The bubble growth rate is relatively low and stable. The pressure inside the bubble fluctuates from 1500 Pa to 2000 Pa. From 1.2 ms to 2.6 ms, the bubble is in detaching. Because of the intensive condensation of a departing bubble caused by subcooled liquid, the bubble diameter dramatically decreases and the pressure inside bubble drops rapidly also.

4.1.3. *Velocity Field of Growing Bubble.* Figure 9 shows the velocity vector field at $t = 1.0$ ms, $t = 2.8$ ms on case 1. According to the analysis of the pressure filed around a bubble, eddies are formed by the pressure discrepancy around the bubble. As shown at $t = 1.0$ ms, eddies can be observed on both sides of the growing bubble. The eddy accelerates contraction of the vapor-liquid interface at bottom of bubble, which leads to bubble shape changing from ellipsoid to approximate sphere. As the eddies transfer subcooled liquid to the heating wall on both sides of bubble, the micro-convection in the vicinity of bubble is enhanced, which would increase heat transfer significantly. At $t = 2.8$ ms, the difference of the fluid velocity on both sides of the departing bubble is quite evident, which accelerates bubble departing from the heating wall.

Figure 10 shows the velocity curve along the center-line of bubble in different bubble growth times. It shows

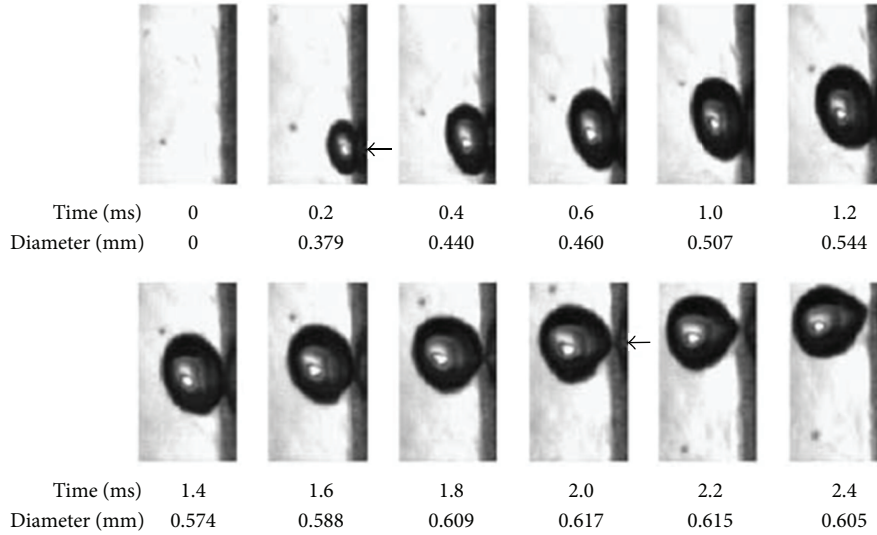


FIGURE 6: The typical photos of bubble growth in subcooled flow boiling in Rong Situ [11] experiment.

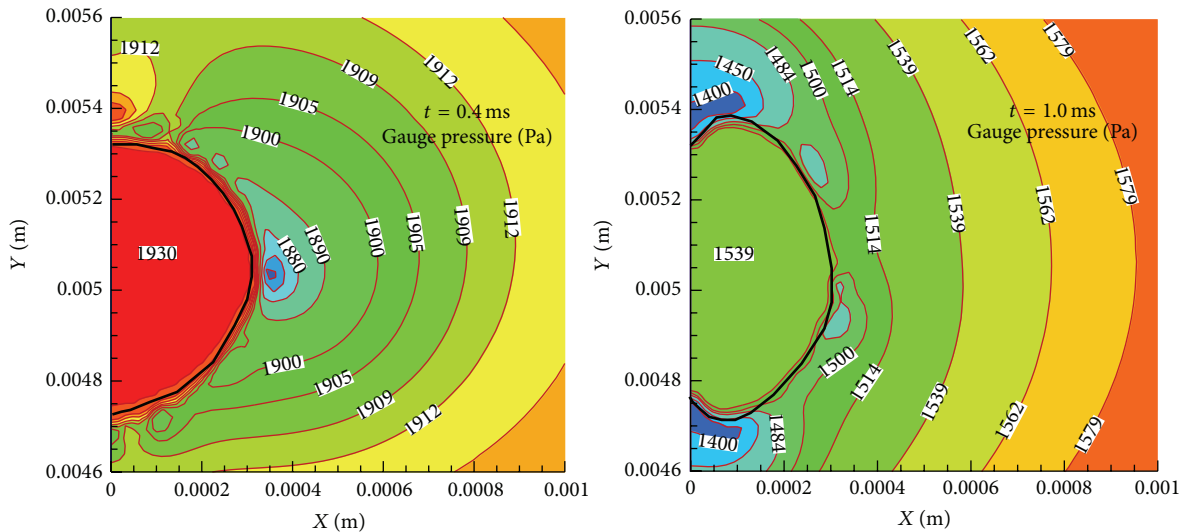


FIGURE 7: The pressure field distribution of bubble growth at $t = 0.4$ ms and $t = 1.0$ ms on case 1.

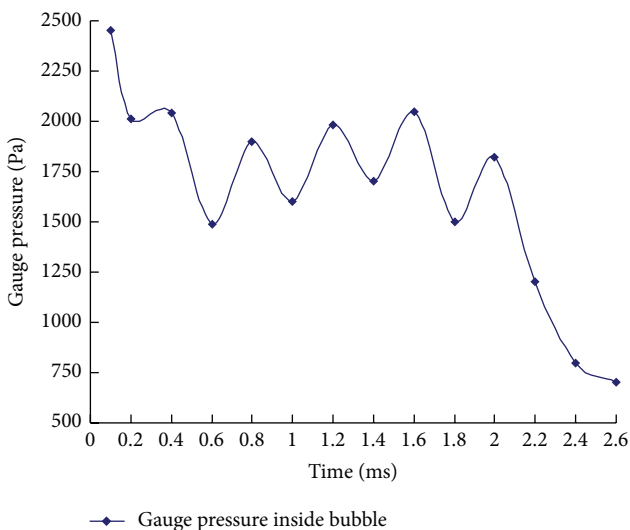


FIGURE 8: The gauge pressure inside bubble varying with bubble growth and detachment time on case 1.

that, along the centerline of bubble, from inside bubble to the mainstream liquid region around bubble, the velocity increases gradually and at the vapor-liquid interface the velocity fluctuation appears. From 0.2 ms to 1.2 ms, with increase of bubble growth time, the velocity inside the bubble gradually reduced.

4.2. *The Dynamic Contact Angle Bubble Shape Evolution.* Figure 11 is the evolution of bubble shape from bubble growth to movement on different conditions of case 2 to case 5. It can be seen that the bulk velocity, liquid subcooling, wall superheat, and vapor-liquid contact angle will lead to different bubble dynamic. Figure 12 shows the dynamic contact angle and the incline angle changes with different working conditions. It can be seen that the dynamic contact angles β_u and β_d are keeping constant in bubble growth; meanwhile β_u is equal to β_d ; $\beta_u = \beta_d$. For example in case 2, the dynamic contact angles β_u and β_d are 45° in bubble growth; in case 3, the dynamic contact angles β_u and β_d are

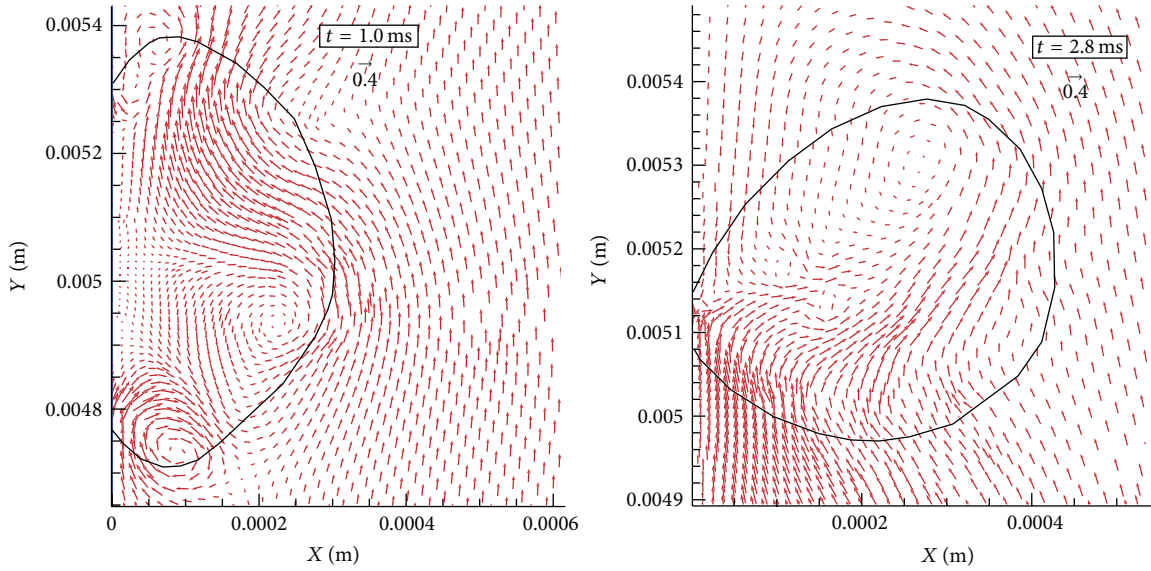


FIGURE 9: The velocity field distribution on case 1.

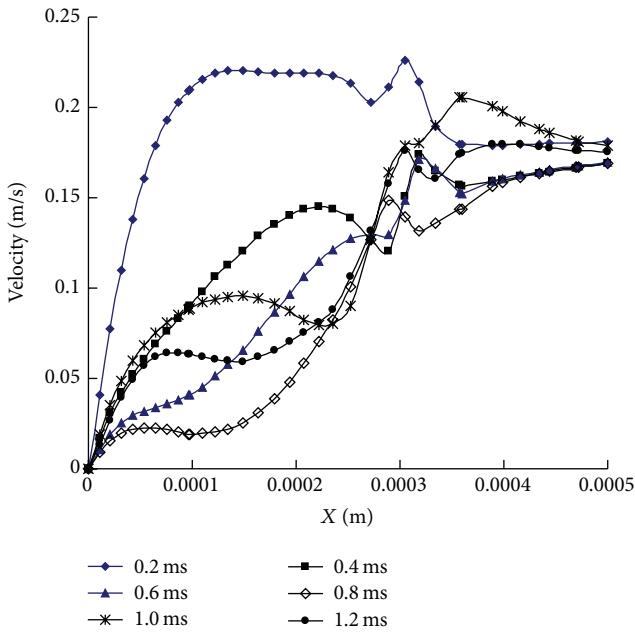


FIGURE 10: The velocity curve along the centerline of bubble in bubble growth on case 1.

60° in bubble growth; in case 4 the dynamic contact angles β_u and β_d are 60° in bubble growth; in case 5 the dynamic contact angles β_u and β_d are 63° in bubble growth. According to contact angle hysteresis theory, the dynamic contact angle values varied between the receding contact angle β_{re} and the advancing angle β_{ad} on the heating wall in the heterogeneous boiling system. The numerical results of dynamic contact angle in bubble growth results agreed with this theory. Based on the numerical results, the incline angles are all 0° in case 2

to case 5. It means that the incline angle is little influenced by working conditions on bubble growth process.

When bubble was on the stage of detachment or sliding on the wall, bubble shape and the dynamic contact angle were strongly influenced by working condition. As shown in Figure 12(a), bubble changes slowly from the ellipsoidal shape on the heating wall to spherical shape; the contact area at bottom of bubble on the heating wall slowly decreases during bubble departure progress. As shown in Figure 12(a), during the bubble departure from heating wall on case 2, the dynamic contact angles β_u and β_d gradually reduced compared with bubble growth. In a certain moment β_u and β_d keep constant and β_u was equal to β_d . The characteristic of dynamic contact angles β_u and β_d on bubble departure and sliding progress still followed the theory of contact angle hysteresis phenomenon; the numerical results of dynamic contact angle on the progress of bubble growth or detachment or sliding from the heating wall varied between receding contact angle β_{re} and the advance contact angle β_{ad} which was defined as boundary conditions. The incline angle kept constant during bubble detertment: $\theta = 0^\circ$. As shown in Figure 12(b), the characteristic of dynamic contact angle and incline angle in case 3 was the same as in case 2. As shown in Figure 12(c), in case 4 bubble shape was ellipsoidal shape at the beginning of bubble sliding on the heating wall and persistently changed during bubble sliding on the heating wall. The dynamic contact angles β_u and β_d changed rapidly at the beginning of bubble sliding and kept constant when bubble sliding velocity became stable, while β_u was not equal to β_d . The incline angle θ varied from 0° to -40° at the beginning of bubble sliding on the wall. As shown in Figure 12(d) the characteristic of dynamic contact angle and incline angle in case 5 was the same as in case 4 while the incline angle θ varied from 0° to -40° at the beginning of bubble sliding on the wall.

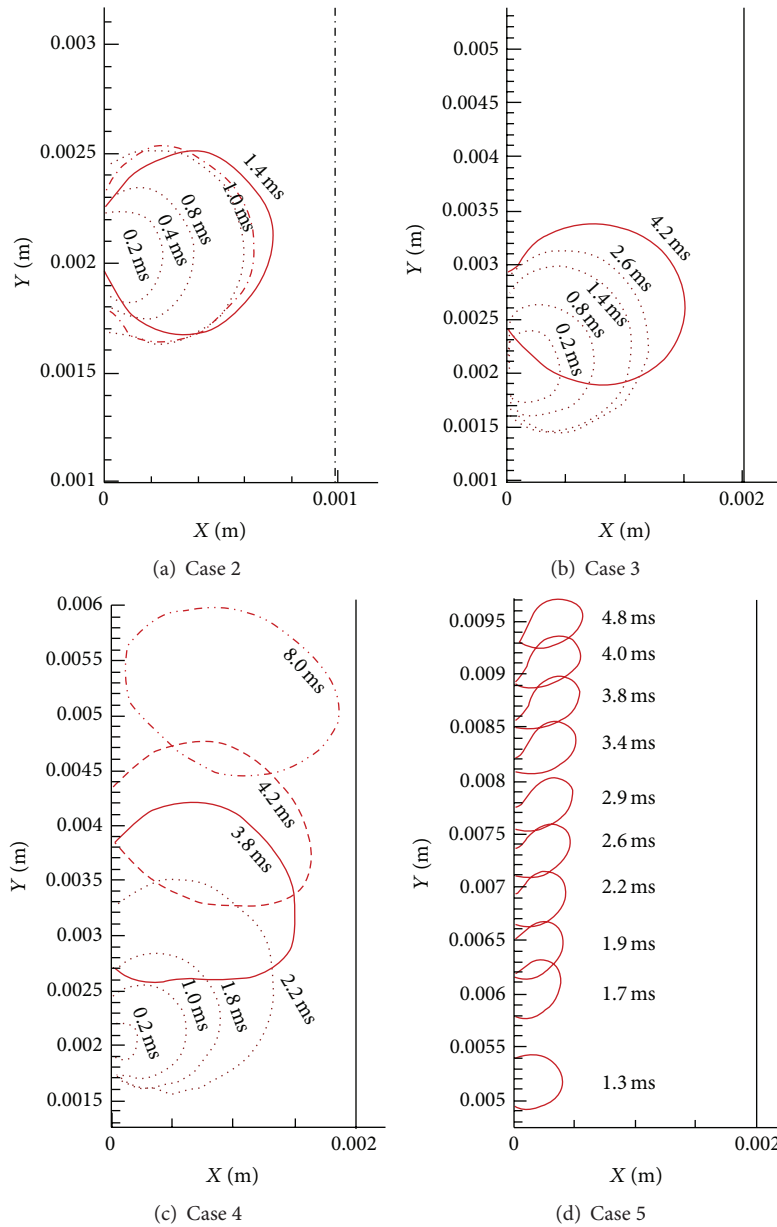


FIGURE 11: The evolution of bubble shape from bubble growth to movement on different conditions.

5. Conclusions

In this paper, a numerical investigation on the bubble growth in subcooled flow boiling has been proposed, and several conclusions are obtained as follows.

- (1) A mechanism model for bubble growth in subcooled flow boiling has been proposed in this study, and the bubble growth curve is obtained based on CFD simulation; the simulation results agree with the experimental results with uncertainty within $\pm 25\%$.
- (2) The evolution of bubble shape is complicated. At the initial time of bubble growth, a large amount of

heat and mass transfers through the micro-layer into the bubble and the bubble grows fast and expands rapidly as a hemisphere. As the condensation gradually enhances at the top of bubble, bubble growth rate becomes much slower than that of before. The forces acting on a growing bubble have significant effect on the bubble evolution.

- (3) There are eddies around the growing bubble. The eddy accelerates contraction of the vapor-liquid interface at the bottom of the bubble, which leads to bubble shape changing and bubble detachment, and this will enhance the of micro-convection heat transfer in the vicinity of a bubble.

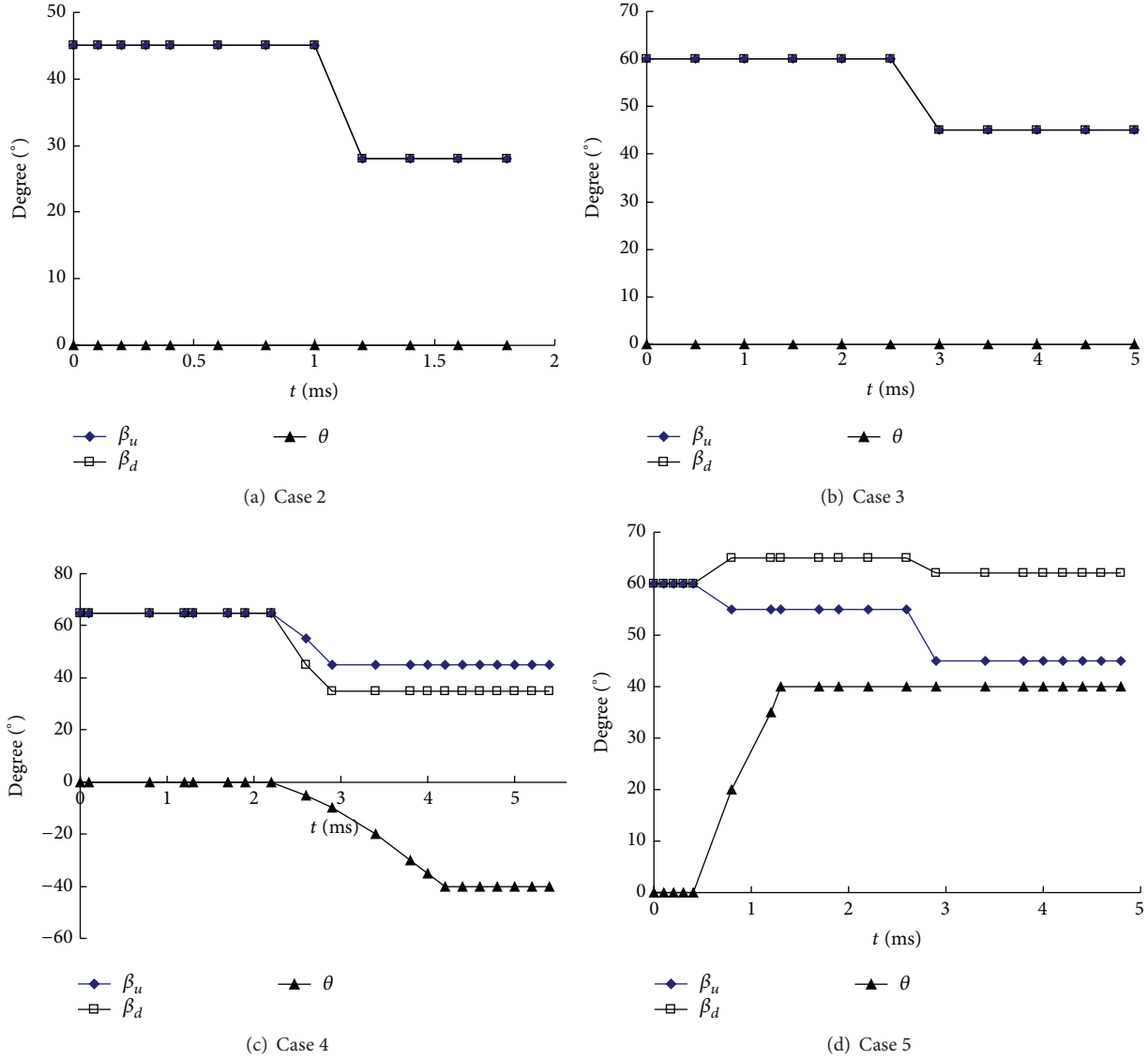


FIGURE 12: The contact angle degree curve in different condition.

Nomenclature

- E : Energy
- F : Surface tension force
- h_{fg} : Latent heat, kJ/kg
- m : The net mass flow rate per unit area, kg/(m²·s)
- M : Mass per mole, kg/mol
- p : Pressure, Pa
- q : Heat flux, kW/m²
- r : Bubble radius, m
- R : Universal gas constant, J/(mol·K)
- S : The mass source term
- t : Time, s
- T : Temperature, K
- u : Velocity, m/s
- x, y : Coordinate axis
- δ : Micro-layer thickness under the bubble bottom, m
- σ : Surface tension coefficient, N/m
- σ_e, σ_c : Coefficient of the vapor-liquid interface

- α : Volume fraction
- ρ : Density, kg/m³
- λ : Thermal conductivity of liquid, W/(m·K)
- ΔT : The temperature difference, K.

Subscripts

- l : Liquid
- v : Vapor
- w : Wall
- s : Saturated
- e : Evaporation
- c : Condensation
- i : i th fluid component.

Competing Interests

The authors declare that there is no conflict of interests regarding the publication of this paper.

Acknowledgments

The authors are grateful for the support of the National Science Foundation of China (no. 51106142 and no. 51206199) and the project funded by China Postdoctoral Science Foundation (no. 2014M562337).

References

- [1] R. Mei, W. Chen, and J. F. Klausner, "Vapor bubble growth in heterogeneous boiling-I. Formulation," *International Journal of Heat and Mass Transfer*, vol. 38, no. 5, pp. 909–919, 1995.
- [2] S. W. J. Welch, "Direct simulation of vapor bubble growth," *International Journal of Heat and Mass Transfer*, vol. 41, no. 12, pp. 1655–1666, 1998.
- [3] S. Heo, S. Koshizuka, and Y. Oka, "Numerical analysis of boiling on high heat-flux and high subcooling condition using MPS-MAFL," *International Journal of Heat and Mass Transfer*, vol. 45, no. 13, pp. 2633–2642, 2002.
- [4] W. Z. Li, Y. Y. Yan, and J. M. Smith, "A numerical study of the interfacial transport characteristics outside spheroidal bubbles and solids," *International Journal of Multiphase Flow*, vol. 29, no. 3, pp. 435–460, 2003.
- [5] J. Liao, R. Mei, and J. F. Klausner, "The influence of the bulk liquid thermal boundary layer on saturated nucleate boiling," *International Journal of Heat and Fluid Flow*, vol. 25, no. 2, pp. 196–208, 2004.
- [6] P. Genske and K. Stephan, "Numerical simulation of heat transfer during growth of single vapor bubbles in nucleate boiling," *International Journal of Thermal Sciences*, vol. 45, no. 3, pp. 299–309, 2006.
- [7] A. Mukherjee and S. G. Kandlikar, "Numerical study of single bubbles with dynamic contact angle during nucleate pool boiling," *International Journal of Heat and Mass Transfer*, vol. 50, no. 1-2, pp. 127–138, 2007.
- [8] G. Hazi and A. Markus, "On the bubble departure diameter and release frequency based on numerical simulation results," *International Journal of Heat and Mass Transfer*, vol. 52, no. 5-6, pp. 1472–1480, 2009.
- [9] Fluent Inc, *Fluent 6.2 User's Guide*, Fluent Inc, Lebanon, Pa, USA, 2005.
- [10] C. W. Hirt and B. D. Nichols, "Volume of fluid (VOF) method for the dynamics of free boundaries," *Journal of Computational Physics*, vol. 39, no. 1, pp. 201–225, 1981.
- [11] H. Chi-Yeh and P. Griffith, "The mechanism of heat transfer in nucleate pool boiling-Part I. Bubble initiation, growth and departure," *International Journal of Heat and Mass Transfer*, vol. 8, no. 6, pp. 887–904, 1965.
- [12] D. L. Youngs, "Numerical simulation of turbulent mixing by Rayleigh-Taylor instability," *Physica D: Nonlinear Phenomena*, vol. 12, no. 1–3, pp. 32–44, 1984.
- [13] J. U. Brackbill, D. B. Kothe, and C. Zemach, "A continuum method for modeling surface tension," *Journal of Computational Physics*, vol. 100, no. 2, pp. 335–354, 1992.
- [14] L. S. Tong and Y. S. Tang, *Boiling Heat Transfer And Two-Phase Flow*, CRC Press, Boca Raton, Fla, USA, 2nd edition, 2001.
- [15] A. J. Addlesee and K. Cornwell, "Liquid film thickness above a bubble rising under an inclined plate," *Chemical Engineering Research and Design*, vol. 75, no. 7, pp. 663–667, 1997.
- [16] R. R. Olander and R. G. Watts, "An analytical expression of microlayer thickness in nucleate boiling," *Journal of Heat Transfer*, vol. 91, no. 1, pp. 178–180, 1969.
- [17] R. Marek and J. Straub, "Analysis of the evaporation coefficient and the condensation coefficient of water," *International Journal of Heat and Mass Transfer*, vol. 44, no. 1, pp. 39–53, 2001.
- [18] I. W. Eames, N. J. Marr, and H. Sabir, "The evaporation coefficient of water: a review," *International Journal of Heat and Mass Transfer*, vol. 40, no. 12, pp. 2963–2973, 1997.
- [19] R. Marek, *Einfluß thermokapillarer Konvektion und inerte Gase beim Blasensieden in unterkühlter Flüssigkeit [Ph.D. thesis]*, Technical University of Munich, 1996.
- [20] R. Marek and J. Straub, "Origin of thermocapillary convection in subcooled nucleate pool boiling," *International Journal of Heat and Mass Transfer*, vol. 44, no. 3, pp. 619–632, 2001.
- [21] Y. Chen, R. Mertz, and R. Kulenovic, "Numerical simulation of bubble formation on orifice plates with a moving contact line," *International Journal of Multiphase Flow*, vol. 35, no. 1, pp. 66–77, 2009.
- [22] G. Hazi and A. Markus, "On the bubble departure diameter and release frequency based on numerical simulation results," *International Journal of Heat and Mass Transfer*, vol. 52, no. 5-6, pp. 1472–1480, 2009.
- [23] R. Zhuan and W. Wang, "Simulation on nucleate boiling in micro-channel," *International Journal of Heat and Mass Transfer*, vol. 53, no. 1–3, pp. 502–512, 2010.
- [24] S. Marity, *Effect of velocity and gravity on bubble dynamics [M.S. thesis]*, University of California, Los Angeles, Calif, USA, 2000.
- [25] D.-Q. Chen, L.-M. Pan, D.-W. Yuan, and X.-J. Wang, "Dual model of bubble growth in vertical rectangular narrow channel," *International Communications in Heat and Mass Transfer*, vol. 37, no. 8, pp. 1004–1007, 2010.
- [26] R. Situ, T. Hibiki, M. Ishii, and M. Mori, "Bubble lift-off size in forced convective subcooled boiling flow," *International Journal of Heat and Mass Transfer*, vol. 48, no. 25-26, pp. 5536–5548, 2005.

Research Article

Wave Characteristics of Falling Film on Inclination Plate at Moderate Reynolds Number

Chuan Lu, Sheng-Yao Jiang, and Ri-Qiang Duan

Institute of Nuclear and New Energy Technology, Collaborative Innovation Center of Advanced Nuclear Energy Technology, Key Laboratory of Advanced Reactor Engineering and Safety of Ministry of Education, Tsinghua University, Beijing, China

Correspondence should be addressed to Ri-Qiang Duan; duanrq@mail.tsinghua.edu.cn

Received 20 June 2016; Accepted 10 August 2016

Academic Editor: Xiangdong Li

Copyright © 2016 Chuan Lu et al. This is an open access article distributed under the Creative Commons Attribution License, which permits unrestricted use, distribution, and reproduction in any medium, provided the original work is properly cited.

Falling water film on an inclined plane is studied by shadowgraphy. The ranges of inclination angle and the film Reynolds number are, respectively, up to 21° and 60. Water is used as working fluid. The scenario of wave regime evolution is identified as three distinctive regimes, namely, initial quiescent smooth film flow, two-dimensional regular solitary wave pattern riding on film flow, and three-dimensional irregular wave pattern. Three characteristic parameters of two-dimensional solitary wave pattern, namely, inception length, primary pulse spacing, and propagation velocity, are examined, which are significant in engineering applications for estimation of heat and mass transfer on film flow. The present experimental data are well in agreement with the Koizumi correlations, the deviation from which is limited to 20% and 15%, respectively, for primary pulse spacing and propagation velocity. Through the scrutiny of the present experimental observation, it is concluded that wave evolution on film flow at the moderate Reynolds number is controlled by gravity and drag and the Rayleigh-Taylor instability that occurred on the steep front of primary pulse triggers the disintegration of continuous two-dimensional regular solitary wave pattern into three-dimensional irregular wave pattern.

1. Introduction

Falling thin film flow has special applications in nuclear engineering due to its unique advantages, namely, high thermal efficiency, zero pumping power consumption, and low flow rate. For AP1000 nuclear plants, film flow falling down from a storage tank is the core safety measure of the Passive Cooling Containment System (PCCS). In sea-water thermal desalination powered by nuclear energy, pure water is produced via evaporation of film flow attached to tube-bundle surface in multiple-effect evaporators due to its high thermal efficiency. To meet the demand of engineering applications, Yu and Cheng [1] investigated statistically falling film on large-scale plates to develop an empirical correlation among flowrate, film thickness, and wave characteristics. However, as well known, the behaviors of heat and mass transfer of film flow are more dependent on film topography and surface wave dynamics than substrate layer flow. Thus, in this paper, flow pattern and wave characteristics on film

flow are experimentally scrutinized to explore the surface topological change for evaluation of heat and mass transfer on film flow from the physical viewpoint.

The wave evolution of falling film is mainly controlled by the Reynolds number, which Portalski [2] used to classify wave mode of falling film flow. Our experiments cover the film Reynolds number in the moderate range from 10 to 60, the corresponding wave modes under which span pseudolaminar up to pseudoturbulent regime [2]. Film flow at the moderate Reynolds number has many applications in industry [3]. At the moderate Reynolds number, it has been established that waves, appearing on a smooth surface, develop quickly into two-dimensional ordered solitary wave pattern featured by the primary pulse preceding with a series of small capillary ripples, and then the pattern is readily susceptible to precipitate breakup into three-dimensional chaotic wave pattern [4]. To discern wave structure and characteristics, small inclination angle (up to 20°) is used in this experiments to slow down its spacial variation.

In this present experiments, initial disturbance of falling film flows is imposed in the natural excitation way. Two-dimensional solitary wave riding on film flow is investigated in this study, including its dynamics, interaction with each other, and transition to three-dimensional complex disordered wave pattern. Two-dimensional solitary wave on film flow was first recorded in the P. L. Kapitza and S. P. Kapitza's pioneering work [5]. It exhibits rich information of coherent structure and nonlinear hydrodynamics of wavy film flow and intrigues a lot of theoretical and numerical investigations on its behaviors and characteristics. Most of previous experimental researches of two-dimensional solitary wave on film flow [4, 6] were limited on forcing excitation by introducing single-frequency disturbance at film entrance, which is however different from practical scenarios of film flow due to the linear filtering nature and the effect of inescapable surrounding noise. Because instabilities of film flow are noise-sustained [7], falling film flow dynamics are considerably affected by the inlet conditions. Natural disturbances (white noise) introduced into inlet evolve on film flow with different scenarios from artificially introduced excitation in inlet. The study of our present experiment is carried out under natural excitation, which is meaningful for engineering applications, as mentioned above in the PCCS of the AP1000 nuclear reactor and the multiple-effect evaporator in seawater desalination. Meanwhile, the previous experimental works on two-dimensional solitary wave on film flow mostly focused on variation of local film thickness [8, 9]. In this study, two key parameters of two-dimensional solitary wave on film flow, namely, primary pulse spacing (wave length) and its propagation velocity, are paid attention to, which are significant to estimate heat and mass transfer for film flow.

On the triggering mechanism of transition of two-dimensional ordered solitary pattern into disordered three-dimensional pattern, it has not yet got well elucidated and no agreement has been achieved. Liu et al. [3] roughly redefined the transition as a secondary instability, which is assumed to initiate coalescence, and splitting processes of two-dimensional solitary wave fronts and furthermore evolve into complicated three-dimensional disordered patterns. Park and Nosoko [10] conjectured that the capillary instability (the Plateau-Rayleigh instability) occurring at the valley right next to primary solitary pulse triggers the transition due to its large curvature, which results in necking breakup of solitary pulse. So there is need to clarify the mechanism in this study. Furthermore, all the previous works on the transition issue are addressed to forcing excitation in inlet. In this paper, the transition to three-dimensional instability on film flow under natural disturbance in inlet is examined, which is motivated by the noise-sustained behavior of film flow instability.

In the present experiments, distilled water is used as working fluid. The shadowgraphic technique is employed to visualize wave structure and flow pattern and measure variables over liquid film. The method is low-cost and high-sensitive to film thickness. It can obtain readily the detail contour of film topography.

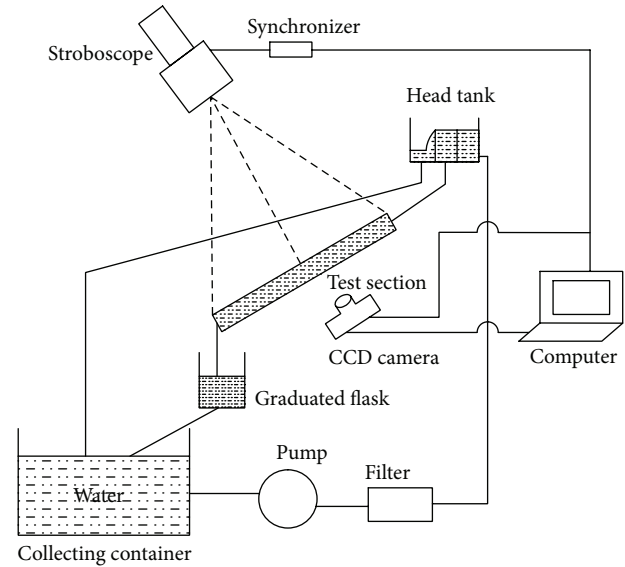


FIGURE 1: Schematic diagram of experimental system.

2. Experiment Apparatus and Procedure

The experimental system used in the present study is shown schematically in Figure 1. The experiments are conducted at room temperature and atmospheric pressure. Distilled water is pumped into a head tank through a filter to remove contamination. The head tank is constructed into three compartments to regulate the film Reynolds number and meanwhile isolate the disturbances out of pump vibration. The right compartment is linked to water feed from the filter. Water brims into the middle compartment and then further spills into the left draining compartment. In such a way, water level in the middle compartment is kept smooth and steady. The left one is used to drain the brimming water from the middle compartment. Water flows through a silicone tube, one end of which is linked to the bottom drain hole of the middle compartment, into a specially designed apparatus to produce water film flow. The film Reynolds number is regulated by adjusting the partition height of the middle compartment to change pressure head of film flow. The volumetric flow rate of film flow is measured with a flask and a stopwatch at the exit of the apparatus.

The apparatus for producing water film is schematically shown in Figure 2. The film plate is made of flat Plexiglas with 0.80 m in length and 0.30 m in width, which is fixed on a rectangular Plexiglas framework. To spread uniformly film flow on the film plate and minimize the effect of wetting difference along the film plate, a small portion is partitioned by a bar at the top of the film plate, in which multiple intertwined layers of $150\ \mu$ sintered wire mesh with fabric thread are tightly stuffed. Water flows into the test section through the gap between the bar and the film plate. The apparatus is mounted on a supporting structure, which stands on a rubber pad to reduce any building vibration. The inclination angle can be continuously adjusted in the range of $0\text{--}45^\circ$ from horizontal plane.

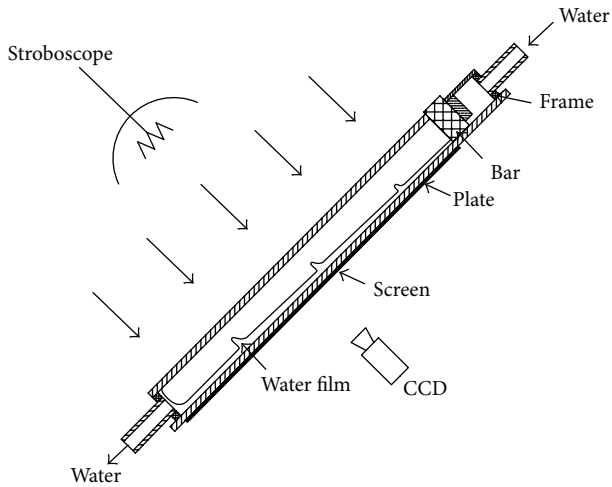


FIGURE 2: Apparatus of generating a falling water film.

Water film is illuminated with a stroboscope and its shadow on a screen is captured with a Charge Coupled Device (CCD) digital video camera synchronized with the stroboscope. The stroboscope flashes at the rate of 30–14000 FPM with 0.1 FPM in both resolution and accuracy. Wave velocity is calculated from the displacement of the same wave peak and the time interval. The procedure is performed for a number of frames that are selected randomly. The average of measured values derived in this manner is defined as wave velocity for a certain experimental condition. The uncertainty of a measured wave velocity is less than approximately 0.0008 m/s. Wave separation is measured in a frame, in which at least two wave peaks are contained. As in wave velocity measurement, a number of frames are selected randomly. The average of measured values is taken as wave separation. The uncertainty of wave separation is less than 0.001 m.

3. Results and Discussion

Film flow is investigated at the moderate Reynolds number from 10 to 60. The experimental observations in the present study show wave on film flow in natural excitation is spatially evolved in three modes based on film topographical variation and wave pattern. In the entrance region of film flow, a train of equally spaced streaks appears on the surface of falling film, as shown in Figure 3, which is defined as the first mode. The lasting length of the first mode depends on the Reynolds number and the inclined angle of film plate. Then, wave evolution on film flow enters the second mode, featured with two-dimensional ordered solitary wave pattern, seen in Figure 4. The structure of solitary wave is characteristic of a large-amplitude primary pulse with steep front preceded with a series of capillary ripples, the amplitudes of which are decreased one by one downstream. Further downstream, two-dimensional ordered solitary wave pattern is precipitately transformed into three-dimensional irregular wave pattern, for example, discrete crater-like and caterpillar-like structures, as illustrated in Figure 5, which is defined as the third mode.

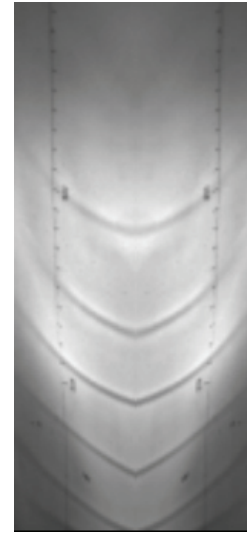


FIGURE 3: Regular streak-like wave pattern, $\beta = 8^\circ$ and $Re = 22$.



FIGURE 4: Two-dimensional regular wave packet, $\beta = 13^\circ$ and $Re = 32$.

3.1. Spatial Development of Two-Dimensional Solitary. Wave evolution in two-dimensional solitary wave pattern is one significant stage of film flow in an inclined plate, which has great effect on heat transfer distribution. Two-dimensional solitary wave pattern starts appearing at a certain distance from the inlet and forms a train of solitary primary pulses downstream, which signals the inception of two-dimensional solitary wave pattern on film flow. They are almost equally spaced between each other with nearly flat film portion. Wave evolution in the two-dimensional solitary wave pattern is a typical convective instability, which is just modulated in the stream-wise direction and held stationary in the transverse direction. In our experiments, primary pulses are bulged out at the central plane due to sidewall effect, the shape of which is just reflection of the transverse distribution of the surface

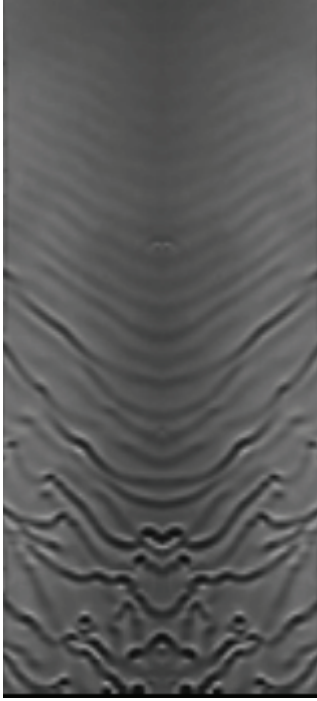


FIGURE 5: Two-dimensional regular wave packet, $\beta = 13^\circ$ and $Re = 56$.

velocity. In this study, the following statistical qualities of two-dimensional solitary wave pattern are extracted, namely, inception length of two-dimensional solitary wave pattern, primary pulse spacing, and its propagation velocity, from the wave profile along the central stream-wise plane to diminish the sidewall effect.

Inception Length of Two-Dimensional Solitary. The inception length of two-dimensional solitary wave pattern is defined as the distance from the inlet where the first visible two-dimensional solitary wave pattern can be recognized based on naked eye. In our investigation, the inception lengths of two-dimensional solitary wave pattern fall into the range of 20 cm to 40 cm, as shown in Table 1, the values of which are consistent with those of Jones and Whitaker [11] observations (30–60 cm) at the comparable inclination angle and the Reynolds number. The experimental results show that the inception length of solitary wave pattern is decreased with inclination angle and little dependent on the Reynolds number. So it is inferred that wave evolution at the moderate Reynolds number is still dominated by drag and gravity and the contribution of inertial force is not yet up to such a degree to change the global evolution trend of two-dimensional solitary wave.

Primary Pulse Spacing. Two-dimensional solitary wave pattern is regularly spaced in sequence with coherent structure. In our investigation, the average primary pulse spacing is in the range of 2–5 cm, as shown in Figure 6, the value of which falls into the range of gravity-driven wave and is in agreement with Jones and Whitaker [11] and Koizumi et al. [12] experiments. The experimental data reveal that the

TABLE 1: Inception length of two-dimensional solitary.

Inclination angle	Reynolds number	Inception length of two-dimensional solitary
8°	21.2~28.3	~37
13°	18.2~29.2	~26
21°	56.7~57.1	~18.5

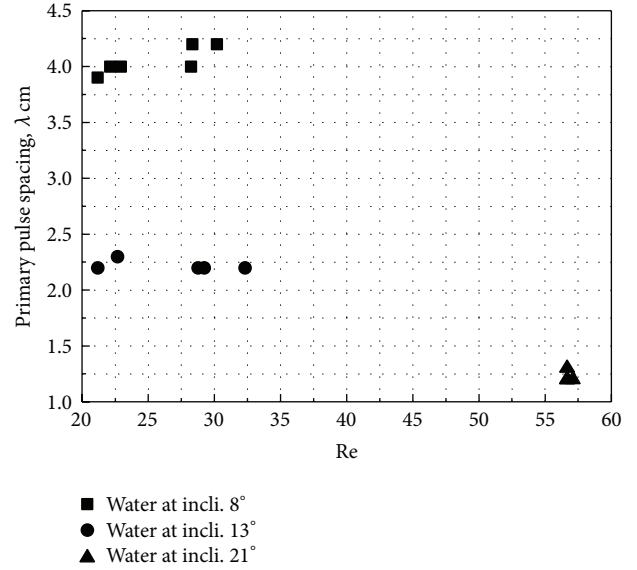


FIGURE 6: Separation spacing between adjacent solitary pulses.

dependence of the primary pulse spacing on inclination angle and the Reynolds number is the same as for inception length of solitary.

Solitary Wave Propagation Velocity. Due to riding on falling film flow, the propagation velocity of solitary wave results from both wave propagation itself and convection of surface film flow [13]. In this study, the propagation velocity is normalized with the Nusselt mean film velocity, as it is reduced to the ratio of C_w/V_{Nu} , in part for manifestation of actual wave propagation and in part for comparison with the data of other researchers. The Nusselt mean film velocity is expressed as follows:

$$V_{Nu} = \frac{\rho g h_{Nu}^2}{3\mu}, \quad (1)$$

where h_{Nu} is Nusselt's flat film thickness for laminar falling film [2].

Figure 7 shows the ratio with the film Reynolds number at different inclination angle, the trend of which is consistent with previous experimental observations. The ratio exhibits a larger spread in the range of 2 to 3 at $Re \leq 30$, the value of which is in agreement with the prediction of Carey [14]. And the effect of inclination angle on wave propagation velocity appears almost independent of it at small Reynolds number. As the Reynolds number increases to ~ 60 , the ratio asymptotically approaches a certain constant, the mechanism of which may be that the dependence of the ratio on the

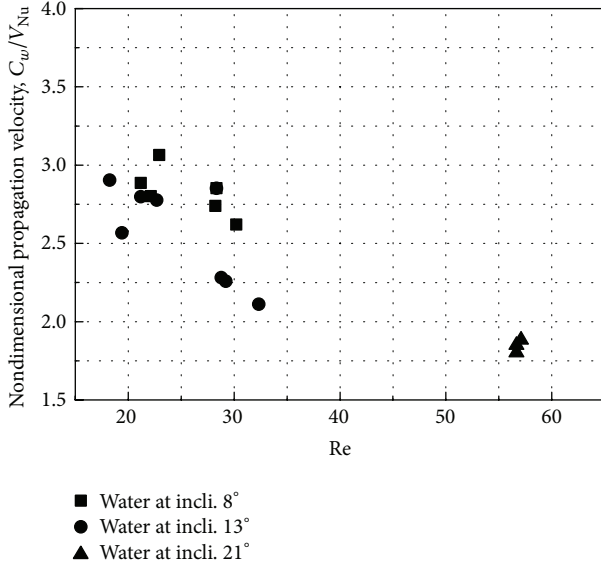


FIGURE 7: Solitary wave propagation velocity.

Reynolds number is the same as that for the Nusselt surface film velocity, causing the ratio to become independent on the Reynolds number.

Dimensionless Correlations of Primary Pulse Spacing and Propagation Velocity. Data reduction of primary pulse spacing and propagation velocity is performed based on the Buckingham π -theorem [15] in this study. For solitary wave on free film flow under natural excitation, primary pulse spacing λ and propagation velocity C_w can be approximately treated independently of each other. Based on physical analyses, both of them are dependent on the five physical qualities, that is, Γ , ρ , ν , σ , $g \sin \beta$. Thus, there are six variables in three dimensions, that is, m, s, and kg, for both primary pulse separation and propagation velocity in film flow. These variables can be combined into three dimensionless groups to correlate primary pulse spacing and propagation velocity. Four dimensionless groups are derived in the same way as Koizumi et al. [12]:

(a) Nondimensional propagation velocity

$$N_{uw} = \frac{C_w}{(\nu g \sin \beta)^{1/3}}. \quad (2)$$

(b) Nondimensional primary pulse spacing

$$N_\lambda = \frac{\lambda}{h_{Nu}}. \quad (3)$$

(c) Film Reynolds number

$$Re = \frac{\Gamma}{\mu}. \quad (4)$$

(d) Froude number

$$Fr = \frac{C_w}{\sqrt{g \sin \beta h_{Nu}}}. \quad (5)$$

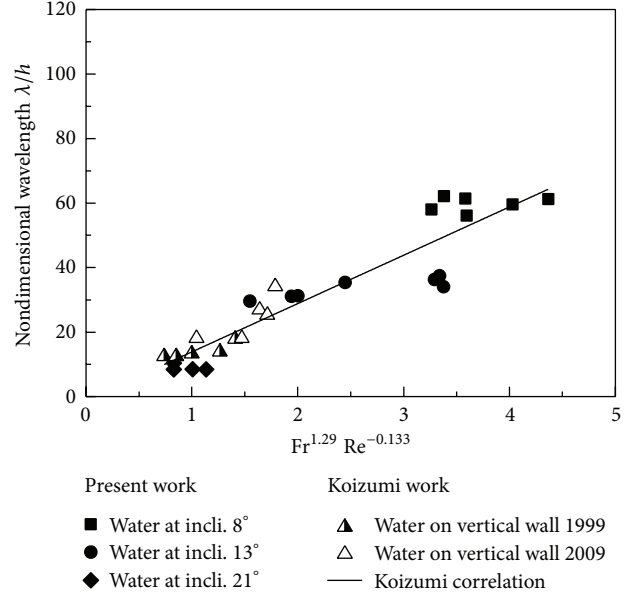


FIGURE 8: Comparison of nondimensional primary pulse spacing between experiments and Koizumi correlation.

The present data of primary pulse spacing and propagation velocity are reformulated with the film Reynolds number and the Froude number using the Koizumi nondimensional correlations, as shown in (6) and (7). Comparing with other relevant correlations, Koizumi correlation is a closure relation under the inlet boundary conditions, which requires only the film flow rate given at the inlet, the geometrical parameters of film plate, and the physical properties of working fluid.

$$N_\lambda = 12.39 Fr^{1.29} Re^{-0.133}, \quad (6)$$

$$N_{uw} = 1.13 Fr^{0.582} Re^{0.429}. \quad (7)$$

Figure 8 shows the present data of nondimensional primary pulse spacing. The Koizumi data with water are also presented in Figure 8 for comparison. The continuous line is correlation (6). The deviation of all the present data from the correlation falls into the $\pm 20\%$ offset strip.

The present data of nondimensional propagation velocity are shown in Figure 9. The data of Koizumi et al. [12] for water film on the outer wall of a vertical pipe and the data of Takahama and Kato [16] for the water film on the inner wall of a vertical pipe are also plotted in the figure. The continuous line is correlation (7). The deviation of all the present data from the correlation falls into the $\pm 15\%$ offset strip.

3.2. Transition to Three-Dimensional Disordered Wave Pattern. The experimental observations show that two-dimensional regular solitary wave pattern is in an unstable state and eventually destructed into three-dimensional disordered wave pattern. It is supposed that there are certainly some fundamental instabilities which trigger the process at some critical conditions. On the destruction mechanism, previous researchers had striven to elucidate it based on some hypotheses. Park and Nosoko [10], Demekhin et al. [17], and Kofman

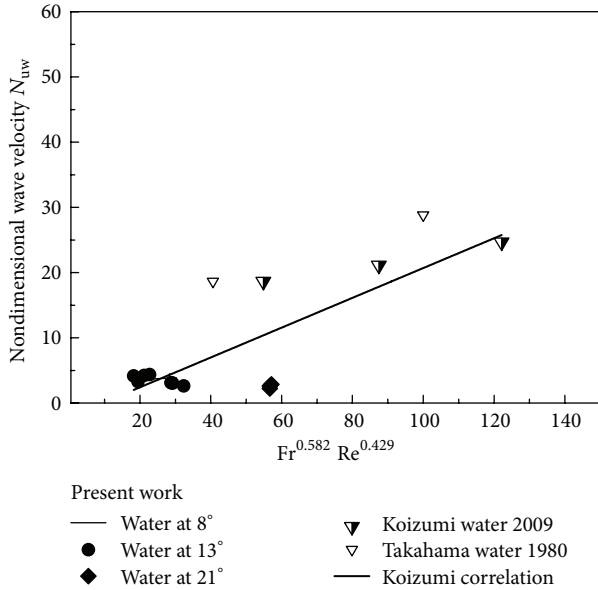


FIGURE 9: Comparison of nondimensional propagation velocity between experiments and Koizumi correlation.

et al. [18] attributed it to the Plateau-Rayleigh instability, which is assumed to occur on the steep ridge between primary solitary pulse and its immediate preceding capillary ripple due to high concentration of surface tension force. And Kofman et al. [18] thought that the Plateau-Rayleigh instability only has effect on the transition in a capillary region with short-wave mode whereas for long-wave mode the transition is triggered by the Rayleigh-Taylor instability. Liu et al. [3] and Scheid et al. [19] ascribed it to 3D synchronous transverse modulations along the trough of primary solitary pulse, but the mechanism behind it was not yet illuminated.

Our experiments show that the transition to three-dimensional disordered wave pattern from regular two-dimensional solitary wave pattern is a fleeting process, which is initiated on the wave-front of primary solitary pulse, and then it precipitately breaks up into discontinuous irregular patterns with different size and shape; that is, some are like caterpillar and some are like crater, as shown in Figure 10. The most compelling feature of three-dimensional wave pattern is that the broken wave segments are with different size and shape and are being evolved out of phase for successive wave fronts, which are originally in phase and separated from one another regularly. Such the patterns and sizes formed are obviously different from that under the Plateau-Rayleigh instability, the typical pattern under which is equally distributed bead-like with similar size and shape.

Through the scrutiny of the transition process from the present experiments, it is found out that bubble-spike structure is firstly formed on the steep front of solitary pulse before the breakup of two-dimensional solitary structure. The bubble-spike structure on interface between fluids is typical of the Rayleigh-Taylor instability under gravity field. Triggering the Rayleigh-Taylor instability on the solitary pulse front, we think, is supposed to be due to steepness of



FIGURE 10: Three-dimensional irregular wave pattern.

solitary pulse front, which is almost vertical to the film plate. Under the stream-wise component of gravity, the Rayleigh-Taylor instability is induced on the front surface of solitary pulse. In addition, the present experiments show that the time scale of the transition process is also consistent with characteristic time scale of the Rayleigh-Taylor instability.

4. Conclusions

Wave characteristics of falling film on inclination plate at the moderate Reynolds number are experimentally investigated using shadowgraphy, the spatial evolution scenario of which covers from initial disturbance up to transition to three-dimensional irregular wave pattern. Working fluid is water at the room temperature and atmospheric pressure. The following conclusions are achieved:

- (1) At the moderate Reynolds number, the evolution of surface disturbance in thin film flow under the natural excitation manifests itself clearly by three distinctive evolution regimes along stream-wise direction, namely, initial quiescent smooth film flow, two-dimensional regular solitary wave pattern riding on film flow, and three-dimensional irregular wave pattern formed on the surface of film flow.
- (2) The inception length of sensible two-dimensional solitary wave pattern is more dependent on the inclination angle than the Reynolds number at the moderate Reynolds number. It is inferred that wave evolution on film flow at the moderate Reynolds number is controlled by gravity and drag.
- (3) On the development of two-dimensional regular solitary wave pattern, the two parameters, namely, primary pulse spacing and propagation velocity, which are significant to engineering applications for estimating heat and mass transfer on film flow, are investigated. The present experimental results of the

two parameters are compared with the Koizumi correlations, which is the closed correlations under natural excitation. The deviation of the present experimental data from the correlations is limited to 20% and 15%, respectively, for primary pulse spacing and propagation velocity.

- (4) On the transition from two-dimensional regular solitary wave pattern to three-dimensional irregular wave pattern, it is revealed that the disintegration of continuous two-dimensional regular solitary wave pattern is triggered by the Rayleigh-Taylor instability that occurred on the steep front of primary pulse. This is in disagreement with other researchers, for example, the Plateau-Rayleigh instability and 3D synchronous moderation.

Nomenclature

C_w :	Propagation velocity
Fr:	Froude number
h_{Nu} :	Nusselt flat film thickness
g :	Gravitational acceleration
N_{uw} :	Nondimensional propagation velocity
N_λ :	Nondimensional primary pulse spacing
Re:	Film Reynolds number
V_{Nu} :	Nusselt mean film velocity
β :	Angle between film plate and horizontal direction
λ :	Primary pulse spacing
μ :	Dynamic viscosity
ρ :	Density.

Competing Interests

The authors declared no potential conflict of interests with respect to the research, authorship, and/or publication of this article.

Acknowledgments

The authors disclosed receipt of the following financial support for the research, authorship, and/or publication of this article: This paper is based on some of the results of projects under Grant nos. 51321002 and 11472155, which were supported by the Science Fund for Creative Research Groups of the National Natural Science Foundation of China.

References

- [1] Y. Q. Yu and X. Cheng, "Experimental study of water film flow on large vertical and inclined flat plate," *Progress in Nuclear Energy*, vol. 77, pp. 176–186, 2014.
- [2] S. Portalski, "Studies of falling liquid film flow film thickness on a smooth vertical plate," *Chemical Engineering Science*, vol. 18, no. 12, pp. 787–804, 1963.
- [3] J. Liu, J. B. Schneider, and J. P. Gollub, "Three-dimensional instabilities of film flows," *Physics of Fluids*, vol. 7, no. 1, pp. 55–67, 1995.
- [4] T. Nosoko, P. N. Yoshimura, T. Nagata, and K. Oyakawa, "Characteristics of two-dimensional waves on a falling liquid film," *Chemical Engineering Science*, vol. 51, no. 5, pp. 725–732, 1996.
- [5] P. L. Kapitza and S. P. Kapitza, "Wave flow of thin fluid layers of liquid," in *Collected Papers of P. L. Kapitza*, D. T. Haar, Ed., pp. 662–709, Pergamon Press, Oxford, UK, 1964.
- [6] J. Liu and J. P. Gollub, "Solitary wave dynamics of film flows," *Physics of Fluids*, vol. 6, no. 5, pp. 1702–1712, 1994.
- [7] J. Liu, J. D. Paul, and J. P. Gollub, "Measurements of the primary instabilities of film flows," *Journal of Fluid Mechanics*, vol. 250, pp. 69–101, 1993.
- [8] K. J. Chu and A. E. Dukler, "Statistical characteristics of thin, wavy films: part II. Studies of the substrate and its wave structure," *AIChE Journal*, vol. 20, no. 4, pp. 695–706, 1974.
- [9] R. P. Salazar and E. Marschall, "Time-average local thickness measurement in falling liquid film flow," *International Journal of Multiphase Flow*, vol. 4, no. 4, pp. 405–412, 1978.
- [10] C. D. Park and T. Nosoko, "Three-dimensional wave dynamics on a falling film and associated mass transfer," *AIChE Journal*, vol. 49, no. 11, pp. 2715–2727, 2003.
- [11] L. O. Jones and S. Whitaker, "An experimental study of falling liquid films," *AIChE Journal*, vol. 12, no. 3, pp. 525–529, 1966.
- [12] Y. Koizumi, R. Enari, and H. Ohtake, "Correlations of wave characteristics for a liquid film falling down along a vertical wall," *Journal of Heat Transfer*, vol. 131, no. 8, pp. 1–9, 2009.
- [13] M. J. Lighthill, *Waves in Fluids*, Cambridge University Press, Cambridge, UK, 2nd edition, 2001.
- [14] V. P. Carey, *Liquid-Vapor Phase-Change Phenomena*, Hemisphere Publishing Corporation, Bristol, UK, 1992.
- [15] J. H. Lienhard IV and J. H. Lienhard V, *A Heat Transfer Textbook*, Phlogiston Press, Cambridge, UK, 3rd edition, 2008.
- [16] H. Takahama and S. Kato, "Longitudinal flow characteristics of vertically falling liquid films without concurrent gas flow," *International Journal of Multiphase Flow*, vol. 6, no. 3, pp. 203–215, 1980.
- [17] E. A. Demekhin, E. N. Kalaidin, S. Kalliadasis, and S. Y. Vlaskin, "Three-dimensional localized coherent structures of surface turbulence. I. Scenarios of two-dimensional-three-dimensional transition," *Physics of Fluids*, vol. 19, no. 11, Article ID 114103, 2007.
- [18] N. Kofman, S. Mergui, and C. Ruyer-Quil, "Three-dimensional instabilities of quasi-solitary waves in a falling liquid film," *Journal of Fluid Mechanics*, vol. 757, pp. 854–887, 2014.
- [19] B. Scheid, C. Ruyer-Quil, and P. Manneville, "Wave patterns in film flows: modelling and three-dimensional waves," *Journal of Fluid Mechanics*, vol. 562, pp. 183–222, 2006.

Research Article

Parametric Investigation and Thermo-economic Optimization of a Combined Cycle for Recovering the Waste Heat from Nuclear Closed Brayton Cycle

Lihuang Luo, Hong Gao, Chao Liu, and Xiaoxiao Xu

Key Laboratory of Low-Grade Energy Utilization Technologies and Systems of Ministry of Education,
College of Power Engineering, Chongqing University, Chongqing 400030, China

Correspondence should be addressed to Hong Gao; gaohong@cqu.edu.cn

Received 19 April 2016; Accepted 22 June 2016

Academic Editor: Xiangdong Li

Copyright © 2016 Lihuang Luo et al. This is an open access article distributed under the Creative Commons Attribution License, which permits unrestricted use, distribution, and reproduction in any medium, provided the original work is properly cited.

A combined cycle that combines AWM cycle with a nuclear closed Brayton cycle is proposed to recover the waste heat rejected from the precooler of a nuclear closed Brayton cycle in this paper. The detailed thermodynamic and economic analyses are carried out for the combined cycle. The effects of several important parameters, such as the absorber pressure, the turbine inlet pressure, the turbine inlet temperature, the ammonia mass fraction, and the ambient temperature, are investigated. The combined cycle performance is also optimized based on a multiobjective function. Compared with the closed Brayton cycle, the optimized power output and overall efficiency of the combined cycle are higher by 2.41% and 2.43%, respectively. The optimized LEC of the combined cycle is 0.73% lower than that of the closed Brayton cycle.

1. Introduction

With the development of the world economy, the total energy consumption increases steadily. The consumption of the energy, especially fossil energy resources, causes and accelerates the occurrence of many environmental problems. Nuclear energy is an efficient energy source that plays an important role in current energy demand. Because of its inherent safety, the high temperature gas-cooled reactor (HTGR) has attracted many attentions of the researchers. To ensure the high efficiency of nuclear power plant, reasonable thermodynamic cycle should be used. Despite the higher efficiency of HTGR, a large amount of waste heat is discharged from the precooler of the nuclear closed Brayton cycle. Thus, research topics focus on recovery and utilization of this low grade thermal energy.

At present, the waste heat of the closed Brayton cycle can be recovered by several ways, as follows: desalination, Organic Rankine Cycle (ORC), Kalina cycle, and ammonia-water combined power/cooling cycle. Soroureddin et al. [1] proposed the utilization of this waste heat for power production by using ORC. Dardour et al. [2] proposed

and analyzed the utilization of waste heat from GT-MHR and PBMR reactors for nuclear desalination of sea water. Since Kalina [3] introduced the Kalina cycle with the ammonia-water mixture as the working fluid, at least 30 new cycles based on the Kalina cycle have been presented. Goswami [4] also put forward a combined power/cooling cogeneration cycle with ammonia-water mixture as working fluid. For a turbine inlet temperature and pressure of 410 K and 30 bar, the first law efficiency is 23.54%; such value is much better than ORC or Kalina cycle [5]. Padilla et al. [6] and Lu and Goswami [7] modified the combined power/cooling cogeneration cycle and studied the effect of key parameters on cycle performance. Pouraghaie et al. [8] revealed that the efficiency of the combined power/cooling cogeneration cycle is much higher than that of a conventional steam Rankine cycle. Demirkaya et al. [9] also found that the combined power/cooling cogeneration cycle has a promising prospect for effective utilization of waste heat because of the reasonably good matching between the temperature profiles of helium and ammonia-water mixture in the boiler.

Meanwhile, many investigations focused on the design and optimization of waste heat recovery system. Some studies

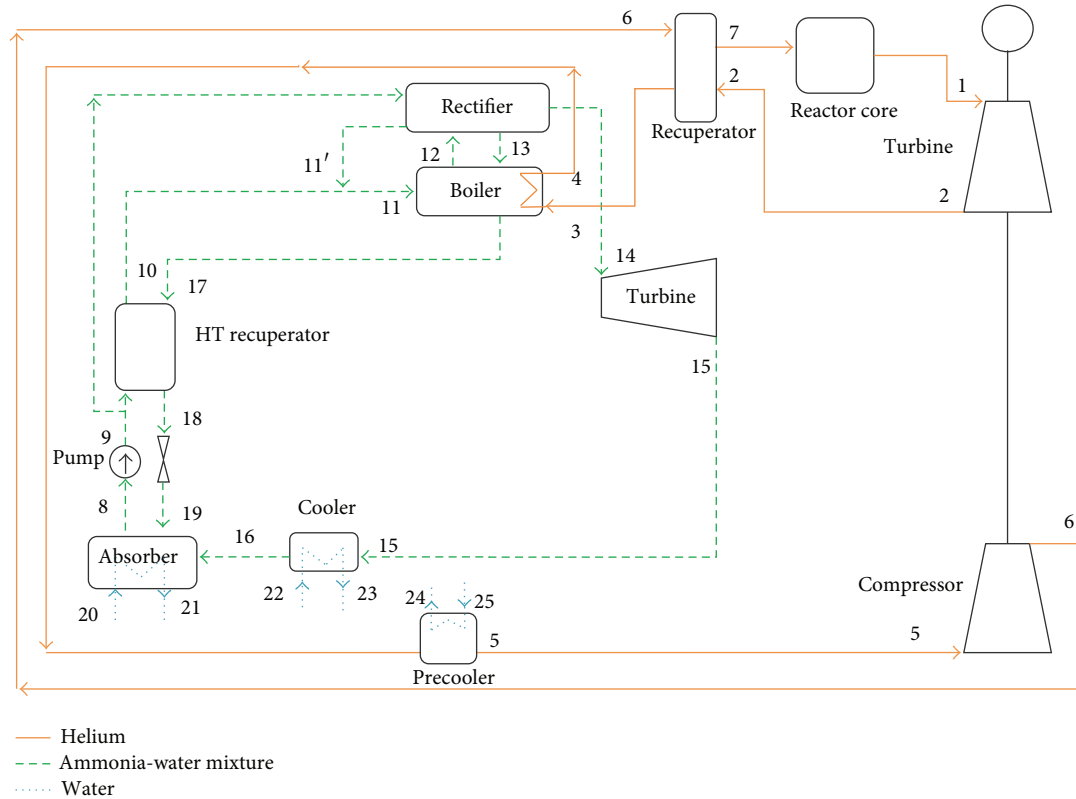


FIGURE 1: Schematic diagram of the combined cycle.

optimized the system according to the net power output, cooling output, first law efficiency, and second law efficiency [8–10]. Shengjun et al. [11] used five indicators: thermal efficiency, exergy efficiency, recovery efficiency, and so on, to optimize the subcritical ORC system and transcritical cycle. Guo et al. [12] used the net power output per unit mass flow rate of hot source, ratio of total heat transfer area to net power output, and electricity production cost to screen working fluids. Coskun et al. [13] proposed four cycles to utilize the geothermal energy and selected one cycle to optimize for the turbine inlet pressure that would generate maximum power output, energy, and exergy efficiencies. Zare et al. [14] carried out an exergoeconomic analysis for a combined GT-MHR/Kalina cycle and compared the performance with the Gas Turbine-Modular Helium Reactor (GT-MHR) plant. Bahlouli et al. [15] perform a parametric study and multiobjective optimization for a bottoming cycle of a trigeneration system with HCCI engine as prime mover. Feng et al. [16] conducted a sensitivity analysis for low temperature ORCs (Organic Rankine Cycles), as well as the thermo-economic comparison between the basic ORC and regenerative ORC.

According to the studies proposed in the public literatures, few investigations focused on the system economic analysis of the combined cycle, especially the evaluation of the levelized energy cost (LEC). In this paper, a combined cycle, in which a power/cooling cogeneration cycle is integrated into the nuclear closed Brayton cycle, is proposed to recover and utilize the waste heat rejected from the precooler of the closed Brayton cycle. Based on a detailed parametric

analysis, a multiobjective function $F(X)$, integrating the overall efficiency and the system cost, is used to optimize the thermodynamic and the economic performances of the combined cycle. So the main contributions of the paper are the combined system analysis and multiobjective optimization according to several important parameters.

2. System Description and Assumptions

A schematic diagram of the proposed combined cycle is shown in Figure 1. The nuclear core of HTGR is the heat source of the closed Brayton cycle. High pressure helium, as the coolant and the working fluid [2], is heated in the reactor and then enters the gas turbine (state 1) for expansion to convert thermal energy into shaft power, thereby driving the compressors and the electric generator on a single shaft. Since the temperature of the exhaust gas from the turbine (state 2) is still high, a recuperator is equipped to utilize the energy of the exhaust gas from the gas turbine, in which the cold helium from the compressor (state 6) is preheated by the turbine exhaust gas. Then, the exhaust gas flows through the precooler to be cooled (state 5). The cooled helium has low pressure and low temperature after the precooler (state 5) and is compressed by the compressor (state 6). Helium with high pressure and low temperature enters the other side of the recuperator mentioned above to be preheated (state 7) before finally flowing into the reactor core to be heated again to repeat the thermodynamic cycle.

TABLE 1: Energy relations for the equipment of closed Brayton cycle and AWM cycle.

Cycle	Equipment	Energy equations
Closed Brayton cycle	Reactor core	$Q_{\text{core}} = m_1 (h_1 - h_7)$
	Turbine	$W_T = m_1 (h_1 - h_{2s}) \eta_{s,T}$
	Recuperator	$(h_2 - h_3) = (h_7 - h_6)$
	Precooler	$Q_{\text{precooler}} = m_1 (h_4 - h_5)$
	Compressor	$W_C = \frac{m_1 (h_{6s} - h_5)}{\eta_{s,C}}$
AWM cycle	Boiler	$m_1 (h_3 - h_4) = m_{12} h_{12} + m_{17} h_{17} - m_{11} h_{11} - m_{13} h_{13}$
	Rectifier	$m_{14} h_{14} + m_{13} h_{13} + m_{11'} (h_{11'} - h_9) = m_{12} h_{12}$
	HT recuperator	$m_{17} (h_{17} - h_{18}) = m_{10} (h_{10} - h_9)$
	Absorber	$Q_{\text{absorber}} = m_{19} h_{19} + m_{16} h_{16} - m_8 h_8$
	Turbine	$W_T = m_{14} (h_{14} - h_{15s}) \eta_{s,T}$
	Cooler	$Q_{\text{cool}} = m_{15} (h_{16} - h_{15})$
	Pump	$W_P = \frac{m_8 (h_{9s} - h_8)}{\eta_{s,P}}$
	Throttle valve	$h_{19} = h_{18}$

$\eta_{s,T}$, $\eta_{s,C}$, and $\eta_{s,P}$ represent the isentropic efficiency of the turbine, the compressor, and the pump, respectively.

The helium flowing out from the gas turbine flows into the hot side of the recuperator where the helium is cooled to about 400 K. To reduce the compressor power consumption, the helium should be cooled to about 300 K before flowing into the compressor. Thus, the ammonia-water power/cooling cycle (AWM), proposed by Goswami [17] in 2000, is coupled into this closed Brayton cycle to utilize the waste heat rejected from the precooler. In this situation, the helium flowing out from the hot side of the recuperator enters a boiler before entering the precooler. The heat released by the helium passing through the boiler is the heat resource of the AWM cycle. Then, a part of the HTGR waste heat is recovered for the AWM cycle to produce power. The AWM cycle uses high concentration of ammonia as the working fluid, which can be expanded to a very low temperature in the turbine. The very low temperature ammonia-water mixture provides refrigeration. The net effects are the production of both power and refrigeration.

An ammonia-water mixture (state 8) is pumped to a high pressure (state 9) and heated to boil off ammonia (state 12). The vapor is enriched in ammonia by condensing a part of the vapor in a rectifier (state 14). The condensate is richer in water and returned to the boiler (state 13). The ammonia vapor, which is almost pure ammonia, can be expanded in a turbine to exit at a very low temperature (state 15). After expansion in the turbine to generate power, low temperature ammonia first provides cooling capacity in the cooler (state 16) and is absorbed by low concentration solution from the boiler in an absorber, to form the basic ammonia-water liquid solution to complete the cycle (state 8) [17].

The following assumptions are used in this work:

- (1) The system operates in a steady state condition.
- (2) Changes in kinetic and potential energies are neglected.
- (3) The pressure loss due to the frictional effects is neglected.

(4) The turbine and the pump in the combined cycle have isentropic efficiencies [15].

(5) The ammonia-water solution leaving the absorber (state 8) is a saturated liquid at low pressure.

3. System Modeling

3.1. Thermodynamic Modeling. A MATLAB code has been developed to carry out the numerical simulations for this combined cycle. The thermodynamic properties of the states in the closed Brayton cycle are evaluated by REFPROP 9.0. The thermodynamic properties of the states of the bottom cycle (AWM cycle) are evaluated by the method proposed by Xu and Goswami [18]. For thermodynamic analysis, the principles of mass and energy conservations as well as the second law of thermodynamics are applied to each component.

To simplify the calculation, just one operation condition of the closed Brayton cycle is selected according to the literature [19], and the parameters are listed in Table 5.

The energy relations for the equipment of combined cycle are listed in Table 1.

For the combined cycle, the net power output can be defined as follows:

$$\begin{aligned} W_{\text{net,Combinedcycle}} &= W_{\text{net,B}} + W_{\text{net,AWM}} \\ &= (W_T - W_C)_B + (W_T - W_P)_{\text{AWM}}. \end{aligned} \quad (1)$$

The overall efficiency of the combined cycle is defined as follows:

$$\eta_{\text{overall,Combinedcycle}} = \frac{W_{\text{net,B}} + W_{\text{net,AWM}} + W_{\text{cool}}}{Q_{\text{core}}}. \quad (2)$$

TABLE 2: Comparison between the properties of the present work and those from the published literature [17].

State	T (K)	p (bar)	h (kJ/kg)		s (kJ/kg K)		x	
			a^*	b^*	a^*	b^*	a^*	b^*
8	280.0	2.0	-214.1	-214.4	-0.1060	-0.1061	0.53	0.53
9	280.0	30.0	-211.4	-211.6	-0.1083	-0.1084	0.53	0.53
11	378.1	30.0	246.3	246.7	1.2907	1.2924	0.53	0.53
12	400.0	30.0	1547.2	1549.8	4.6102	4.6223	0.9432	0.9451
13	360.0	30.0	205.8	206.1	1.1185	1.1201	0.6763	0.6760
14	360.0	30.0	1373.2	1374.1	4.1520	4.1546	0.9921	0.9938
15	257.0	2.0	1148.9	1177.6	4.5558	4.6702	0.9921	0.9938
16	280.0	2.0	1278.7	1284.6	5.0461	5.0734	0.9921	0.9938
17	400.0	30.0	348.2	347.9	1.5544	1.5563	0.4147	0.4269
18	300.0	30.0	-119.0	-120.7	0.2125	0.2105	0.4147	0.4269

a^* : the thermodynamic properties presented in literature [17].

b^* : the thermodynamic properties calculated in this work.

The cooling capacity is converted to equivalent power and can be expressed as

$$W_{\text{cool}} = \frac{Q_{\text{cool}}}{\text{cop}}, \quad (3)$$

where cop is the coefficient of performance and set as 4 [20].

3.1.1. Verification of Ammonia-Water Thermodynamic Properties. To verify the developed thermodynamic models for AWM cycle, the available data in the literature are used. The comparisons between the simulation results and those reported in the published literature are presented in Table 2. For AWM cycle, the data in Table 2 indicate a very good agreement between simulation results of this paper and those in published literature [17], and the maximum deviation is only 2.5%.

3.2. Economic Modeling. To evaluate the thermoeconomic performance of the combined cycle, leveled energy cost (LEC) is analyzed in this paper. Because the aim of this paper is to evaluate the effect of AWM cycle on the thermodynamic and economic performances of the combined cycle, the HTGR plant (closed Brayton cycle) specific cost is assumed to be 1073\$/kW [21]. A cost of 8\$/MWh is assumed for nuclear fuel [22].

Then, the capital investment of AWM cycle is calculated. According to the literature [23], the heat exchangers, pump, and turbine contribute largely to the total cost. We assume that all of the heat exchangers in AWM system are shell-and-tube heat exchanger [24, 25].

The heat exchanger area can be expressed as follows:

$$A = \frac{Q}{(U\Delta T_m)}, \quad (4)$$

$$\Delta T_m = \frac{(\Delta T_{\text{max}} - \Delta T_{\text{min}})}{\ln(\Delta T_{\text{max}}/\Delta T_{\text{min}})},$$

where Q represents the heat exchanger heat load; U stands for the overall heat transfer coefficient; and ΔT_m is the logarithmic mean temperature difference. The heat transfer

TABLE 3: Heat transfer coefficients for heat exchangers [33].

Component	Heat transfer coefficient (W/m ² K)
Absorber	800
Separator	900
Cooler	1000
Recuperator	800

coefficients of some heat exchangers in AWM cycle are shown in Table 3.

The overall heat transfer coefficient of the boiler can be calculated as follows [26]:

$$\frac{1}{U} = \frac{1}{h_{\text{He}}} + \frac{\delta}{k} + \frac{1}{h_{\text{aw}}} + R, \quad (5)$$

where h_{He} is the heat transfer coefficient of the helium; h_{aw} is the ammonia-water heat transfer coefficient and is 2000 W/(m²K) [27] according to the characteristic of the cycle; δ is the thickness of the heat exchanger tube; k is the heat conductivity of the tube; R is the heat resistance of the tube.

The heat transfer coefficient of the helium in the shell is calculated by the following equations:

$$\text{Nu}_{\text{He}} = 0.023 \text{Re}_{\text{He}}^{0.8} \text{Pr}_{\text{He}}^{0.65} \left(\frac{T_w}{T_b} \right)^{-c},$$

$$c = 0.57 - \left(\frac{1.59}{l/d} \right), \quad (6)$$

$$h_{\text{He}} = \frac{\text{Nu} \lambda}{d}.$$

For the above equations, Re and Pr are Reynolds number and Prandtl number, respectively. T_w and T_b are the temperatures of the shell and tube, respectively. λ is the thermal conductivity coefficient. d is the diameter or equivalent hydraulic diameter of the heat exchanger. l is the length of the tube.

TABLE 4: Coefficients required for the cost evaluation for each component [26].

Components	K_1	K_2	K_3	C_1	C_2	C_3	B_1	B_2	F_m	F_{bm}
Turbine	3.15140	0.5890	0	0	0	0	0	0	0	3.50
Pump	3.5790	0.3210	0.0290	0.1680	0.3480	0.4840	1.80	1.51	1.80	Equation (9)
Heat exchanger	3.2138	0.2688	0.07961	-0.064991	0.05025	0.01474	1.80	1.50	1.25	Equation (9)

TABLE 5: Specifications of the combined cycle [19].

Parameters	Value
m_1 (kg/s)	358.8
$\eta_{s,P}$	0.85
T_1 (K)	1179.1
T_5 (K)	301
p_1 (bar)	67.6
$\eta_{s,T}$	0.85
$\eta_{s,C}$	0.85
T_3 (K)	398.8
T_7 (K)	855.4
p_2 (bar)	31.0

The capital costs of the AWM system consist of the heat exchanger, pump, and turbine costs and are expressed as follows [26, 28]:

$$\lg C_b = K_1 + K_2 \lg Z + K_3 (\lg Z)^2, \quad (7)$$

where C_b is the estimated component cost based on US dollars in the year of 1996. Z is a parameter related to cycle components. For the heat exchanger, Z refers to the area of heat exchanger, A . For the pump, Z means the power consumption in pump, W_p . For the turbine, Z represents the power output, W_{out} . The coefficients of K_1 , K_2 , and K_3 are listed in Table 4.

The capital cost C , which is corrected according to the component materials and the pressure, is determined by (8), as follows:

$$C = C_b F_{bm}, \quad (8)$$

where the coefficient F_{bm} is 3.5 for the turbine and the coefficients F_{bm} for other components are calculated by (9) [29] as follows:

$$F_{bm} = B_1 + B_2 F_m F_p, \quad (9)$$

where B_1 and B_2 are the coefficients of different types of the components and F_m is the correction coefficient for the component materials. The values of B_1 , B_2 , and F_m are presented in Table 4.

F_p represents the pressure correction coefficient and is calculated by

$$\lg F_p = C_1 + C_2 \times \lg p + C_3 \times (\lg p)^2. \quad (10)$$

The coefficients of C_1 , C_2 , and C_3 are also shown in Table 4.

Thus, the cost of the AWM system in the year 1996 $C_{AWM,1996}$ can be evaluated as follows:

$$C_{AWM,1996} = C_H + C_E + C_P. \quad (11)$$

According to the time value of money, the cost of closed Brayton system in the year of 2006 and the AWM system in the year of 1996 are converted into the capital costs in the year of 2015, respectively, and the total cost of the combined cycle (C_{2015}) is their sum, as follows:

$$C_{2015} = C_{B,2006} \frac{CEPCI_{2015}}{CEPCI_{2006}} + C_{AWM,1996} \frac{CEPCI_{2015}}{CEPCI_{1996}}, \quad (12)$$

where $CEPCI_{1996}$, $CEPCI_{2006}$, and $CEPCI_{2015}$ are the chemical plant cost indexes in the years 1996, 2006, and 2015, and the values are 382, 510, and 592, respectively [30].

The capital recovery factor (CRF) is defined as follows:

$$CRF = \frac{i(1+i)^{T_s}}{(1+i)^{T_s} - 1}. \quad (13)$$

In this equation, i is the discount rate and is 5% with inflation rate zero [21]. The economic life of the combined system (T_s) is 40 years.

For each year, the operation hour of the system is calculated as follows:

$$OP_s = 365 \times 24 \times L_f. \quad (14)$$

In the combined system, the levelized energy cost (LEC) can be calculated by (14). One has

$$LEC = \frac{CRF \times C_{2015} + COM_s}{(W_{net} + W_{cool}) \times OP_s}, \quad (15)$$

where COM_s is the system operation and maintenance cost and is 1.5% of C_{2015} . The load factor L_f is taken as 0.75 [31].

3.3. Optimization Model. A simple thermodynamic optimization or economical optimization might draw different results, because it is difficult to ensure a global cost-effective cycle design. Thus, the optimizations on both the thermodynamics and economics are simultaneously needed in the assessment of the combined cycle. Regarding this, overall efficiency $\eta_{overall, Combinedcycle}$ and levelized energy cost (LEC) are selected to build a multiobjective function as the performance indicator in this paper. The multiobjective optimization model is constructed as follows.

The first objective function $F_1(X)$ is expressed by the following:

$$\min F_1(X) = \frac{1}{\eta_{overall, Combinedcycle}}. \quad (16)$$

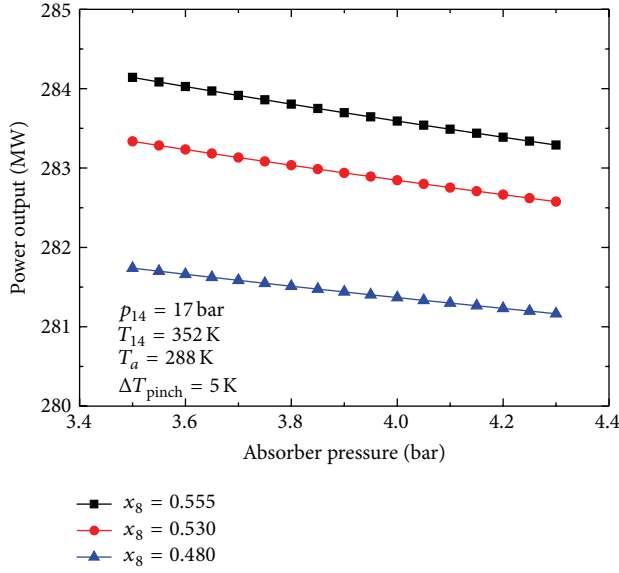


FIGURE 2: Variation of power output of combined cycle with absorber pressure.

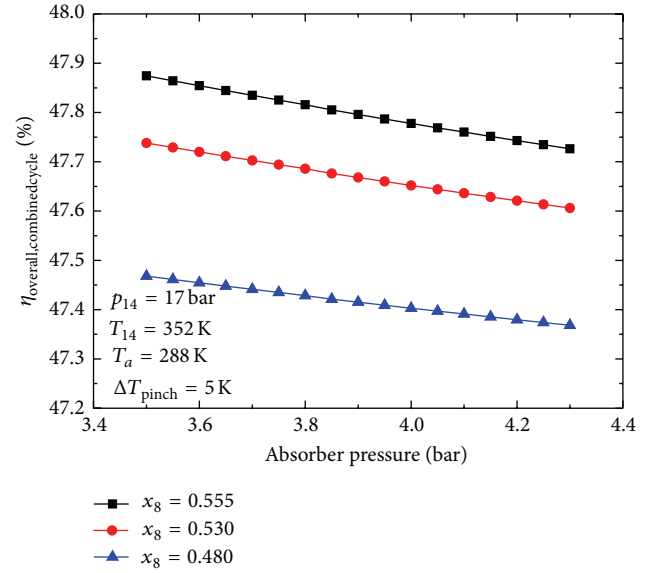


FIGURE 3: Variation of overall efficiency of combined cycle with absorber pressure.

The second objective function $F_2(X)$ is expressed by the following:

$$\min F_2(X) = \text{LEC}. \quad (17)$$

The first objective function $F_1(X)$ represents system thermodynamic property, and the second objective function $F_2(X)$ is the thermo-economic property.

In this paper, the method of linear weighted evaluation function is adopted to solve the objective function optimization model [28], which contains more than two performance indicators. The multiobjective function $F(X)$ is given by the following:

$$F(X) = \alpha F_1(X) + \beta F_2(X), \quad (18)$$

where α and β are the weight coefficients of objective function and a method proposed by Карлевиц is applied to solve these two weight coefficients [32]:

$$\alpha = \frac{(F_2^1 - F_2^2)}{[(F_1^2 - F_1^1) + (F_2^1 - F_2^2)]}, \quad (19)$$

$$\beta = \frac{(F_1^2 - F_1^1)}{[(F_1^2 - F_1^1) + (F_2^1 - F_2^2)]}.$$

4. Results and Discussion

4.1. Effect of Absorber Pressure. The absorber pressure is the outlet pressure of ammonia-water turbine. If the absorber pressure is high, the working fluid cannot expand fully in the turbine, and both the power output and overall efficiency decrease in turn (Figures 2 and 3). Figure 4 shows that LEC increases with increasing absorber pressure. The reason is

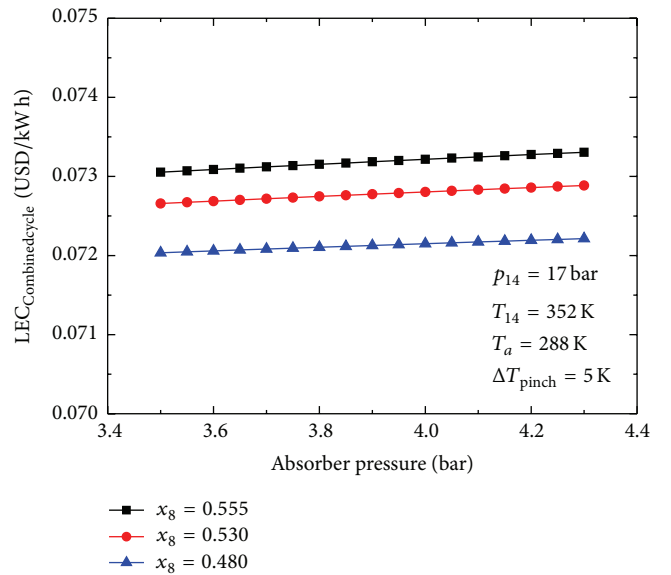


FIGURE 4: Variation of LEC of combined cycle with absorber pressure.

that the higher absorber pressure leads to less power output, which causes the increase in LEC. However, if absorber pressure is far less than 3.5 bar, the working fluid at the outlet of the absorber will change into vapor-liquid mixture. This increases the pump power consumption greatly. The relationships of $F(X)$ with the absorber pressure are demonstrated in Figure 5. $F(X)$ increases monotonically with increasing absorber pressure. Because the lowest $F(X)$ means the best performance, the lower absorber pressure is beneficial for the thermodynamic and economic performances.

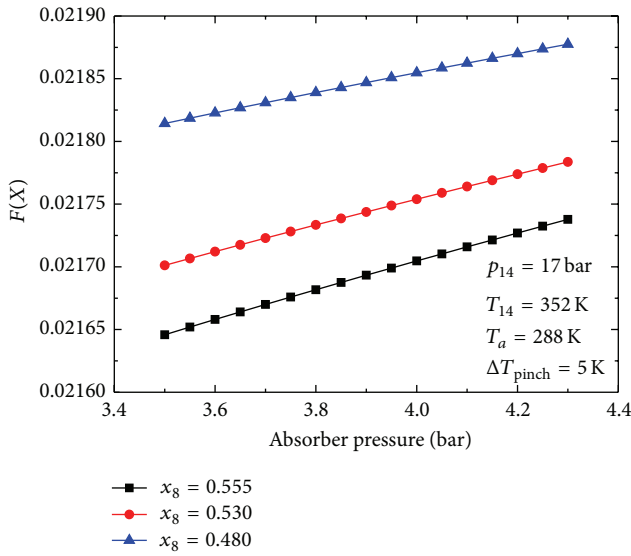


FIGURE 5: Variation of $F(X)$ of combined cycle with absorber pressure.

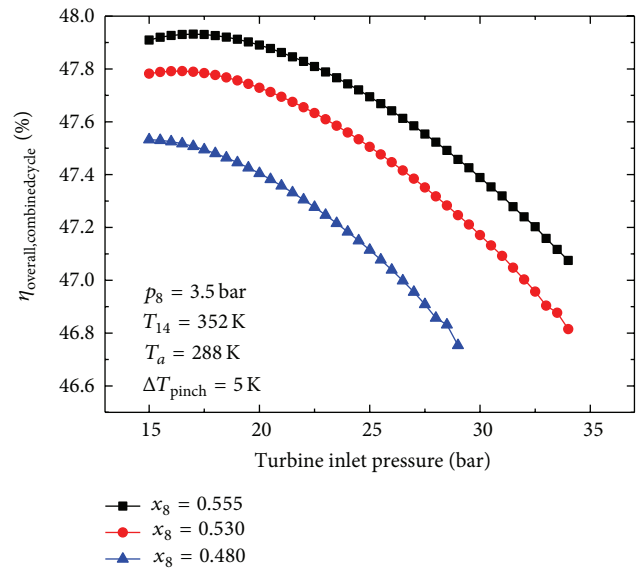


FIGURE 7: Variation of overall efficiency of combined cycle with turbine inlet pressure.

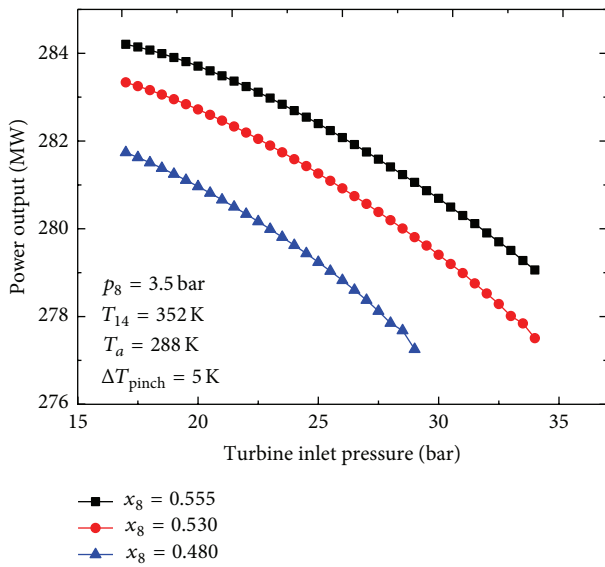


FIGURE 6: Variation of power output of combined cycle with turbine inlet pressure.

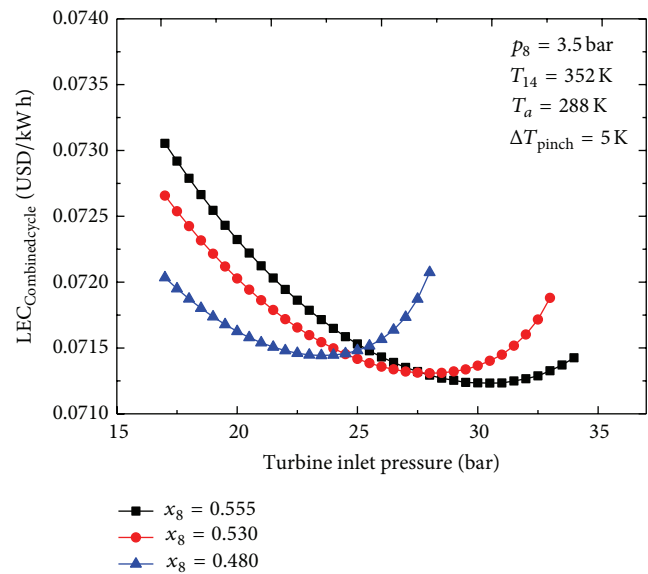


FIGURE 8: Variation of LEC of combined cycle with turbine inlet pressure.

4.2. *Effect of Turbine Inlet Pressure.* As shown in Figures 6 and 7, the variations of the power output and overall efficiency with the turbine inlet pressure are presented. The enthalpy drop across the turbine increases as the turbine inlet pressure increases. However, the enthalpy gains because of increasing turbine inlet pressure cannot compensate for the drop in the vapor flow rate. Thus, the turbine work output decreases. Owing to the decrease of vapor flow rate, both the cooling capacity and the equivalent work of cooling capacity (W_{cool}) increase first and then decrease. However, the equivalent work of cooling capacity is too little compared with the power output of the combined cycle. Hence, the power output and overall efficiency decrease with the increasing turbine inlet temperature.

As shown in Figure 8, LEC decreases at first and then increases with increasing turbine inlet pressure. When the ammonia mass fraction is 0.555, LEC reaches the minimum of 0.0712 USD/(kWh) with the turbine inlet pressure of 30.5 bar. Figure 9 shows that $F(X)$ decreases first and increases with the increasing turbine inlet pressure when the ammonia mass fraction is 0.53 or 0.555. Thus, an optimal turbine inlet pressure is present, and the optimal turbine inlet pressure value is changing with the ammonia mass fraction.

4.3. *Effect of Turbine Inlet Temperature.* Figure 10 shows that the power output increases with increasing turbine

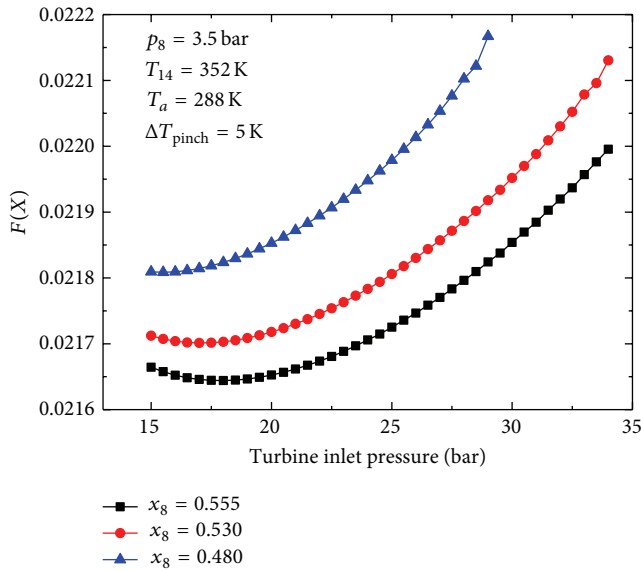


FIGURE 9: Variation of $F(X)$ of combined cycle with turbine inlet pressure.

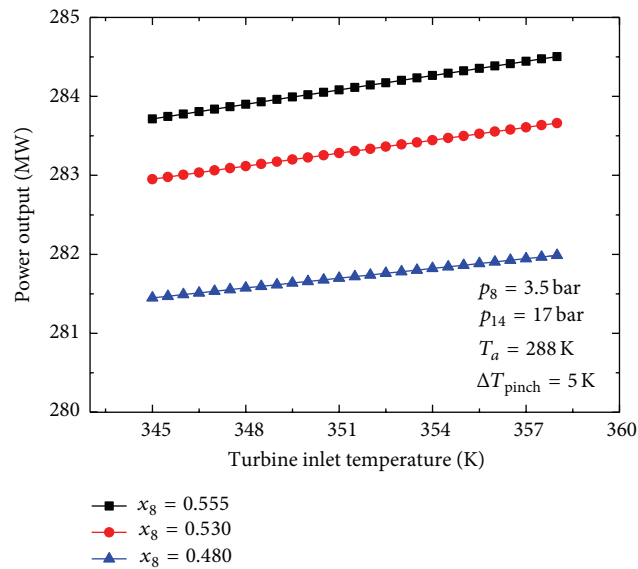


FIGURE 10: Variation of power output of combined cycle with turbine inlet temperature.

inlet temperature. With fixed pressure ratio, increase in inlet temperature leads to higher inlet enthalpy of working fluid. The exit enthalpy of working fluid also increases at the same time because of high exit temperature. But the increase in enthalpy caused by the increase in inlet temperature is more than that because of the increase in exit temperature. Hence, the turbine work output rises up as the turbine inlet temperature increases.

Because the increasing turbine inlet temperature increases cooler inlet temperature, the equivalent work of cooling capacity (W_{cool}) declines. However, the increase of power output compensates for the drop in the equivalent

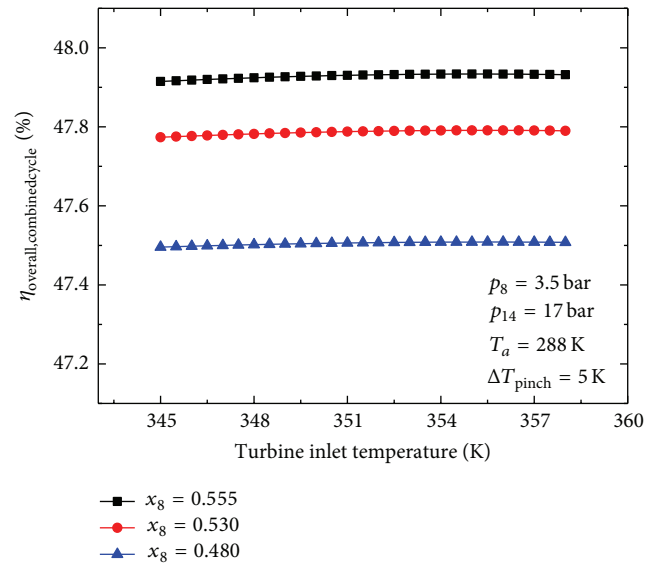


FIGURE 11: Variation of overall efficiency of combined cycle with turbine inlet temperature.

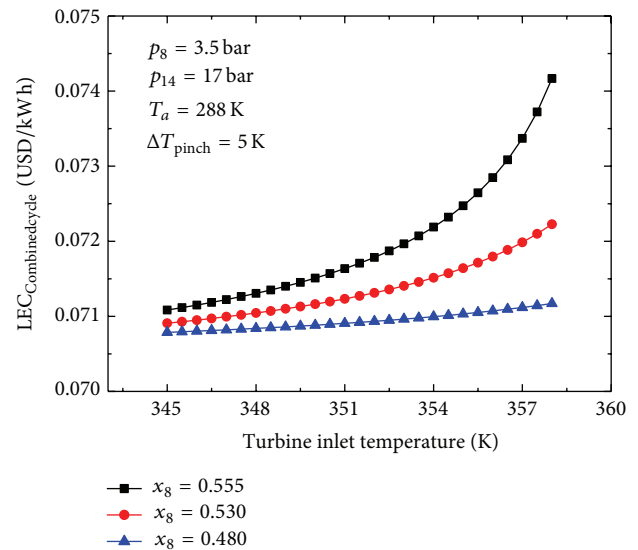


FIGURE 12: Variation of LEC of combined cycle with turbine inlet temperature.

work of cooling capacity. This fact results in the slight increase of overall efficiency (Figure 11).

As shown in Figure 12, LEC increases with increasing turbine inlet temperature monotonously. This fact implies that the lower inlet temperature results in better economic performance. Figure 13 shows that $F(X)$ changes very slightly when the turbine inlet temperature is lower than 253 K.

4.4. Effect of Ammonia Mass Fraction. Figures 14 and 15 reveal that the power output and overall efficiency will benefit from increased ammonia mass fraction. Increasing the ammonia mass fraction will improve the thermodynamic performance of the combined cycle because the higher the ammonia

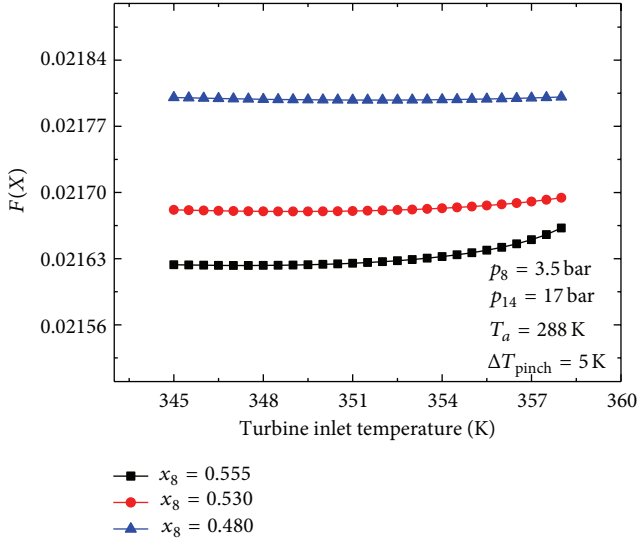


FIGURE 13: Variation of $F(X)$ of combined cycle with turbine inlet temperature.

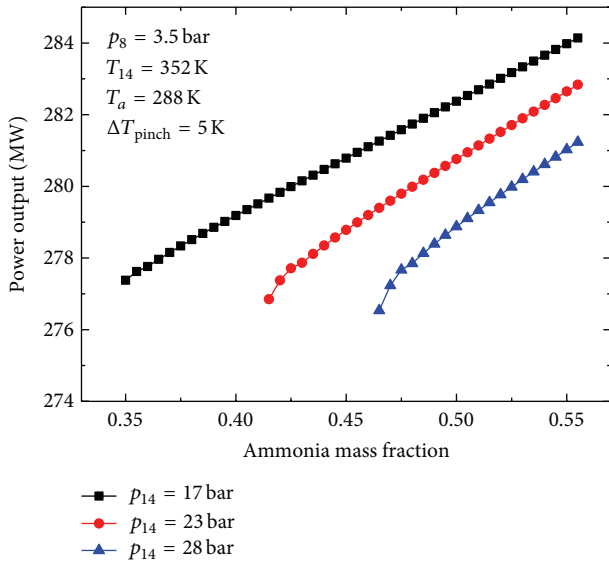


FIGURE 14: Variation of power output of combined cycle with ammonia mass fraction.

concentration, the greater the ammonia vapor flow rate expanding in the turbine. However, if the ammonia mass fraction is too high, the pump power consumption will increase greatly because the ammonia liquid mixture at the outlet of the absorber (state 8) will change into the vapor-liquid mixture.

Figure 16 shows the effect of ammonia mass fraction on LEC. With the increase of ammonia mass fraction, LEC decreases initially and then increases. The higher the turbine inlet pressure, the smaller the optimal ammonia mass fraction. When the turbine inlet pressure is 17 bar, LEC reaches the minimum of 0.0716 USD/(kWh) with an ammonia mass fraction of 0.405. When the turbine inlet pressure is 17 bar, LEC reaches the minimum of 0.0713 USD/(kWh) with

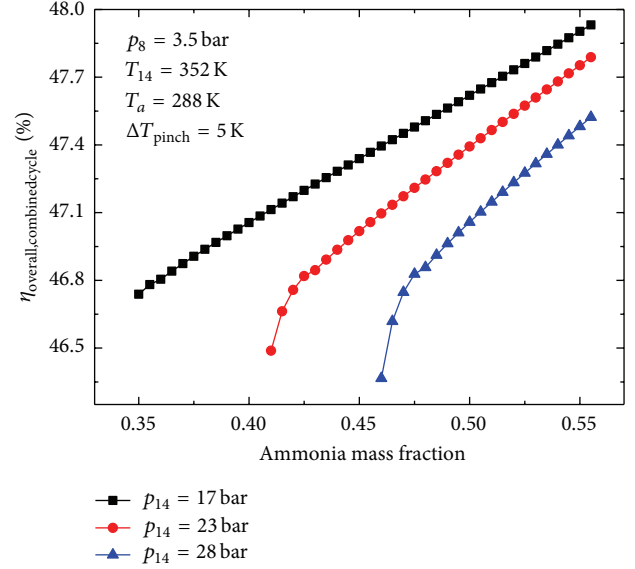


FIGURE 15: Variation of overall efficiency of combined cycle with ammonia mass fraction.

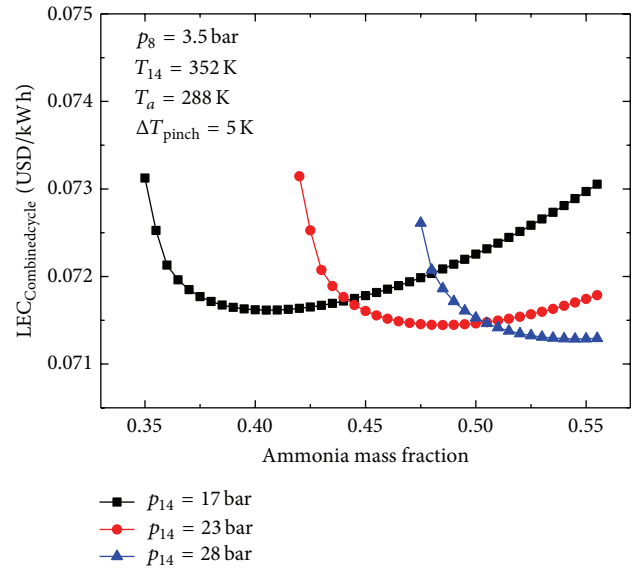


FIGURE 16: Variation of LEC of combined cycle with ammonia mass fraction.

an ammonia mass fraction of 0.545. Figure 17 presents the variations of $F(X)$ with ammonia mass fraction. $F(X)$ decreases rapidly with increasing ammonia mass fraction.

4.5. System Optimization. In this work, SA (Simulated Annealing) is employed to obtain the optimum combination of the key parameters. For the optimization, the constraints are simplified as follows:

Subject to:

$$17.0 \leq p_{14} \text{ (bar)} \leq 34.0,$$

$$345 \leq T_{14} \text{ (K)} \leq 375,$$

$$0.36 \leq x_8 \leq 0.555,$$

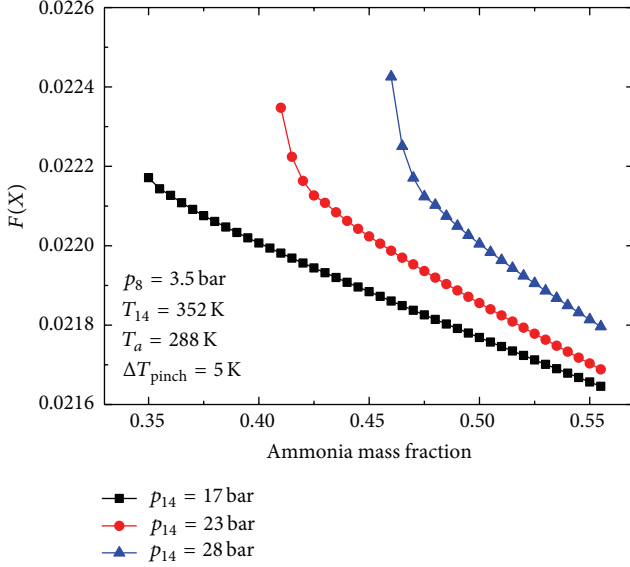


FIGURE 17: Variation of $F(X)$ of combined cycle with ammonia mass fraction.

$$288 \leq T_a \text{ (K)} \leq 300,$$

$$0 \leq \frac{m_{10}}{m_9} \leq 1,$$

$$0 \leq \frac{m_{12}}{m_1} \leq 1,$$

$$(T_{17} - T_{10}) \geq 5 \text{ K},$$

$$(T_4 - T_{11}) \geq 5 \text{ K},$$

$$(T_3 - T_{\text{Boiler}}) \geq 5 \text{ K},$$

$$T_{\text{Boiler}} \geq T_{\text{Rectifier}},$$

$$Q_{\text{cool}} > 0,$$

$$p_{14} \geq p_8.$$

(20)

The selection of the above-mentioned parameters for this optimization is according to the literatures [6, 9, 13].

Table 6 shows some results of the closed Brayton cycle. To compare the thermodynamic and economic performances of the combined cycle with those of the closed Brayton cycle, three parameters are defined as follows:

$$\begin{aligned} \text{RV}_{W_{\text{net}}} &= \frac{(W_{\text{net,Combinedcycle}} - W_{\text{net,Brayton}})}{W_{\text{net,Brayton}}}, \\ \text{RV}_{\eta_{\text{overall}}} &= \frac{(\eta_{\text{overall,Combinedcycle}} - \eta_{\text{overall,Brayton}})}{\eta_{\text{overall,Brayton}}}, \\ \text{RV}_{\text{LEC}} &= \frac{(\text{LEC}_{\text{Combinedcycle}} - \text{LEC}_{\text{Brayton}})}{\text{LEC}_{\text{Brayton}}}. \end{aligned} \quad (21)$$

TABLE 6: Results of the closed Brayton cycle.

Parameters	Value
Q_{core} (MW)	593.64
$\eta_{\text{overall,B}}$	46.6%
$W_{\text{net,B}}$ (MW)	276.90
LEC_B (USD/(kWh))	0.0711

TABLE 7: Optimization results.

Parameters	Optimization results
	$F(X) = 0.02164$
	$W_{\text{net,Combinedcycle}} = 283.56 \text{ MW}$,
	$\text{RV}_{W_{\text{net}}} = 2.41\%$
	$\eta_{\text{overall,Combinedcycle}} = 47.91\%$, $\text{RV}_{\eta_{\text{overall}}} = 2.43\%$
	$\text{LEC}_{\text{Combinedcycle}} =$
	$0.0706 \text{ USD}/(\text{kWh})$, $\text{RV}_{\text{LEC}} =$
	-0.73%

Table 7 lists the result of the parameters for the optimization. The optimized power output and overall efficiency for the combined cycle are 283.56 MW and 47.91%, respectively. These values are 2.41% and 2.43% higher than those of the closed Brayton cycle, respectively. Both the lower average heat addition temperature and the higher back pressure of turbine in AWM cycle result in less power output and lower overall efficiency of the combined cycle.

Comparing with closed Brayton cycle, the combined cycle reduces the LEC slightly. The optimized LEC of combined cycle is 0.73% lower than that of the closed Brayton cycle. The reason is that the AWM utilizes the waste heat and adds the power output and the cooling capacity to the closed Brayton cycle. However, the total capital investment increases due to the combined AWM system.

5. Conclusions

In this paper, a combined cycle, which combines AWM cycle and a nuclear closed Brayton cycle to recover the waste heat rejected from the pre-cooler, is proposed. A detailed parametric study and optimization are carried out for this combined cycle according to the thermodynamics and economics performances. The combined cycle can potentially be used to improve the power output and overall efficiency. The power output and overall efficiency of the combined cycle increase with increasing turbine inlet temperature and ammonia mass fraction, but the turbine inlet temperature and the ammonia mass fraction are limited by the heat source temperature and the absorb pressure, respectively. Compared with the closed Brayton cycle, the optimized power output and overall efficiency increase by 2.41% and 2.43%, respectively. LEC increases with decreasing absorber pressure and turbine inlet temperature. The optimized LEC of the combined cycle is 0.0706 USD/(kWh), which is 0.73% lower than those of the closed Brayton cycle.

Competing Interests

The authors declare that there are no competing interests regarding the publication of this paper and regarding the funding that they have received.

Acknowledgments

This present research was supported by the Chinese Natural Science Fund (Project no. 51306216) and the Fundamental Research Funds for the Central University (Project no. CDJ2R13140016).

References

- [1] A. Soroureddin, A. S. Mehr, S. M. S. Mahmoudi, and M. Yari, "Thermodynamic analysis of employing ejector and organic Rankine cycles for GT-MHR waste heat utilization: A Comparative Study," *Energy Conversion and Management*, vol. 67, pp. 125–137, 2013.
- [2] S. Dardour, S. Nisan, and F. Charbit, "Utilisation of waste heat from GT-MHR and PBMR reactors for nuclear desalination," *Desalination*, vol. 205, no. 1–3, pp. 254–268, 2007.
- [3] A. I. Kalina, "Combined-cycle system with novel bottoming cycle," *Journal of Engineering for Gas Turbines and Power*, vol. 106, no. 4, pp. 737–742, 1984.
- [4] D. Y. Goswami, "Solar thermal power technology: present status and ideas for the future," *Energy Sources*, vol. 20, no. 2, pp. 137–145, 1998.
- [5] D. S. Ayou, J. C. Bruno, R. Saravanan, and A. Coronas, "An overview of combined absorption power and cooling cycles," *Renewable and Sustainable Energy Reviews*, vol. 21, pp. 728–748, 2013.
- [6] R. V. Padilla, G. Demirkaya, D. Y. Goswami, E. Stefanakos, and M. M. Rahman, "Analysis of power and cooling cogeneration using ammonia-water mixture," *Energy*, vol. 35, no. 12, pp. 4649–4657, 2010.
- [7] S. Lu and D. Y. Goswami, "Optimization of a novel combined power/refrigeration thermodynamic cycle," *Journal of Solar Energy Engineering*, vol. 125, no. 2, pp. 212–217, 2003.
- [8] M. Pouraghaie, K. Atashkari, S. M. Besarati, and N. Nariman-zadeh, "Thermodynamic performance optimization of a combined power/cooling cycle," *Energy Conversion and Management*, vol. 51, no. 1, pp. 204–211, 2010.
- [9] G. Demirkaya, R. Vasquez Padilla, D. Y. Goswami, E. Stefanakos, and M. M. Rahman, "Analysis of a combined power and cooling cycle for low-grade heat sources," *International Journal of Energy Research*, vol. 35, no. 13, pp. 1145–1157, 2011.
- [10] L. S. Vieira, J. L. Donatelli, and M. E. Cruz, "Exergoeconomic improvement of a complex cogeneration system integrated with a professional process simulator," *Energy Conversion and Management*, vol. 50, no. 8, pp. 1955–1967, 2009.
- [11] Z. Shengjun, W. Huaixin, and G. Tao, "Performance comparison and parametric optimization of subcritical Organic Rankine Cycle (ORC) and transcritical power cycle system for low-temperature geothermal power generation," *Applied Energy*, vol. 88, no. 8, pp. 2740–2754, 2011.
- [12] T. Guo, H. X. Wang, and S. J. Zhang, "Fluids and parameters optimization for a novel cogeneration system driven by low-temperature geothermal sources," *Energy*, vol. 36, no. 5, pp. 2639–2649, 2011.
- [13] A. Coskun, A. Bolatturk, and M. Kanoglu, "Thermodynamic and economic analysis and optimization of power cycles for a medium temperature geothermal resource," *Energy Conversion and Management*, vol. 78, pp. 39–49, 2014.
- [14] V. Zare, S. M. S. Mahmoudi, and M. Yari, "On the exergoeconomic assessment of employing Kalina cycle for GT-MHR waste heat utilization," *Energy Conversion and Management*, vol. 90, pp. 364–374, 2015.
- [15] K. Bahlouli, R. Khoshbakhti Saray, and N. Sarabchi, "Parametric investigation and thermo-economic multi-objective optimization of an ammonia-water power/cooling cycle coupled with an HCCI (homogeneous charge compression ignition) engine," *Energy*, vol. 86, pp. 672–684, 2015.
- [16] Y. Feng, Y. Zhang, B. Li, J. Yang, and Y. Shi, "Sensitivity analysis and thermoeconomic comparison of ORCs (organic Rankine cycles) for low temperature waste heat recovery," *Energy*, vol. 82, pp. 664–677, 2015.
- [17] F. Xu, D. Y. Goswami, and S. S. Bhagwat, "A combined power/cooling cycle," *Energy*, vol. 25, no. 3, pp. 233–246, 2000.
- [18] F. Xu and D. Y. Goswami, "Thermodynamic properties of ammonia-water mixtures for power-cycle applications," *Energy*, vol. 24, no. 6, pp. 525–536, 1999.
- [19] M. S. El-Genk and J.-M. Tournier, "Noble gas binary mixtures for gas-cooled reactor power plants," *Nuclear Engineering and Design*, vol. 238, no. 6, pp. 1353–1372, 2008.
- [20] F. W. Yu, K. T. Chan, R. K. Y. Sit et al., "Review of standards for energy performance of chiller systems serving commercial buildings," *Energy Procedia*, vol. 61, pp. 2778–2782, 2014.
- [21] S. Nisan and S. Dardour, "Economic evaluation of nuclear desalination systems," *Desalination*, vol. 205, no. 1–3, pp. 231–242, 2007.
- [22] L. E. Herranz, J. I. Linares, and B. Y. Moratilla, "Power cycle assessment of nuclear high temperature gas-cooled reactors," *Applied Thermal Engineering*, vol. 29, no. 8–9, pp. 1759–1765, 2009.
- [23] H. D. Madhawa Hettiarachchi, M. Golubovic, W. M. Worek, and Y. Ikegami, "Optimum design criteria for an Organic Rankine cycle using low-temperature geothermal heat sources," *Energy*, vol. 32, no. 9, pp. 1698–1706, 2007.
- [24] Y. T. Zhu, W. H. Qu, and P. Y. Yu, *Chemical Equipment Design Manual*, Chemical Industry Press, 2005.
- [25] Q. Songwen, *Heat Exchanger Design Handbook*, Chemical Industry Press, 2002.
- [26] R. Turton, R. C. Bailie, W. B. Whiting et al., *Analysis, Synthesis and Design of Chemical Processes*, Prentice Hall, Upper Saddle River, NJ, USA, 1997.
- [27] F. Táboas, M. Vallès, M. Bourouis, and A. Coronas, "Flow boiling heat transfer of ammonia/water mixture in a plate heat exchanger," *International Journal of Refrigeration*, vol. 33, no. 4, pp. 695–705, 2010.
- [28] L. Xiao, S.-Y. Wu, T.-T. Yi, C. Liu, and Y.-R. Li, "Multi-objective optimization of evaporation and condensation temperatures for subcritical organic Rankine cycle," *Energy*, vol. 83, pp. 723–733, 2015.
- [29] C. E. Campos Rodríguez, J. C. Escobar Palacio, O. J. Venturini et al., "Exergetic and economic comparison of ORC and Kalina cycle for low temperature enhanced geothermal system in Brazil," *Applied Thermal Engineering*, vol. 52, no. 1, pp. 109–119, 2013.
- [30] D. Mignard, "Correlating the chemical engineering plant cost index with macro-economic indicators," *Chemical Engineering Research and Design*, vol. 92, no. 2, pp. 285–294, 2014.

- [31] <http://www.neimagazine.com/news/newsnuclear-reactor-performance-by-vendors-agrs-23>.
- [32] H. W. Tang, *Practical Introduction to Mathematical Programming*, Dalian Institute of Technology Press, 1986.
- [33] V. Zare, S. M. S. Mahmoudi, and M. Yari, "An exergoeconomic investigation of waste heat recovery from the Gas Turbine-Modular Helium Reactor (GT-MHR) employing an ammonia-water power/cooling cycle," *Energy*, vol. 61, pp. 397–409, 2013.

Research Article

A Study on the Instantaneous Turbulent Flow Field in a 90-Degree Elbow Pipe with Circular Section

Shiming Wang,¹ Cheng Ren,¹ Yangfei Sun,¹ Xingtuan Yang,¹ and Jiyuan Tu^{1,2}

¹*Institute of Nuclear and New Energy Technology, Tsinghua University, Collaborative Innovation Center of Advanced Nuclear Energy Technology, Key Laboratory of Advanced Reactor Engineering and Safety of Ministry of Education, Beijing 100084, China*

²*School of Aerospace, Mechanical & Manufacturing Engineering, RMIT University, Melbourne, VIC 3083, Australia*

Correspondence should be addressed to Xingtuan Yang; yangxt@mail.tsinghua.edu.cn

Received 22 March 2016; Accepted 8 May 2016

Academic Editor: Xin Tu

Copyright © 2016 Shiming Wang et al. This is an open access article distributed under the Creative Commons Attribution License, which permits unrestricted use, distribution, and reproduction in any medium, provided the original work is properly cited.

Based on the special application of 90-degree elbow pipe in the HTR-PM, the large eddy simulation was selected to calculate the instantaneous flow field in the 90-degree elbow pipe combining with the experimental results. The characteristics of the instantaneous turbulent flow field under the influence of flow separation and secondary flow were studied by analyzing the instantaneous pressure information at specific monitoring points and the instantaneous velocity field on the cross section of the elbow. The pattern and the intensity of the Dean vortex and the small scale eddies change over time and induce the asymmetry of the flow field. The turbulent disturbance upstream and the flow separation near the intrados couple with the vortexes of various scales. Energy is transferred from large scale eddies to small scale eddies and dissipated by the viscous stress in the end.

1. Introduction

With the increasing acute global energy crisis, more and more attention is paid to seek a green environment-friendly and low-carbon development pattern. Nuclear energy is identified as a competitive alternative in the energy markets. The uranium-based, graphite-moderated, helium-cooled pebble bed reactor high temperature reactor (HTR) has been proved to be one of the most promising nuclear power projects in China due to its high efficiency, attractive economics, high levels of passive safety, and potential usage for hydrogen production [1]. Also, some test reactors, such as AVR in Germany [2], MPBR in USA [3], and PBMR in South Africa [4], have been demonstrated around the world. The Chinese high-temperature gas-cooled reactor-pebble bed module (HTR-PM) demonstration project, oriented by Institute of Nuclear and New Energy Technology of Tsinghua University (INET), is very attractive and competitive in the nuclear power market and is going well [5].

The HTR-PM has one steam turbine-generator and two independent primary loops, which have the same construction design and are arranged in the so-called “side-by-side”

way [6]. Both of the loops have their own reactor modules and steam generators, as shown in Figure 1(a). The helium in the loop is heated to 750°C by the high temperature fuel spheres in the core of the reactor and flows into the chamber of the spiral tube exchanger in the steam generator through the inner pipe of the coaxial hot gas duct. Then the hot helium releases its thermal power to the water in the secondary loop and is cooled down to around 250°C. The cooled helium from 14 riser pipes collects into the header box and is pumped back to the reactor by the blower. Each of the riser pipes is connected to the header box by a 90° elbow, as shown in Figure 1(b), which is used as the sensor to measure the helium flow rate by monitoring the pressure difference between its intrados and extrados [7–9].

The elbow sensor does not introduce any additional pressure loss in the pipe system other than that already caused by the elbow. As an enormous amount of heat must be extracted out of the core, enough helium is needed to meet the requirement. Hence, the accurate measurement of helium gas flow rate in the primary loop is closely related to the safe operation and power control of the reactor system. Considering that the elbows arranged behind the riser pipes

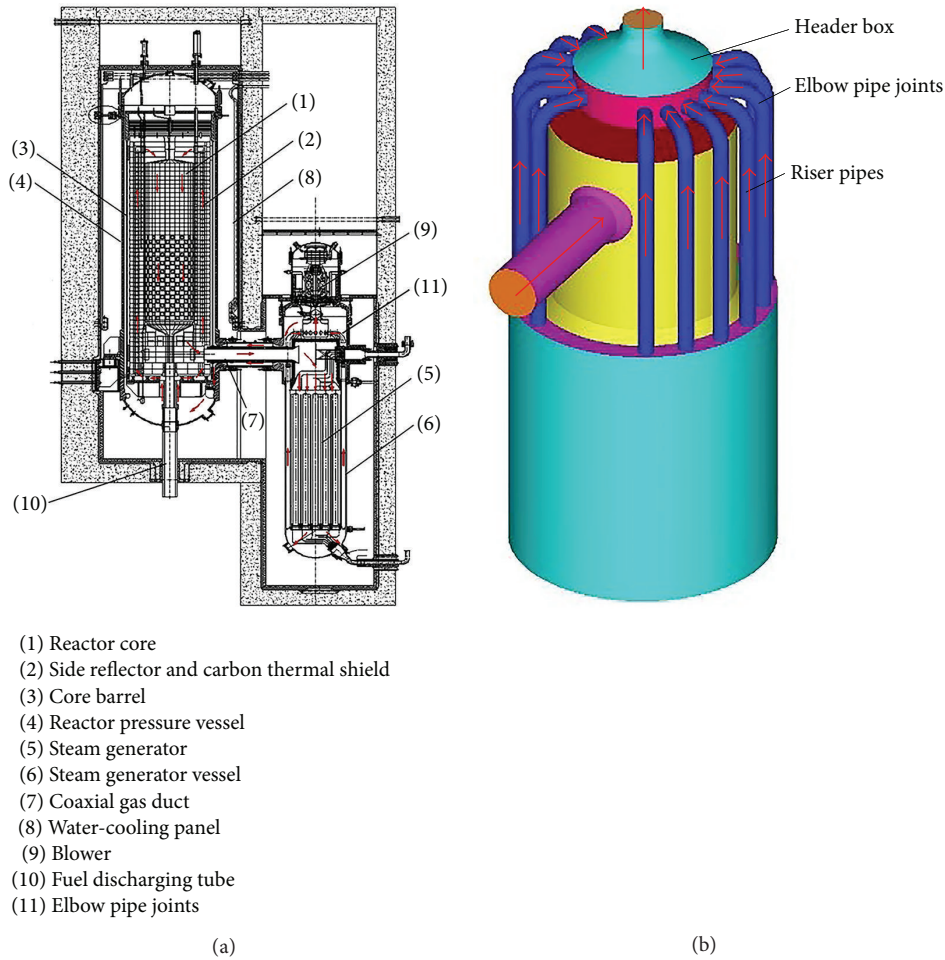


FIGURE 1: The structure configuration of the HTR-PM. (a) Primary system of the HTR-PM. (b) The 3D model of the flow concentration system.

is used as the sensor to measure the helium flow rate, the characteristics of the turbulent flow in a 90° elbow must be studied to guarantee the accuracy and reliability.

In a 90° elbow, the central parts of the flow which go more rapidly are forced outwards by the centrifugal actions, while the slower parts near the extrados are forced inwards to the intrados along the circumference wall by the pressure difference between extrados and intrados. Then the so-called secondary flow takes place in either a clockwise or an anticlockwise sense about the axis [10, 11]. These behaviors induce a squeeze effect to the extrados and a suction effect to the intrados. Along with the flow separation occurring on the intrados, the instantaneous velocity field and pressure field in the elbow turned out to be very complicated.

The development of secondary flow and flow separation is classified as transient process. The interaction between them and the turbulent disturbance from upstream are factors of significant influence on the flow field. There have been a number of representative studies on the flow field in elbow pipes due to the progresses in both computational fluid dynamics and experimental methods. Pigott [12], Kirchbach [13], and Schubart [14] measured the pressure drop of flowing through a 90° elbow and provide the detailed results including the

methods used to calculate the elbow pipe pressure drop. Enayet et al. [15] and Sudo et al. [16] investigated the turbulent flow in a circular-sectioned 90° elbow by using laser Doppler velocimetry and single inclined hot wire, respectively. Eguchi et al. [17] applied the LES method to simulate the high-Re flow in a short-elbow pipe and the mechanism of the pressure fluctuation and the origin of the fluid force were discussed. And the same method was utilized by Rütten et al. [18, 19] to investigate the unsteady flow separation, unstable shear layers, and an oscillation of the Dean vortices in 90° elbow pipes.

However, there are few works on the asymmetry of the instantaneous pressure field and velocity field in 90° elbow pipes. Tunstall and Harvey [20] studied the fully developed turbulent flow through a mitred sharp bend experimentally and declared that the secondary flow was dominated by a single circulation about the axis in either a clockwise or an anticlockwise sense, between which it switches abruptly at a low, random frequency. Ono et al. [21] investigated the influence of elbow curvature on flow structure by using PIV method and concluded that the separation region was generated constantly in short elbows but was formed intermittently in long elbows. All of the characteristics mentioned above

have significant influence on the flow field in the elbow, which is the critical factor to decide the helium flow rate in the HTR-PM. Unfortunately, these studies are limited only to global flow field structure. Little attention has been paid to the local instantaneous information of turbulent flow in 90° elbow pipes.

Under general operation conditions (250°C, 7.0 MPa), the velocity of helium in the riser pipes of HTR-PM reaches 24.69 m/s, to which h , the corresponding Reynolds number, is about 1.3×10^6 . Considering the limitation of the drive capability of the pump arranged in the experimental loop, too large Reynolds number cannot be achieved in our experiments. So the focus of this paper is concentrated on the detailed information on instantaneous pressure field and velocity field through a circular-sectioned 90° elbow but not on simulating the working condition in the HTR-PM. The purpose is achieved by applying the large eddy simulation approach coupled with experimental data and RANS results.

In the following, the experimental apparatus and numerical description are explained in detail. The accuracy of the numerical method is demonstrated by comparing numerical and experimental findings. Detailed information on the instantaneous flow field is analyzed by a detailed discussion of the instantaneous pressure and velocity distribution on the cross section of the elbow.

2. Experimental Apparatus

The compressibility of helium can be left out of account due to the relatively low velocity in the practical situation of HTR-PM, to which the corresponding Mach number is less than 0.3. Hence, the incompressible helium flow can be imitated by the water flow in specific test loop.

The experiments were conducted on a self-built water circulating loop. The experimental section is illustrated in Figure 2. The configuration of the test pipe is circular and its inner diameter, d , is 80 mm. It is made up of a 90° elbow of curvature radius $R = 120$ mm and two straight pipes in the upstream tangent and downstream tangent with the length of $L_{up,exp} = L_{down,exp} = 30d$. The upstream and downstream tangents are arranged long enough to eliminate the disturbance generated by chokes or bends upstream and to guarantee the full development of turbulent flow downstream. The ratio of bending radius to diameter is 1.5 to mimic the geometric construction of elbows utilized in HTR-PM. The test section was arranged in vertical plane. The water flows along the horizontal and then turns to vertical due to the constraints of the elbow. The circulation is sustained by the constant pressure difference between the elevated water tank and the storage tank at lower place to guarantee the stable and continual flow. The flow rate is adjusted by the electric control valve located downstream of the test section and is measured by an electromagnetic flowmeter installed on the horizontal pipe. The water in the storage tank is pumped to the elevated water tank by a variable frequency pump.

There are 8 pressure tappings scattered along the intrados and extrados of the elbow at different bending angle α and 4 tappings scattered on the inner and outer side of the downstream tangent, as illustrated in Figure 2. The

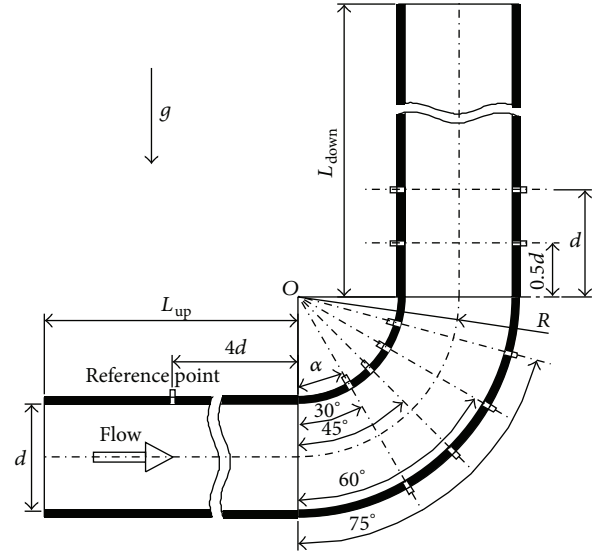


FIGURE 2: The arrangements of tappings on the test section.

pressure difference, ΔP , between each of the 12 tappings and the identical pressure reference point was measured by identical Rosemount 3051S pressure difference transmitter, whose accuracy was within 0.04%. The pressure reference point is located $4d$ upstream of the inlet of the elbow. Also, the system pressure and temperature were measured to decide the physical property parameter of water.

Measurements were performed for a water flow with the bulk mean velocity $U = 0.5$ m/s, to which the corresponding Reynolds number was 44805. Special attention has been paid to decreasing the measuring error, like averaging the observed values of different measurements and maintaining the stability of the power supply.

3. Numerical Description

3.1. Geometrical Model and Mesh Division. The computational domain extracted from the experimental apparatus has the same geometric parameters with the test section except the length of upstream and downstream tangents, which were shortened to $L_{up,num} = 3d$ and $L_{down,num} = 5d$, respectively, to reduce the computational amount. This reduction can be acceptable owing to the undisturbed flow upstream in the numerical case, and it was proved to be applicable by comparing the results to the experimental data.

Great care must be taken when setting the size, Δs , of the wall-normal mesh near the wall because the flow characteristics in the boundary layer near the wall may interact with the flow separation at an intense level. Eguchi et al. [22] claimed that, under the condition of a fully developed velocity profile, the relation between Re and the pipe diameter in terms of the wall unit, D^+ , was described as below:

$$Re = \frac{\rho d U}{\mu} = D^+ \left\{ \frac{1}{\kappa} \left[\ln(2D^+) - \frac{\pi}{2} - \frac{4}{3} \right] + B \right\}. \quad (1)$$

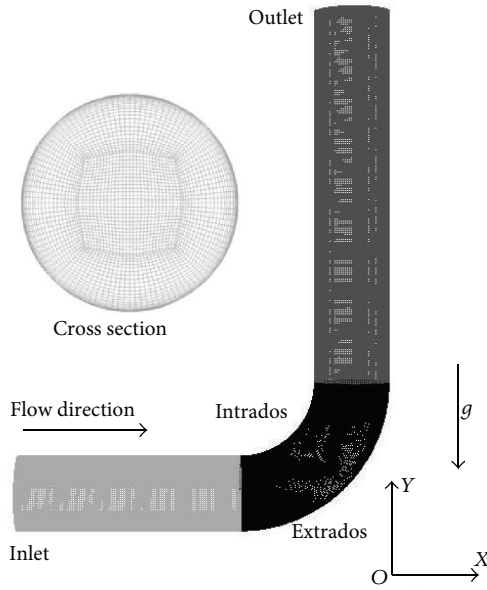


FIGURE 3: Computational geometry and finite element mesh employed.

Here, the constants κ and B are the same as those in the widely used wall law, that is, typically 0.4 and 5.5. D^+ is the pipe diameter in terms of the wall unit and is obtained by

$$D^+ = \frac{du_\tau}{\nu}, \quad (2)$$

where u_τ is the friction velocity and ν is the kinematic viscosity. The required mesh size normalized by the pipe diameter can be roughly estimated as

$$\frac{\Delta s}{d} = \frac{\Delta s^+}{D^+} = \frac{2}{D^+} \quad (3)$$

according to Piomelli and Balaras [23]. Then the required mesh size is obtained as illustrated in (1) and (3), which suggests that $\Delta s/d$ should be approximately 8×10^{-4} at $Re = 44805$ for a resolved LES computation. Therefore, the mesh size normal to the wall was set to $0.0001d$ in the present mesh design to satisfy the requirements of LES via ICEM CFD software. The entirety of the domain was divided into about 3.13 million hexahedral elements finally, as illustrated in Figure 3.

In this paper, the main attention is paid to the influence of the large scale vortexes induced by the elbow on the instantaneous flow field. Hence, the mesh scales are designed elaborately to catch the main information of large scale vortexes. y^+ check was made after the calculation. The vast majority of y^+ is less 1 and the maximum is 2.5 only distributed on minority of the intrados of the elbow. By comparing with the experimental results, the mesh strategy was proved to be fine enough to capture the pressure characteristics adjacent to the wall.

3.2. Numerical Model and Boundary Conditions. The large eddy simulation method embedded in ANSYS FLUENT 14.5

software was used to solve the incompressible Navier-Stokes equations for the instantaneous flow field. In LES, large eddies are resolved directly, while small eddies are modeled. The governing equations for LES employ the Boussinesq hypothesis as in the RANS models. The dynamic Smagorinsky-Lilly model was selected to model eddy viscosity because of the fact that the Smagorinsky model constant, C_S , can be dynamically computed based on the information provided by the resolved scales of motion. The dynamic procedure therefore obviates the need for users to specify the model constant in advance. Also, the RNG $k - \epsilon$ model based on the second-order center-difference scheme was utilized to calculate the RANS results which was compared with the LES results.

We have assumed steady inlet velocity without any temporal fluctuation superimposed and the spatial variations of velocity were taken into consideration. This is mainly because the inlet disturbance is expected to be low due to the long straight pipe arranged before the elbow. For purpose of comparing the numerical results with the experimental data, the boundary conditions of the simulation cases were set identically with the experimental cases. A steady state flow in a $12.5d$ long straight pipe with the same diameter d and inlet velocity U was also solved by using the RNG $k - \epsilon$ model. The velocity profile on the cross section located $2d$ upstream of the outlet of the straight pipe was set as the velocity inlet boundary conditions for the inlet of the elbow. A nonslip boundary condition was employed for the wall boundary and the pressure outlet was inducted for the outlet. There is no heat transfer happening in the computational domain.

Water at ambient conditions (25°C , 0.1MPa) was used as the working fluid ($\rho = 997\text{kg/m}^3$ and $\mu = 890 \times 10^{-6}\text{kg/(m}\cdot\text{s)}$) in the simulation cases. Turbulent intensity ($I = 0.16Re^{-1/8}$) based on the elbow pipe diameter was specified for an initial assumption of turbulent quantities.

4. Results and Discussion

4.1. Longitudinal Distribution of Wall Static Pressure. Nondimensional pressure difference normalized by $0.5\rho U^2$, namely, the pressure coefficient, C_p , was introduced to describe the longitudinal distribution of wall static pressure. The wall static pressure at various α values gained from LES method, experiments, and RANS method is illustrated against the locations along the flow direction in Figure 4. The results of LES method were time-averaged to meet the requirement for comparison. Figure 4 shows that the results of LES method are in good agreement with that of experiments and RANS method between $\alpha = 10^\circ$ and 90° . The accuracy of the LES results is verified and more effective information of the flow field can be extracted from the LES results.

Upstream of $\alpha = 10^\circ$ and downstream of $\alpha = 90^\circ$, the LES results are relatively smaller than that of RANS method but more close to the experimental data. The deviation between the three methods is induced by their own characteristics. For experiments, the tappings drilled in the wall change the surface structure to some degree. This exerts an influence on the boundary layer flow. RANS method solves the time-averaged equations of motion for fluid flow and loses some

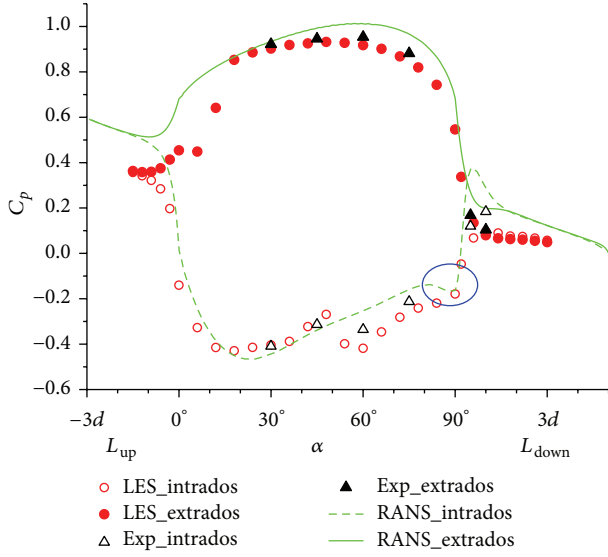


FIGURE 4: Longitudinal distribution of wall static pressure.

of the transient information. However, the LES method takes the interactions among the various scale vortexes into consideration and accords with the actual conditions.

Under the impact of the centrifugal force produced throughout the swerve, the extrados is squeezed and the intrados is sucked, both by the fluid flowing outwards to the outer wall. This induces a pressure swell on the extrados and leads to a pressure sink on the intrados along the flow direction, just as shown in Figure 4.

Before $L_{up} = -1.5d$, the flow is not yet disturbed by the elbow and the wall static pressures on the inner wall and the outer wall remain equal. However, the static pressure on extrados exceeds that on intrados rapidly after this location. Temporary pressure increase and pressure decrease occur, respectively, on the extrados and intrados. At the location of $\alpha = 60^\circ$ on extrados, the static pressure is up to its maximum. Hence, the fluid near the extrados between the location of $L_{up} = -1.5d$ and that of $\alpha = 60^\circ$ is decelerated slightly due to the adverse pressure gradient. Simultaneously, at the location of $\alpha = 25^\circ$, the static pressure on the intrados reaches its minimum and the fluid between the location of $L_{up} = -1.5d$ and that of $\alpha = 25^\circ$ is accelerated in accordance with the positive pressure gradient.

Downstream of the location of $L_{down} = d$, the distorted wall static pressure begins to recover and ends up with a uniform pressure field. Then between the location of $\alpha = 60^\circ$ and that of $L_{down} = d$, the fluid near the extrados is accelerated slightly because of the positive pressure gradient, while, the fluid near the intrados is decelerated according to the adverse pressure gradient between the location of $\alpha = 25^\circ$ and that of $L_{down} = d$.

On the intrados, between $\alpha = 80^\circ$ and 90° , the static pressure has a little subsidence, as marked in blue in Figure 4. The abnormality is caused by the flow separation occurring near the intrados. The recirculation zone has two stagnation points, of which the velocities are both zero. And at the

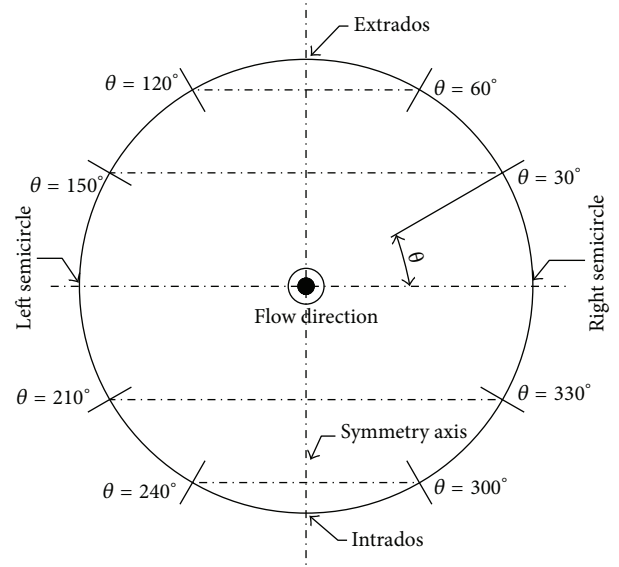


FIGURE 5: The distribution of pressure monitoring points on the cross section.

middle of the recirculation zone, the back-flow velocity is relatively high. Then the pressure here is lower than other locations in the zone according to the Bernoulli equation.

4.2. Circumferential Distribution of Wall Static Pressure. Wall static pressure on specific locations is extracted from the LES results. The schematic diagram of the distribution of the pressure monitors on the circumference of the cross section at different bending angle α is illustrated in Figure 5. There are 8 monitors distributed on each circumference. Every two of them, which are located at the same level, form a symmetric point pair and are connected to each other by a horizontal center line, just as shown in Figure 5.

The fluctuation of pressure on the wall makes it especially hard to compare the instantaneous pressures on the monitors at a specific time, while, a global time-averaged value of LES results will lose all of the instantaneous information. So a short-time-averaged method was introduced to make the comparison realizable. In this paper, we randomly intercepted a continuous data flow with a length of 2 seconds from the integral LES results. The intercepted data was averaged over time and this conduct made it feasible to compare the instantaneous pressures without losing instantaneous information. The comparison of the static pressure on the symmetric point pair is shown in Table 1, where $\overline{C_{p1}}$ and $\overline{C_{p2}}$ represent the short-time-averaged results of the pressure coefficient on the monitors distributed on left and right semicircle, respectively, and $\overline{C_p}$ is the mean of $\overline{C_{p1}}$ and $\overline{C_{p2}}$. The relative deviation δ is described as

$$\delta = \frac{|\overline{C_{p1}} - \overline{C_{p2}}|}{\overline{C_p}}. \quad (4)$$

For the cross section sliced at $\alpha = 36^\circ, 48^\circ, 60^\circ$, and 78° , the relative deviation δ related to the symmetric point

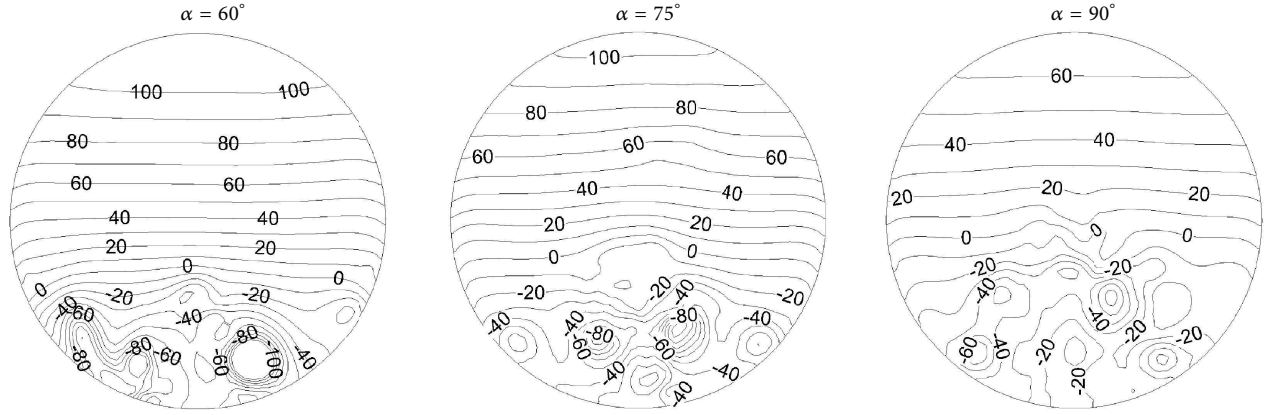


FIGURE 6: The pressure contours on the cross sections of the elbow (Pa): $t = 5$ s.

TABLE 1: The comparison of static pressures on symmetric point pair.

α		θ_1	$\overline{C_{p1}}$	θ_2	$\overline{C_{p2}}$	$\overline{C_p}$	Relative deviation δ
36°	Upper	120°	0.864	60°	0.869	0.866	0.27%
		150°	0.703	30°	0.697	0.700	0.43%
	Lower	210°	-0.044	330°	-0.074	-0.059	25.50%
		240°	-0.610	300°	-0.669	-0.640	4.60%
48°	Upper	120°	0.871	60°	0.879	0.875	0.42%
		150°	0.700	30°	0.684	0.692	1.13%
	Lower	210°	0.018	330°	0.029	0.023	23.76%
		240°	-0.740	300°	-0.777	-0.759	2.48%
60°	Upper	120°	0.854	60°	0.856	0.855	0.12%
		150°	0.665	30°	0.667	0.666	0.15%
	Lower	210°	-0.169	330°	-0.128	-0.148	13.97%
		240°	-0.458	300°	-0.455	-0.456	0.33%
78°	Upper	120°	0.758	60°	0.760	0.759	0.14%
		150°	0.561	30°	0.569	0.565	0.70%
	Lower	210°	-0.222	330°	-0.242	-0.232	4.21%
		240°	-0.340	300°	-0.330	-0.335	1.51%

pairs on the upper semicircle is quite small. This indicates that the instantaneous pressure distribution on the upper semicircle of the cross section is symmetrical. However, δ related to the symmetric point pairs on the lower semicircle is relatively large, especially to the pairs whose θ is 210° and 330°, as marked by bold font in Table 1. δ related to this pair is about 3~10 times larger than that related to other pairs and decreases gradually along with the increasing of α . The asymmetry of the instantaneous pressure distribution on the lower semicircle of the cross section is caused by the counterrotating vortices with different swirling intensity and the flow separation occurring near the intrados. The separation grows stronger gradually along with the flow developing downstream and interacts with the counterrotating vortices. Large scale vortices are broken into small scale vortices. The momentum and energy are transferred among them and the

fluctuation energy is dissipated rapidly, which is conducive to the recovery of the distorted pressure field.

The pressure contours on the cross section sliced at $\alpha = 60^\circ$, 75° , and 90° are illustrated in Figure 6. The data was extracted at the time $t = 5$ s. The static pressure value demonstrated here refers to the pressure of the outlet of the domain. Corresponding to the former conclusion, the pressure field of the cross section is symmetrical in the upper semicircle and asymmetrical in the lower semicircle.

Figure 6 indicates that the zone of disturbed pressure distribution spreads towards the upper part along with the increasing of α . And the asymmetrical area of the instantaneous pressure field extends gradually. Simultaneously, the contours thin and the difference between the maximum and minimum of the contours diminishes gradually. In conclusion, the instantaneous pressure distribution on the cross section is no longer globally symmetrical due to the secondary flow and the flow separation. The influence of flow separation on the flow field focuses on the lower semicircle. Along with the development of flowing, the instantaneous pressure distribution has a tendency to homogenize.

4.3. The Velocity Vector Fields on the Cross Section. The velocity vector fields projected onto the cross sections sliced at $\alpha = 60^\circ$, 75° , and 90° are illustrated in Figure 7. The fluid near the axis of symmetry is forced to flow towards the extrados under the impact of the centrifugal force, while the fluid near the wall of left and right semicircles is transported to the intrados along the circumferential wall under the differential pressure. Then, the large scale vortices rotating in contrary direction come up in the elbow, known as the Dean vortex.

On the lower semicircle of the cross sections sliced at $\alpha = 60^\circ$ and 75° , two counterrotating vortices with small scale are observed. These vortices are induced by the relatively high intensity secondary flow near the intrados. Figure 6 shows that a low pressure area presents at the intrados. Then the fluid adjacent to the left and right semicircle wall is accelerated by the pressure difference near the intrados. When it comes to the appropriate location at the lower semicircle, the fluid deflects towards extrados rapidly and

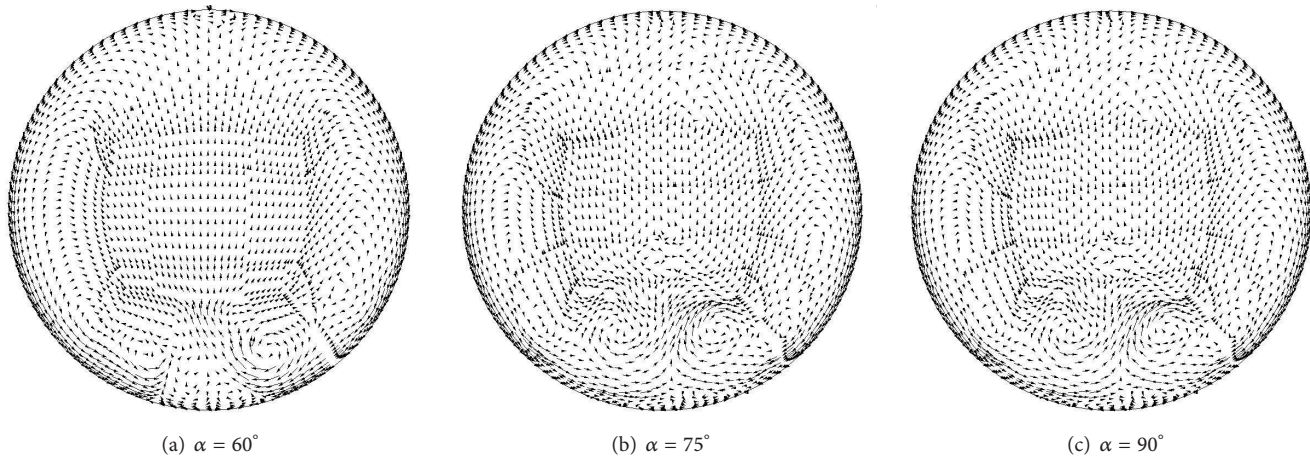


FIGURE 7: The velocity vector fields on the cross section: $t = 5$ s, $U = 0.5$ m/s.

flows away. In the process, the fluid that is deflecting with relatively high velocity rotates the neighbouring fluid through the shearing action and promotes the generation of the two vortices in the end. The cores of the two vortices are of axial symmetry but the intensity of them has some difference. On the cross section at $\alpha = 75^\circ$, the two vortices interact with each other to some degree. Their velocity fields begin to merge and the location of the cores moves to an upper level comparing to that of the section at $\alpha = 60^\circ$.

The flow field of the lower semicircle of the cross section at $\alpha = 90^\circ$ is more complicated than that upstream. Secondary vortices with smaller scale are observed in this section. These vortices are the outcome of the interaction between the secondary flow and the separation vortices. The separation vortices are broken into small eddies by the shearing action. Then small eddies merge while the others break with certain probability. Actually, the probability of eddy breakdown is much higher than that of eddy merging. Kinetic energy is transferred from eddies with relatively large scale to eddies with small scale and this transfer process continues until the rotational energy is dissipated by the viscous stress.

Both of the pressure field and velocity field are of homogeneous distribution on the upper semicircle of the cross section. Near the extrados, the pressure is relatively high due to the squeeze effect. Then the velocity of this region is relatively low. In addition, the pressure gradient adjacent to the extrados is lower than that adjacent to the intrados. Hence, the flow near the extrados is much more stable and this is the primary cause of the homogeneous flow field on the upper semicircle of the cross section.

5. Conclusion

The LES method combined with RANS method and experiments was applied to research the complicated flow field in a 90° elbow and the instantaneous turbulence information was obtained. The results were clarified to be reliable by comparing with that of RANS method and experiments. The conclusions obtained in this study are summarized as follows:

- (1) The instantaneous flow field in a 90° elbow is globally asymmetrical. The pattern and intensity of the Dean vortex and the small scale eddies change over time and induce the asymmetry of the flow field.
- (2) The counterrotating vortices and various scale eddies induced by shearing action exist in the region adjacent to the intrados.
- (3) The turbulent disturbance upstream and the interaction between the secondary flow and the flow separation are the dominant factors distorting the flow field.
- (4) The flow field on the upper semicircle of the cross sections is homogeneous due to the relatively lower velocity and pressure gradients of the fluid adjacent to the extrados.

Competing Interests

The authors declare that they have no competing interests.

Acknowledgments

This work is carried out in the frame of a current research project funded by the National Natural Science Foundation of China under Grant no. 51506114, the Specialized Research Fund for the Doctoral Program of Higher Education under Grant no. 20130002120015, and the Science Fund for Creative Research Groups of National Natural Science Foundation of China (Grant no. 51321002).

References

- [1] S. Y. Jiang, X. T. Yang, Z. W. Tang et al., "Experimental and numerical validation of a two-region-designed pebble bed reactor with dynamic core," *Nuclear Engineering and Design*, vol. 246, pp. 277–285, 2012.
- [2] R. Schulten, "Pebble bed HTRs," *Annals of Nuclear Energy*, vol. 5, no. 8–10, pp. 357–374, 1978.

- [3] A. C. Kadak and M. V. Berte, "Modularity in design of the MIT pebble bed reactor," in *Proceedings of the American Nuclear Society Meeting*, Reno, Nev, USA, November 2001.
- [4] A. Koster, H. D. Matzner, and D. R. Nicholsi, "PBMR design for the future," *Nuclear Engineering and Design*, vol. 222, no. 2-3, pp. 231-245, 2003.
- [5] Z. Y. Zhang, Z. X. Wu, Y. L. Sun, and F. Li, "Design aspects of the Chinese modular high-temperature gas-cooled reactor HTR-PM," *Nuclear Engineering and Design*, vol. 236, no. 5-6, pp. 485-490, 2006.
- [6] Z. Zhang, Z. Wu, D. Wang et al., "Current status and technical description of Chinese 2×250 MWth HTR-PM demonstration plant," *Nuclear Engineering and Design*, vol. 239, no. 7, pp. 1212-1219, 2009.
- [7] D. C. Taylor, M. B. McPherson, and E. B. Meier, "Elbow meter performance [with Discussion]," *Journal of the American Water Works Association*, vol. 46, no. 11, pp. 1087-1095, 1954.
- [8] K. Rup and L. Malinowski, "Fluid flow identification on base of the pressure difference measured on the secant of a pipe elbow," *Forschung im Ingenieurwesen*, vol. 70, no. 4, pp. 199-206, 2005.
- [9] L. Malinowski and K. Rup, "Measurement of the fluid flow rate with use of an elbow with oval cross section," *Flow Measurement and Instrumentation*, vol. 19, no. 6, pp. 358-363, 2008.
- [10] S. A. Berger, L. Talbot, and L. S. Yao, "Flow in curved pipes," *Annual Review of Fluid Mechanics*, vol. 15, pp. 461-512, 1983.
- [11] H. Ito, "Flow in curved pipes," *JSME International Journal*, vol. 30, no. 262, pp. 543-552, 1987.
- [12] R. J. S. Pigott, "Pressure losses in tubing, pipe and fittings," *Transactions of the ASME*, vol. 72, pp. 679-688, 1950.
- [13] H. Kirchbach, *Loss of Energy in Miter Bends*, Transactions of the Munich Hydraulic Institute, American Society of Mechanical Engineers, 1935.
- [14] W. Schubart, "Energy loss in smooth and rough surfaced bends and curves in pipe-lines," *Transactions of the Hydraulic Institute of the Munich Technical University*, vol. 3, pp. 81-99, 1935.
- [15] M. M. Enayet, M. M. Gibson, A. M. K. P. Taylor, and M. Yiannekis, "Laser-Doppler measurements of laminar and turbulent flow in a pipe bend," *International Journal of Heat and Fluid Flow*, vol. 3, no. 4, pp. 213-219, 1982.
- [16] K. Sudo, M. Sumida, and H. Hibara, "Experimental investigation on turbulent flow in a circular-sectioned 90-degree bend," *Experiments in Fluids*, vol. 25, no. 1, pp. 42-49, 1998.
- [17] Y. Eguchi, T. Murakami, M. Tanaka, and H. Yamano, "A finite element les for high-Re flow in a short-elbow pipe with undisturbed inlet velocity," *Nuclear Engineering and Design*, vol. 241, no. 11, pp. 4368-4378, 2011.
- [18] F. Rütten, M. Meinke, and W. Schröder, "Large-eddy simulation of 90° pipe bend flows," *Journal of Turbulence*, vol. 2, 2001.
- [19] F. Rütten, W. Schröder, and M. Meinke, "Large-eddy simulation of low frequency oscillations of the Dean vortices in turbulent pipe bend flows," *Physics of Fluids*, vol. 17, no. 3, Article ID 035107, 2005.
- [20] M. J. Tunstall and J. K. Harvey, "On the effect of a sharp bend in a fully developed turbulent pipe-flow," *Journal of Fluid Mechanics*, vol. 34, no. 3, pp. 595-608, 1968.
- [21] A. Ono, N. Kimura, H. Kamide, and A. Tobita, "Influence of elbow curvature on flow structure at elbow outlet under high Reynolds number condition," *Nuclear Engineering and Design*, vol. 241, no. 11, pp. 4409-4419, 2011.
- [22] Y. Eguchi, T. Murakami, M. Tanaka, and H. Yamano, "A finite element les for high-Re flow in a short-elbow pipe with undisturbed inlet velocity," *Nuclear Engineering & Design*, vol. 241, no. 11, pp. 4368-4378, 2011.
- [23] U. Piomelli and E. Balaras, "Wall-layer models for large-eddy simulations," *Annual Review of Fluid Mechanics*, vol. 34, pp. 349-374, 2002.

Research Article

A Calculation Method for the Sloshing Impact Pressure Imposed on the Roof of a Passive Water Storage Tank of AP1000

Daogang Lu,^{1,2} Xiaojia Zeng,^{1,2} Junjie Dang,³ and Yu Liu^{1,2}

¹School of Nuclear Science and Engineering, North China Electric Power University, Beijing 102206, China

²Beijing Key Laboratory of Passive Safety Technology for Nuclear Energy, North China Electric Power University, Beijing 102206, China

³China Nuclear Power Engineering Co., Ltd., Beijing 100840, China

Correspondence should be addressed to Xiaojia Zeng; 453672704@qq.com

Received 18 January 2016; Revised 6 April 2016; Accepted 19 May 2016

Academic Editor: Iztok Tiselj

Copyright © 2016 Daogang Lu et al. This is an open access article distributed under the Creative Commons Attribution License, which permits unrestricted use, distribution, and reproduction in any medium, provided the original work is properly cited.

There is a large water storage tank installed at the top of containment of AP1000, which can supply the passive cooling. In the extreme condition, sloshing of the free surface in the tank may impact on the roof under long-period earthquake. For the safety assessment of structure, it is necessary to calculate the impact pressure caused by water sloshing. Since the behavior of sloshing impacted on the roof is involved into a strong nonlinear phenomenon, it is a little difficult to calculate such pressure by theoretical or numerical method currently. But it is applicable to calculate the height of sloshing in a tank without roof. In the present paper, a simplified method was proposed to calculate the impact pressure using the sloshing wave height, in which we first marked the position of the height of roof, then produced sloshing in the tank without roof and recorded the maximum wave height, and finally regarded approximately the difference between maximum wave height and roof height as the impact pressure head. We also designed an experiment to verify this method. The experimental result showed that this method overpredicted the impact pressure with a certain error of no more than 35%. By the experiment, we conclude that this method is conservative and applicable for the engineering design.

1. Introduction

As the ultimate heat sink of AP1000 reactor, passive cooling system (PCS) is the key equipment to ensure the safety of nuclear power plant. The large water storage tank, installed at the top of the containment of AP1000, can supply plenty of water for the passive cooling. In the extreme condition, sloshing of the free surface in the tank may impact on the roof and jeopardize structural integrity under long-period earthquake. For the safety assessment of structure, it is necessary to calculate the impact pressure caused by water sloshing.

Since the behavior of sloshing impacted on the roof is involved into a strongly nonlinear phenomenon, calculations of the impact pressure with theoretical or numerical method currently are of difficulties. Ibrahim [1] focused on a 2D tank with simple geometry to solve the linear sloshing problems using analytical methods. A numerical model using finite element technique was presented by Pal et al. [2] to study

the linear behavior of cylindrical tanks. Choun and Yun [3] used the velocity potential and the linear water wave theory to decompose the surface wave into multiple forms. There are some complex methods to solve the nonlinear sloshing problems. Li et al. [4] used an improved material point method (MPM) to predict the liquid impact force by a contact algorithm. Liquid sloshing experiments in a partially watered square tank were proposed to validate the results of simulation. Eswaran et al. [5] proposed a numerical method based on volume of fluid (VOF) techniques with arbitrary-Lagrangian-Eulerian (ALE) formulation to analyze baffled and unbaffled tanks with a nonlinear sloshing behavior. However, these researches are usually valid for simple cases with linear or weakly nonlinear liquid sloshing dynamics.

But it is applicable to calculate the height of sloshing in a tank without roof. Fujita et al. [6] utilized the velocity potential theory to analyze the liquid sloshing in the annular region of more intricate coaxial circular cylinders. Formulas

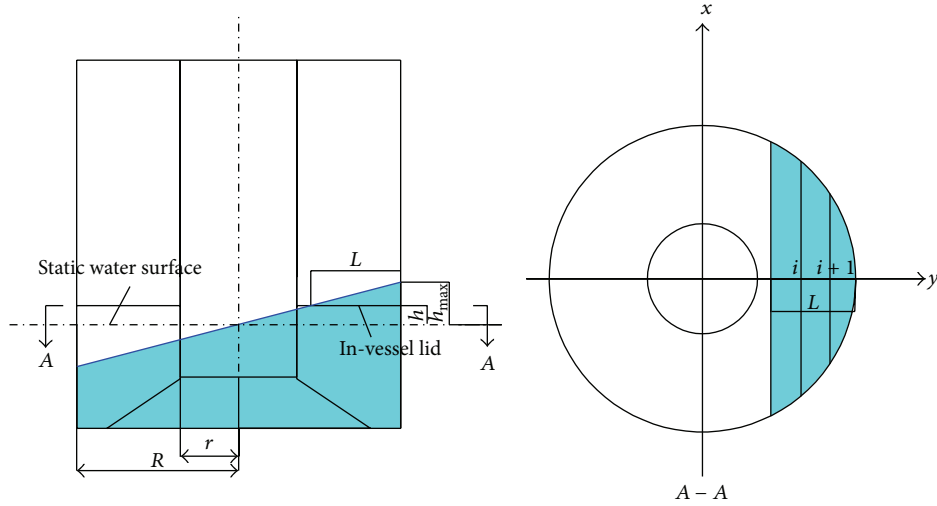


FIGURE 1: Schematic of sloshing.

about the maximum wave height (η_{\max}) at shell wall and the maximum pressure (p_{\max}) at the free surface were obtained. More interestingly, the correlation between maximum wave height and maximum pressure was $p_{\max} = \rho g \eta_{\max}$ from equation (34) in their research. Virella et al. [7] used the finite element package ABAQUS to investigate the free surface wave amplitude and pressure distribution of tank wall by both linear wave theory and nonlinear wave theory models. Nayak and Biswal [8] used the Galerkin-weighted-residual based finite element method (FEM) to solve Laplace equation with nonlinear boundary conditions. The wave height of nonlinear sloshing was verified to be accurate.

Besides, the impact pressure is an important parameter in the assessment of safety of engineering design. Researchers had conducted large-scale experiments to investigate impact pressure [9–12].

As is mentioned above, the available studies mostly focused on the sloshing characteristics of rectangular tanks with simple geometry. However, considering the special structure of PCCWST, which is a coaxial circular cylinder tank with an inclined bottom, it is difficult in obtaining analytical expressions for the prediction of the natural modes and the liquid motion. Moreover, numerical and analytical methods to precisely describe the sloshing impact pressure are complicated because of the significant nonlinearity phenomena. In the present paper, a simplified method was proposed to calculate the impact pressure using the sloshing wave height. Moreover, an experiment was designed to verify this method.

2. Calculation Method

Sloshing of the water surface in the tank may impact on the roof under long-period earthquake and the prediction of the impact pressure is necessary. Due to the apparent nonlinear behavior caused by complicated sloshing phenomena, a simplified method was proposed to calculate the impact pressure using the sloshing wave height, in which we first marked

the position of the height of roof, the solid wide line showed in Figure 1, then produced sloshing in the tank without roof and recorded the maximum wave height which can be shown as the oblique line in Figure 1, and finally regarded approximately the difference between maximum wave height and roof height as the impact pressure head. In this way, the impact pressure can be calculated by the following equation:

$$P = \rho g (h_{\max} - h), \quad (1)$$

where P is the maximum impact pressure, ρ is the density of water, g is the acceleration due to gravity, h_{\max} is the maximum wave height, and h is the distance between the static water surface and the roof.

Besides, the impact force of water in a tank at any time is given by the following equation:

$$F_w = \iint_{s_1}^{s_2} P ds, \quad (2)$$

where F_w is impact force, P is the impact pressure, and s_1 , s_2 , respectively, mean the lower and upper boundary of tank roof.

By utilizing the maximum sloshing wave height, the maximum impact pressure, which appeared near the outer wall, can be calculated by (1).

The impact area is divided into n parts and the impact pressures in each part can be obtained by linear interpolation. The i th pressure is given by the following equation:

$$p_i = \frac{i}{n} \rho g (h_{\max} - h). \quad (3)$$

According to Figure 1, L , which is related to the impact area, can be calculated by

$$\frac{L}{R} = \frac{h_{\max} - h}{h_{\max}}. \quad (4)$$

TABLE 1: Scaling factors for sloshing experiments.

Parameter	Scaling ratio
Length: L [m]	C_l
Gravity: g [m/s^2]	1
Velocity: V [m/s]	$C_l^{1/2}$
Frequency: f [Hz]	$C_l^{-1/2}$
Time: t [s]	$C_l^{1/2}$
Kinematic viscosity: ν [m^2/s]	$C_l^{3/2}$
Pressure: P [Pa]	$C_p C_l$
Wave height: H [m]	C_l

The total impact force can be written as

$$F_t = \sum_{i=0}^{n-1} \int_{-\sqrt{R^2-y^2}}^{\sqrt{R^2-y^2}} dx \int_{R-L+i(L/n)}^{R-L+(i+1)(L/n)} \frac{p_i + p_{i+1}}{2} dy \quad (5)$$

$$i = 0, 1, 2, 3, \dots, n-1.$$

Substituting (3) and (4) to (5), we can get the total impact force.

3. Experiment

In order to verify the calculation method, an experiment was designed.

3.1. Scaling Model. Since the passive storage tank of AP1000 is large, experiment with the large size of tank is difficult. In order to keep the similar properties of fluid, a scaling model is proposed. For the case of the present experiment, some main governing dimensionless numbers that should be respected are as follows [6, 13].

Froude number: $Fr = V^2/gL$; Reynolds number: $Re = VL/\nu$; Strouhal number: $St = fL/V$; Euler number: $Eu = P/\rho V^2$; Bond number: $Bo = \rho g L^2/\sigma$.

With the analysis, the Froude number, Strouhal number, Euler number, and Bond number are respected and the Re number is relaxed when ignoring viscosity effects. The scaling factors for the different parameters in sloshing experiments are summarized in Table 1 and these expressions are called the modified linear scaling method.

3.2. Experimental Equipment. According to the similarity criteria, an experimental model (Figure 2) of PCCWST was built with the scale of 1:40. The experimental tank was mainly cylindrical (0.122 m internal radius) with an inclined bottom and the vessel was made of acrylic sheet to observe the sloshing phenomena clearly. The tank was considered to be rigid due to the 15 mm thickness of outer wall. This assumption was made to simplify the study of sloshing. In order to measure the maximum sloshing wave height, the length scaling for the height of the tank was 3:40. A summary of the main sizes of experimental tank is presented in Figure 3.

The internal structures, showed as the red parts in Figure 3, were added suspended from the top cover, which was fixed on the outer structure. Such internal structures contained a supporting configuration and an in-vessel circle roof

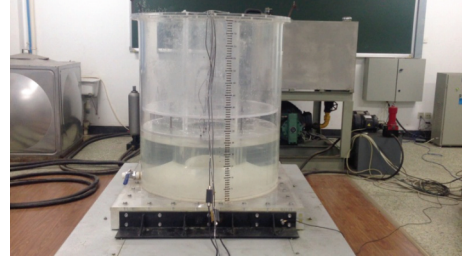


FIGURE 2: Experimental setup.

mounted on the supporting configuration by 4 connecting rods with knurled caps. The whole experimental tank was glued to a square shell which was screwed in 28 threaded holes on the shaking table.

The experimental setup included a computer, a laser displacement sensor, 3 pressure sensors, an acceleration sensor, a data acquisition tool, a set of commercial acquisition software COINV DASP, and some wires. The layouts and numbers of sensors are illustrated in Figure 3.

3.3. Experimental Procedure and Results. Tabulating in Table 2, a total of 6 experiment cases involving 4 different filling depths were carried out on the experimental setup with two configurations, first without internal components (a supporting configuration and an in-vessel roof) and then with internal components. For each case, sloshing experiments under multiple excitation amplitudes were carried out and several kinds of transient sloshing responses like sloshing wave height and slosh-induced impact pressure were recorded by data acquisition system. Measurements of the wave height are presented in Section 3.3.2, in cases without internal components. Impact pressure of sloshing is discussed in Section 3.3.3 in cases with internals.

3.3.1. Natural Frequency of Sloshing in First Mode. Liquid motion inside a tank in periodic movement is dominated by the liquid filling ratio, the amplitude and frequency of the tank motion, and the geometry of the tank. Considering the complex geometry of the experimental tank, the fundamental natural frequency of liquid was measured through sweep frequency response analysis (SFRA) experiment. The tank was partially filled with water, which was mixed with gouache paint and covered by pearl cotton on the surface. It was aimed to make the laser displacement sensor work normally by detecting object with surface that exhibited a diffuse reflection. From the research of Lu et al. [14], the influence of water level on natural frequency of sloshing water was quite small. Hence, the subtle variations of natural frequency with different filling depths can be ignored. The tank was filled up to a water level of 217 mm, which was based on the length scale, for the measuring of liquid frequency. For the purpose of looking in detail at the resonance frequency of liquid, a logarithmic sweep with a range of 0.1~20 Hz was adopted. In addition, there are two types of control mode for driving the shaking table: Acceleration Control (AC) and Displacement Control (DC). At low frequency, about 0.1~4 Hz, AC is used

TABLE 2: Experiment sequences.

Case number	Filling depth H [mm]	Distance between static water surface and in-vessel roof h [mm]	Excitation amplitude A [mm]
1*	217	43	12, 24, 36
2	177	83	12, 24, 36
3	197	63	12, 24, 36
4	237	23	12, 24, 36

*: H and h are based on the length scale.

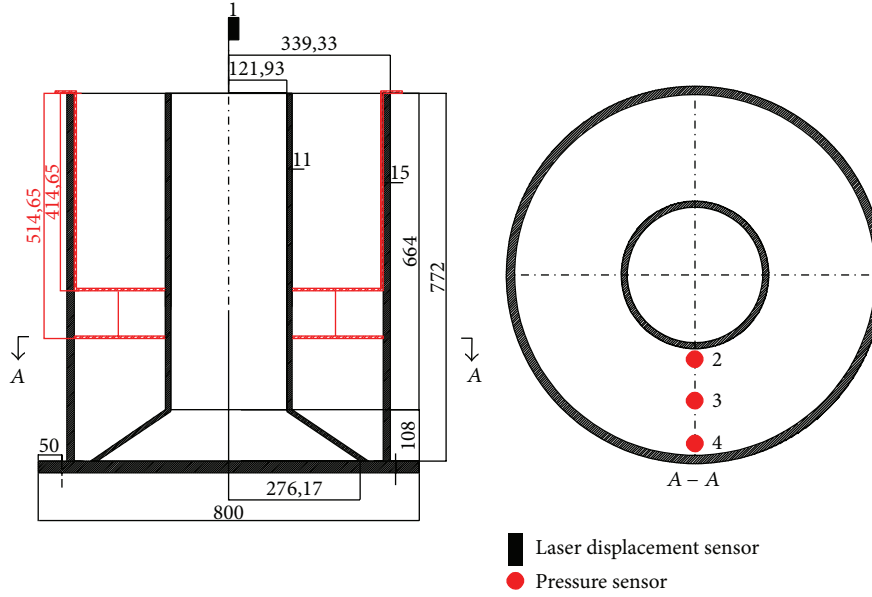


FIGURE 3: Sensor layout.

and the displacement was controlled at the value of 2.0 mm, since the displacement sensor achieved higher accuracy than acceleration sensor at low frequency range. However, DC is invoked in high frequency of 4~20 Hz and the acceleration was set with 0.650 m/s^2 . The time history of sloshing displacement was transformed into frequency spectrum by a fast Fourier transform (FFT). By this analysis, the fundamental natural frequency of the liquid was evaluated to be 0.75 Hz.

For an annular region formed by coaxial circular cylinder tank in periodic motion, the resonant frequencies of the liquid can be calculated from the linear potential theory as [6, 13]

$$\omega_{mn}^2 = \frac{g}{a} \xi_{mn} \tanh\left(\xi_{mn} \frac{H}{a}\right) \quad (6)$$

$$m = 0, 1, 2, \dots, \infty, \quad n = 1, 2, 3, \dots, \infty,$$

where g is the gravitational acceleration, a is the outer radius of the tank, ξ_{mn} are the positive roots related to the ratios of inner radius to outer radius of the tank, and H is the still filling depth.

The calculating fundamental natural frequency from (6) is 0.887 Hz, a little larger than the experimental result. It can be explained by the inclined bottom configuration of the tank.

3.3.2. Sloshing without the Roof. Due to the fact that the periods of sloshing water ($1/f = 1/0.75 = 1.33 \text{ s}$) were far more longer than the site predominant period (0.34 s), the resonant three-cycle sine wave (RTCS) was assumed to be the input excitation according to the HAF0102 of nuclear safety guide in China, which is also a widely used evaluation method of seismic response in Japan. The load function can be written as $X = A \sin(2\pi ft)$, where X is the displacement of shaking table, A is the amplitude of the sine wave, f is the water natural frequency, and t is the time which lasts for three periods of sine waves. In our experiments, the frequency of RTCS was set as 0.75 Hz. When the frequency of excitation closed to the natural frequency, the liquid inside the experimental tank can exhibit strong oscillations, thus exerting a greater extent of sloshing and violent impact loads on the tank.

The experimental setup without internals was carried out for the experiment of seismic response about sloshing wave height. The sloshing wave height was measured through laser displacement sensor which was installed at point 1 near the outer tank wall which is showed in Figure 3. The acceleration transducer was installed at the bottom of the tank, in order to monitor the initial and final points of RTCS. Figure 4 reveals the vertical displacement of the wave in case 1 with 24 mm amplitude. It can be seen that the crest was almost 2 times

TABLE 3: The maximum wave height.

Amplitude [mm]	Case 1	Case 2	Case 3	Case 4
12	79.191	65.272	67.103	98.9172
24	227.355	163.953	190.414	264.142
36	316.327	217.348	255.602	355.023

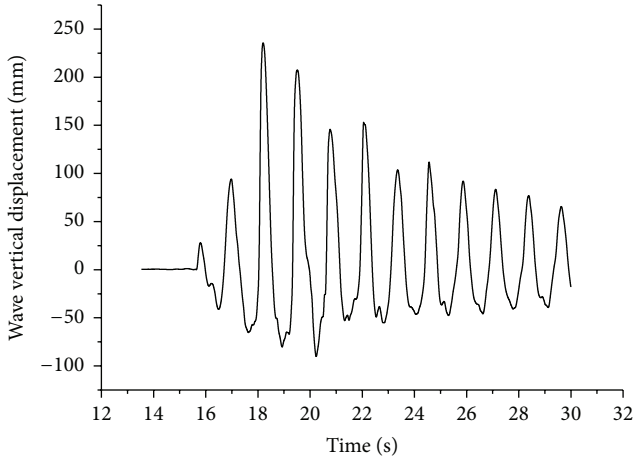


FIGURE 4: The vertical displacement time history of sloshing wave of case 1 with 24 mm amplitude.

size of the trough, which embodied an apparent feature of nonlinearity. Table 3 lists the maximum wave heights of case 1 to case 4. Moreover, through the analysis of these data, for each case, the maximum wave heights increased as the excitation amplitudes grew and the increasing tendency gradually reduced, which was also a nonlinear behavior.

3.3.3. Sloshing with Roof. At the second part of the experiment, experiments with internals were carried out to measure the impact pressure of in-vessel roof. CYY8 dynamic pressure sensors with high frequency response were installed at measuring points 2, 3, and 4 on the roof, as showed in Figure 3, to present the radial pressure distribution.

Pressure variations were measured by dynamic piezoresistive pressure transducers in cases 1 to 4. Figure 5 illustrates the impact pressures time history results in case 1 of measuring point 4 with 24 mm amplitude. According to the curve, the maximum impact pressure appeared when it came to the third wave of RTCs and then 2 small peaks came after it. These two small peaks can be explained by the inertia effect of water, which made water impact the inner roof despite the end of excitation. In addition, the gap between in-vessel roof and the tank wall would lead to a small portion of water splashing upward to the top surface of cap. Therefore, some negative values appeared intermittently in the measuring data showed in Figure 5.

As is shown in Figure 6, impact pressure distributions along the radial direction are presented in cases with different RTCs and the same filling depth, 217 mm. The impact pressure of point 2 was the minimum and the impact pressure of point 4 was the maximum, which showed that the impact pressure increases from inner wall to outer wall.

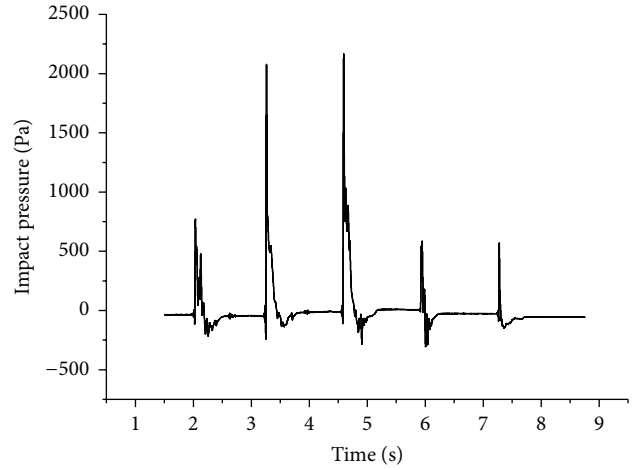


FIGURE 5: Time history of impact pressure about case 1 of point 4 with 24 mm amplitude.

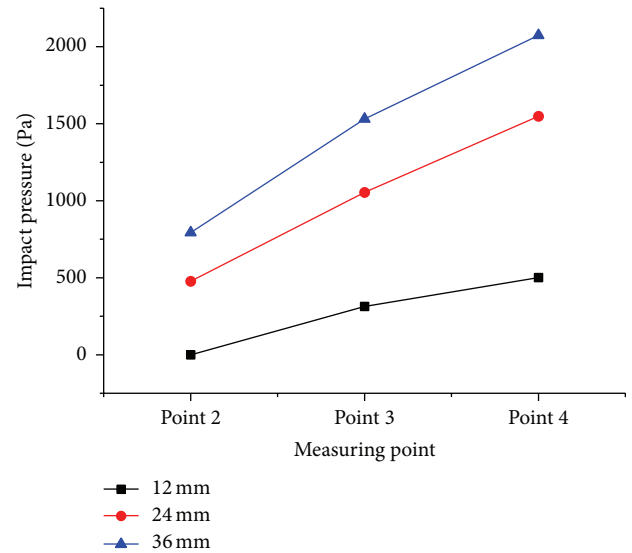


FIGURE 6: The distribution of impact pressure of case 1 with 24 mm amplitude.

During the operational process of experiments, there were some errors in experimental data owing to erroneous human input and the accuracy of measuring instruments to a certain extent. The use of laser displacement sensor, pressure sensors, and the indigenous vibration of shaking table caused significant errors in measurements. Besides, there also existed electromagnetic interferences during the operational process of shaking table, which adversely affected the accuracy of sensors especially pressure sensors, also contributed to the errors' list.

By computing the area integral of pressure, the experimental force data can be derived from the measuring pressure data with some conservative assumptions.

In our research, as illustrated in Figure 7, the area from inner wall to outer wall along y axis is divided into 3 parts and the pressure of each part is assumed to be the measuring

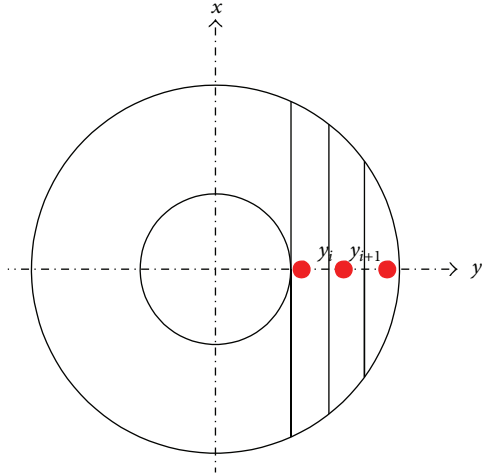


FIGURE 7: Schematic of area dividing.

value of the sensor which is installed at the corresponding part. Therefore, the impact force in each part can be written as in (7). The total impact force is the sum of that in each part which is showed in (8). Consider the following:

$$F_i = \int_{-\sqrt{R^2-y^2}}^{\sqrt{R^2-y^2}} dx \int_{y_i}^{y_{i+1}} p_i dy, \quad (7)$$

$$F_t = \sum_{i=1}^n F_i \quad i = 1, 2, 3, \quad (8)$$

where F_i and p_i are the impact force and impact pressure in each part, R is the outer radius of cylinder tank, and F_t is the total impact force.

In our cases, the total impact forces of different conditions are listed in Table 4.

4. Analysis of Experimental Results

In Section 2, we proposed a simplified method to estimate the impact pressure. So we list the results of simplified method and measured data. We used the calculated impact pressure (CIP) indirectly to represent the results of simplified method. The measured data were called the measured impact pressure (MIP) directly. The comparison between calculated pressure and measured pressure is listed in Table 5.

According to Table 5, CIP are lower than MIP under small amplitudes of RTCS. A possible reason is the influence of air motion. In our experiment, the water tank cannot be thoroughly sealed. Therefore, air in the ring cavity can move with the vigorous sloshing of water. Air motion is the primary influential factor under low level of excitation. However, it is considered that small excitation has really subtle effect in engineering practice. As for the higher excitation level, CIP are larger than MIP under medium and high level of excitations. With a certain error of no more than 35%, this method of impact pressure calculation is considered to be overpredictive. Therefore, similar to the results of Lu's [15] research, it

TABLE 4: Total impact force from measuring data.

Case no.	Filling depth [mm]	Amplitude [mm]	Impact force [N]
1	217 mm	12	11.31001
		24	60.37129
		36	91.28681
2	177 mm	12	4.370317
		24	25.62775
		36	41.8155
3	197 mm	12	7.423492
		24	36.49382
		36	56.19478
4	237 mm	12	23.1682
		24	84.23761
		36	117.9033

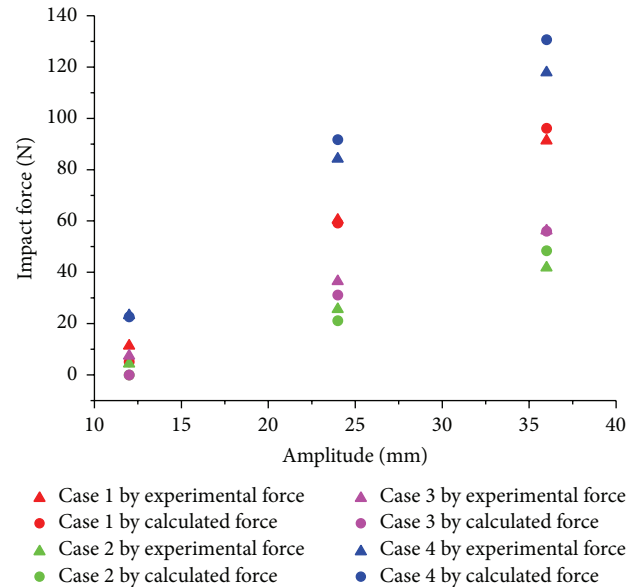


FIGURE 8: Comparison of calculated force and experimental force.

can be concluded that the calculation method is reasonable and relatively conservative.

According to the simplified calculation equation for impact force proposed in Section 2, we obtained the impact force of simplified method which was called calculated force here. Showed in Section 3.3.3, the experimental force data was called experimental force here. Figure 8 compares the calculated force and experimental force. The calculated force is lower than, though generally coinciding with, the experimental force in smaller wave height cases. However, calculated force becomes close to the experimental force and then exceeds it due to the increase of maximum sloshing wave height.

By the comparison of calculated results and experimental results, some future works are left. First, there should be some holes on the in-vessel roof to reduce the influence of air motion during experimental procedure. Second, longer

TABLE 5: The comparison between calculated pressure and measured pressure.

Case no.	Amplitude [mm]	Measured pressure (MIP) [Pa]	Calculated pressure (CIP) [Pa]	Error (%)
1	12	500.62	354.6718	-29.1536
	24	1549.30	1806.679	16.6126
	36	2074.05	2678.605	29.14851
2	12	263.27	0	-100
	24	913.30	793.3394	-13.1349
	36	1243.44	1316.61	5.884514
3	12	397.514	40.209	-89.8856
	24	1221.34	1248.657	2.236658
	36	1579.48	1887.5	19.50133
4	12	757.21	743.9886	-1.74607
	24	1753.86	2363.192	34.74232
	36	2445.99	3253.825	33.02691

duration time experiments with more pressure sensors and displacement sensors are needed to investigate the impact pressure distribution and computation of impact force.

5. Conclusions

- (1) In order to estimate the impact pressure imposed on the roof of water storage tank of AP1000, we proposed a simplified method, which regarded approximately the difference between maximum wave height and roof height as the impact pressure head.
- (2) In order to verify the above method, we built a scaled experimental facility.
- (3) Using the experimental facility, we measured the maximum sloshing wave height in the case of not having roof and the impact pressure in the case of having roof.
- (4) By the above experiment, the simplified method was considered to be conservative with a certain error of no more than 35%.

Competing Interests

The authors declare that they have no competing interests.

Acknowledgments

The project was sponsored by National Science and Technology Major Project of the Ministry of Science and Technology of China (2015ZX06004002-003).

References

- [1] R. A. Ibrahim, *Liquid Sloshing Dynamics: Theory and Applications*, Cambridge University Press, New York, NY, USA, 2005.
- [2] N. C. Pal, P. K. Sinha, and S. K. Bhattacharyya, "Finite element coupled slosh analysis of rectangular liquid filled laminated composite tanks," *Journal of Reinforced Plastics and Composites*, vol. 18, no. 15, pp. 1375-1407, 1999.
- [3] Y.-S. Choun and C.-B. Yun, "Sloshing analysis of rectangular tanks with a submerged structure by using small-amplitude water wave theory," *Earthquake Engineering and Structural Dynamics*, vol. 28, no. 7, pp. 763-783, 1999.
- [4] J. G. Li, Y. Hamamoto, Y. Liu, and X. Zhang, "Sloshing impact simulation with material point method and its experimental validations," *Computers & Fluids*, vol. 103, pp. 86-99, 2014.
- [5] M. Eswaran, U. K. Saha, and D. Maity, "Effect of baffles on a partially filled cubic tank: numerical simulation and experimental validation," *Computers & Structures*, vol. 87, no. 3-4, pp. 198-205, 2009.
- [6] K. Fujita, T. Ito, and K. Okada, "Seismic response of liquid sloshing in the annular region formed by coaxial circular cylinders," *Engineering Computations*, vol. 2, no. 4, pp. 299-306, 1985.
- [7] J. C. Virella, C. A. Prato, and L. A. Godoy, "Linear and nonlinear 2D finite element analysis of sloshing modes and pressures in rectangular tanks subject to horizontal harmonic motions," *Journal of Sound and Vibration*, vol. 312, no. 3, pp. 442-460, 2008.
- [8] S. K. Nayak and K. C. Biswal, "Nonlinear seismic response of a partially-filled rectangular liquid tank with a submerged block," *Journal of Sound and Vibration*, vol. 368, pp. 148-173, 2016.
- [9] H. Akyildiz and E. Ünal, "Experimental investigation of pressure distribution on a rectangular tank due to the liquid sloshing," *Ocean Engineering*, vol. 32, no. 11-12, pp. 1503-1516, 2005.
- [10] Y. K. Song, K.-A. Chang, Y. Ryu, and S. H. Kwon, "Experimental study on flow kinematics and impact pressure in liquid sloshing," *Experiments in Fluids*, vol. 54, no. 9, article 1592, 2013.
- [11] A. Souto-Iglesias, G. Bulian, and E. Botia-Vera, "A set of canonical problems in sloshing. Part 2: influence of tank width on impact pressure statistics in regular forced angular motion," *Ocean Engineering*, vol. 105, pp. 136-159, 2015.
- [12] F. Pistani and K. Thiagarajan, "Experimental measurements and data analysis of the impact pressures in a sloshing experiment," *Ocean Engineering*, vol. 52, pp. 60-74, 2012.
- [13] H. N. Abramson, "The dynamic behavior of liquids in moving containers, with applications to space vehicle technology," Tech. Rep. NASA-SP-106, NASA, Washington, DC, USA, 1966.

- [14] D. Lu, Y. Liu, and X. Zeng, "Experimental and numerical study of dynamic response of elevated water tank of AP1000 PCCWST considering FSI effect," *Annals of Nuclear Energy*, vol. 81, pp. 73–83, 2015.
- [15] D. Lu, "Sloshing response of the free surface in the main vessel of CEFR excited by 3 sine waves," *Chinese Journal of Nuclear Science and Engineering*, vol. 23, pp. 306–310, 2003.

Research Article

Assessment of Prediction Capabilities of COCOSYS and CFX Code for Simplified Containment

Jia Zhu,¹ Xiaohui Zhang,¹ and Xu Cheng²

¹School of Energy, Soochow University, Suzhou 215000, China

²Karlsruhe Institute of Technology (KIT), 76131 Karlsruhe, Germany

Correspondence should be addressed to Xiaohui Zhang; xhzhang@suda.edu.cn

Received 4 February 2016; Accepted 8 May 2016

Academic Editor: Keith E. Holbert

Copyright © 2016 Jia Zhu et al. This is an open access article distributed under the Creative Commons Attribution License, which permits unrestricted use, distribution, and reproduction in any medium, provided the original work is properly cited.

The acceptable accuracy for simulation of severe accident scenarios in containments of nuclear power plants is required to investigate the consequences of severe accidents and effectiveness of potential counter measures. For this purpose, the actual capability of CFX tool and COCOSYS code is assessed in prototypical geometries for simplified physical process-plume (due to a heat source) under adiabatic and convection boundary condition, respectively. Results of the comparison under adiabatic boundary condition show that good agreement is obtained among the analytical solution, COCOSYS prediction, and CFX prediction for zone temperature. The general trend of the temperature distribution along the vertical direction predicted by COCOSYS agrees with the CFX prediction except in dome, and this phenomenon is predicted well by CFX and failed to be reproduced by COCOSYS. Both COCOSYS and CFX indicate that there is no temperature stratification inside dome. CFX prediction shows that temperature stratification area occurs beneath the dome and away from the heat source. Temperature stratification area under adiabatic boundary condition is bigger than that under convection boundary condition. The results indicate that the average temperature inside containment predicted with COCOSYS model is overestimated under adiabatic boundary condition, while it is underestimated under convection boundary condition compared to CFX prediction.

1. Introduction

The containment phenomenological aspects during an accident have been studied extensively during the last 40 years for light water reactors [1–4]. Nevertheless, the Fukushima accident has driven the attention of the regulatory bodies and the industry to the assessment of the detailed thermal-hydraulic containment simulation under severe accident conditions [5].

Considerable international efforts were dedicated to better understand related phenomena by performing experiments and analytical assessments of their results. Since it is not possible to perform containment thermal-hydraulics experiments in the existing nuclear power plants due to safety concerns, experiments are performed in special facilities, which imitate containment or their parts [6, 7]. However, such devices are usually smaller in size and have simpler geometry than prototypical containment. Therefore, in order to study processes on the containment scale, numerical experiments are also performed using computer codes. Codes

are also used for simulation of experiments, in order to better understand experimental results, and to assess code capability to simulate occurring processes.

Two main kinds of codes/approaches are used for simulation of containment thermal-hydraulics, that is, lumped-parameter approach with highly simplified 0D models and 3D CFD (Computational Fluid Dynamics) approach.

The program COCOSYS, a lumped-parameter code, is being developed by the Gesellschaft für Anlagen- und Reaktorsicherheit (GRS) gGmbH, Germany, for the simulation of all relevant processes and plant states during severe accidents in containment of light water reactors. And this code is widely used in nuclear engineering [8, 9]. The characteristic feature of lumped-parameter approach is that mass and energy are transferred between control volumes by junctions, according to momentum equation solution for each junction.

The CFX code is a general purpose CFD tool developed by ANSYS Inc. The code solves the conservation equations for mass, momentum, and energy together with their initial

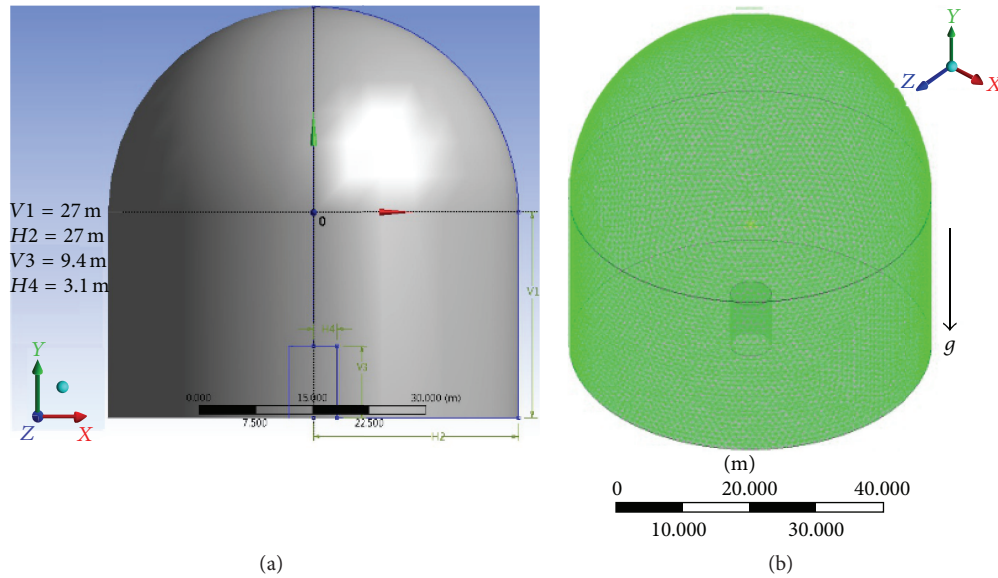


FIGURE 1: Geometry (a) and mesh (b) for CFD simulation.

and boundary conditions. The discretization of the equations in the CFX code is based on a conservative finite-volume method.

Considerable research has been devoted to the study of the associated phenomena predicted by lumped-parameter code and field code; the development of various computer codes to analyze these severe accidents phenomena is summarized in the review [10].

Nevertheless containment thermal-hydraulics prediction remains an open question. One outcome of the ISP-47 (TOSQAN, MISTRA, and THAI) [11] activity was the recommendation to elaborate generic containment including all important components. In the frame of the European Network of Excellence SARNET2 (Severe Accident Research Network) such generic containment nodalisation was developed, based on an existing COCOSYS model of a German pressurized water reactor (PWR) with 1300 MWe, provided by GRS [12]. It is used to compare and to assess analyses being performed with different lumped-parameter (LP) codes and models. Moreover, it can serve as a basis for testing new model developments on a commonly available and accepted basis on plant scale in future.

In present work, a simplified enclosure based on generic containment is adapted in prototypical geometries for comparing different simulation results with separate effects scenario “thermal plume” to illustrate the prediction capacity of COCOSYS and ANSYS CFX.

2. Assessment of COCOSYS and CFX Prediction Results

Irrespective of the nature of the accident, heat and mass transfer play a major role in these accidents. Quite often it is a complex phenomenon involving forced and natural convection heat transfer, metal-water reaction, nuclear heat

generation, melting, condensation, diffusive and convective mass transfer, nucleate and film boiling, porous medium, combustion, and detonation.

The analyses presented here aimed at investigating the accuracy of COCOSYS code compared to the CFD codes to provide an evaluation of the applicability to the large-scale, transient problems. To this aim, the assessment must use separate-effect simulation, so we focus on a plume (due to a heat source) process in the present work; on the other hand, because of the thin shell and cylinder structure in CFX model, measures of smaller structure thickness with higher structure conductivity, lower density, and heat capacity are taken in COCOSYS model to eliminate the transient process impact of the structure, so that COCOSYS model and CFX model are comparable.

2.1. Computational Modeling. Figure 1 shows the geometry of the CFD simulation physical modeling. The main characteristics of the simplified containment are the following: a volume of about 102724 m^3 , including a cylinder with radius of 27 m and a height of 27 m, and a hemisphere with radius of 27 m. R-CAVITY (radius $H4 = 3.1 \text{ m}$; height $V3 = 9.4 \text{ m}$) is the system heat source with constant value 3000 kW; the rest of space is full of air. The turbulence $k-\epsilon$ model and nonsteady method were used in the calculations.

After grid independent test (coarse, intermediate, and fine mesh), mesh containing tetra element (element size 1.0 m) is adopted; it is simulated in CFX with a 3D Cartesian geometry model using 90,142 computational elements with 1234,062 nodes. Figure 1 shows a 3D view of the domain mesh.

The input data and nodalisation of the generic containment have been created on the basis of benchmark run-2 COCOSYS code for German PWR simulation [12]. Figure 2 shows the COCOSYS model; finer vertical nodalisation is built with 46 zones.

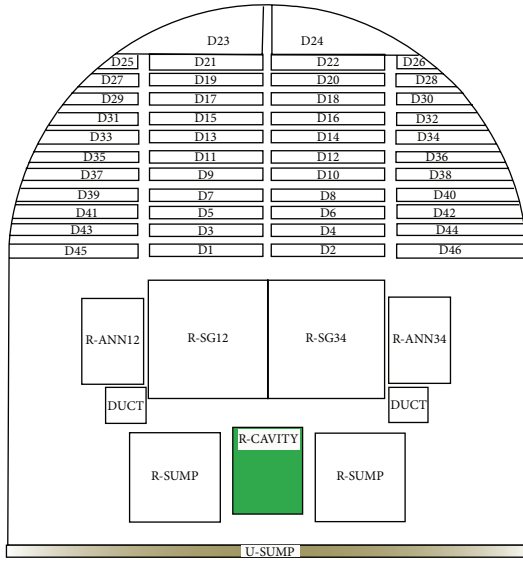


FIGURE 2: COCOSYS model.

An overview of the general initial condition and boundary condition is listed as follows.

(1) Adiabatic case:

- Initial condition: air at 1 bar pressure and 20°C temperature.
- R-CAVITY volumetric heat generation: 3000 kW.
- Boundary condition: adiabatic enclosure.

(2) Convection case:

- Initial condition: air at 1 bar pressure and 20°C temperature.
- R-CAVITY volumetric heat generation: 3000 kW.
- USUMP boundary condition: adiabatic condition.
- More specific information on the convection condition which follows in Section 2.3.

2.2. *Adiabatic Case.* Direct comparison of the zone temperature in COCOSYS and discrete point temperature is difficult due to some differences between COCOSYS and CFX; an alternative approach is to take a weighted average of CFX discrete points corresponding to COCOSYS area temperature.

The results are compared in curve charts for transient evolution process in Figure 3 at R-SG12 zone.

The *x*-axis in the graph is the time, *y*-axis represents temperature, the blue line is the analytical solution of average temperature inside the containment, the dotted black line is transient temperature in R-SG12 zone predicted by COCOSYS, and the dotted red line is CFX predicted average temperature of R-SG12 zone. A relative good agreement is obtained among the analytical solutions, COCOSYS

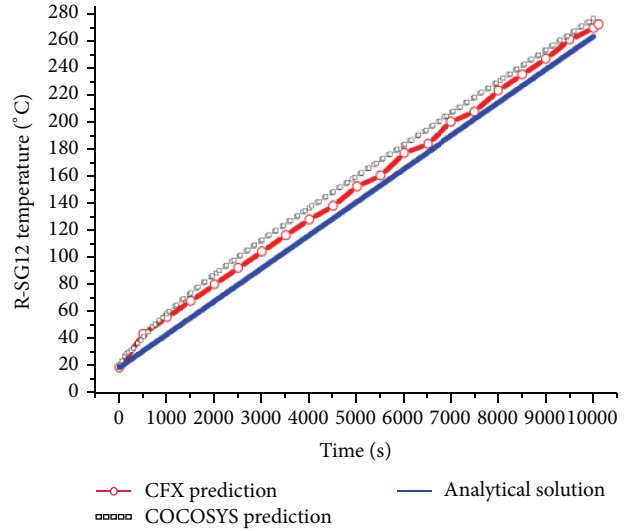


FIGURE 3: Comparison of zone temperature at transient state.

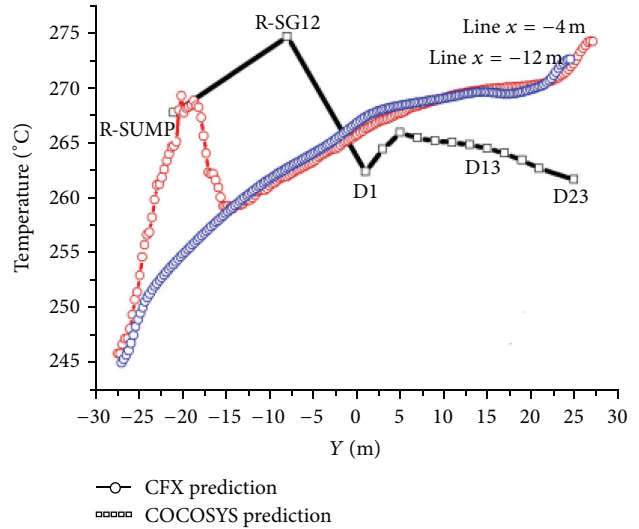


FIGURE 4: Comparison of temperature distribution at 10106 s.

predicted results, and the CFX predicted results. Figure 4 gives the comparisons of the temperature distribution along the vertical direction inside the containment at 10,106 s. There are 14 layers (R-SUMP, R-SG12, D1, D3, D5, D7, D9, D11, D13, D15, D17, D19, D21, and D23) in COCOSYS model (Figure 2), so 14 points are used for plotting the COCOSYS predicted data (black line in Figure 4).

Two vertical lines (*x* = -4 m and *x* = -12 m in Figure 1) are taken in CFX model to represent the 14 layers' zones in COCOSYS model. It can be seen that near the heat source zone (R-SG12 in COCOSYS, *x* = -4 m in CFX), the temperatures climb up dramatically along the vertical height. It indicates that the general trends of the results for COCOSYS meet an agreement with the CFX prediction (line *x* = -4 m) except in the upper dome.

CFX predictions (line *x* = -4 m and line *x* = -12 m) show that the temperature increases slowly from the height of 3 m

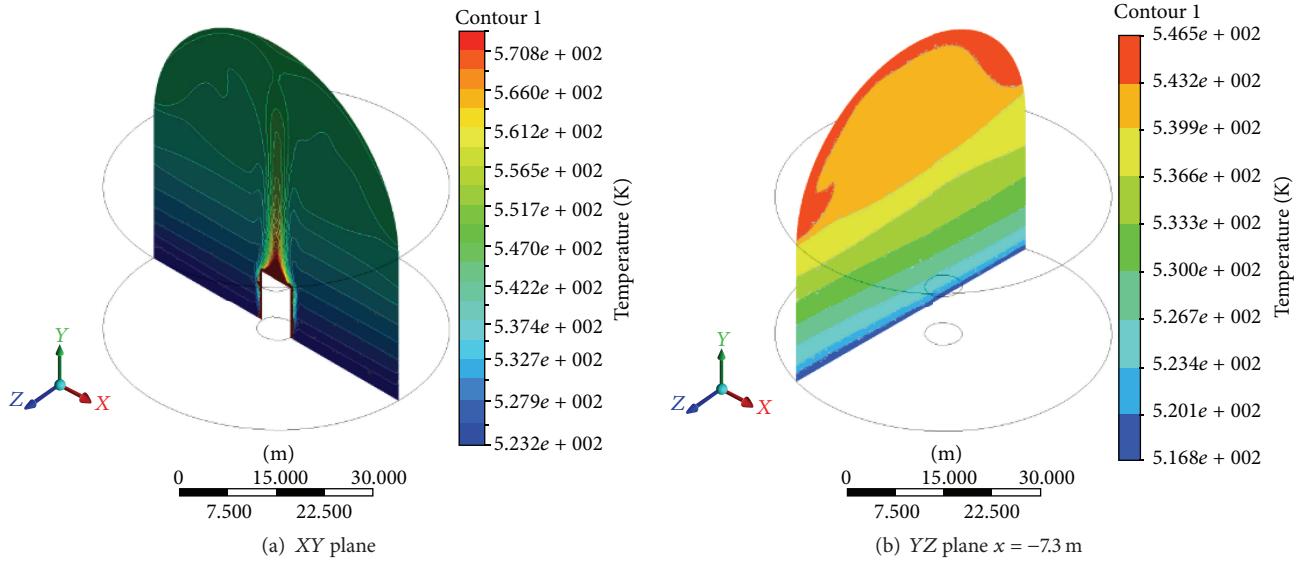


FIGURE 5: Contour plot of the temperature at 10106 s.

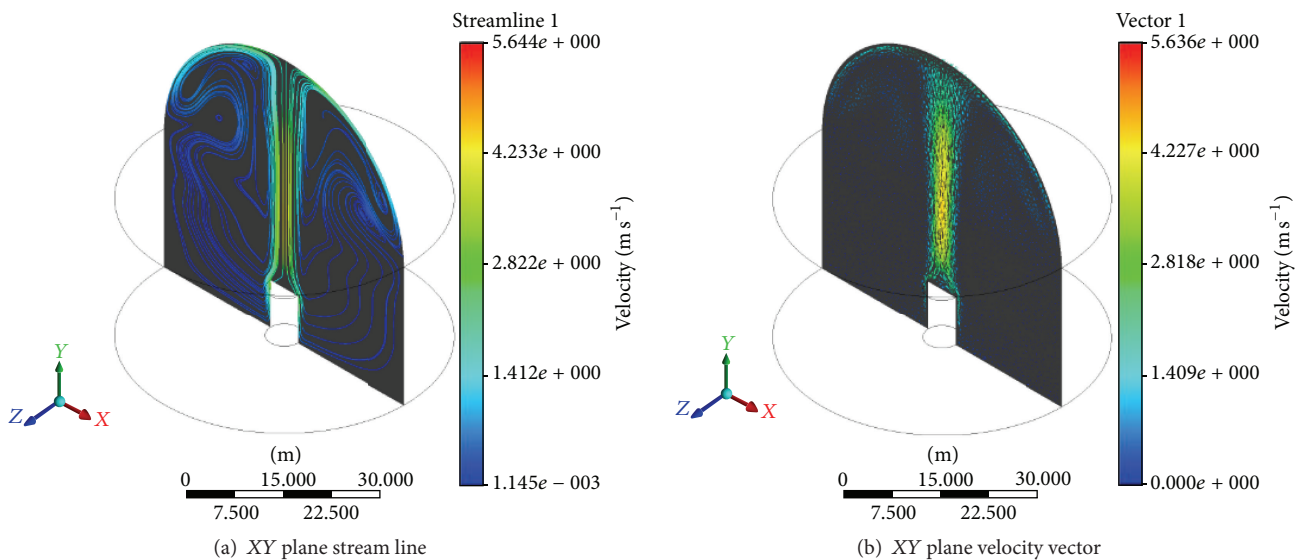


FIGURE 6: Stream lines and velocity vector at 10106 s.

to 25 m and maintains a relatively high temperature, which implies that most energy is stored in the upper region. In the upper part of the containment the temperature increases again due to the shape of the dome in which the heat can be accumulated; these considerations are seen more clearly in terms of temperature contour map (Figure 5). However, from a quantitative view point, discrepancies are observed in the upper dome between CFX and COCOSYS results. The COCOSYS code gives lower temperature values. CFX prediction (line $x = -12$ m) shows that thermal stratification is more pronounced from the height of $y = -23$ m to $y = 0$ m, which can be seen in temperature contour map (Figure 5); COCOSYS cannot predict thermal stratification, because R-SG12 is big control volume using the equilibrium zone model; from the thermodynamic point of view, the volume

temperature is assumed to be mixed homogeneously as zone temperature; the detailed information cannot be obtained from COCOSYS model. The buoyancy-driven flow that arises from the temperature field is presented in Figure 6. It implies that the strong convection areas are in the top of heat source; the weak convection dominant areas are away from the heat source, which suggests an influence of temperature stratification.

It can be seen that the model and boundary conditions are selected symmetric along y -axis, while the contour plot of the temperature (presented in Figure 5) is not very symmetric; the reason is that the symmetric solution breaks down as instabilities grow and the time behaviors of quantities relative to geometrically symmetric points begin to differ; we only presented results at 10,106 s here.

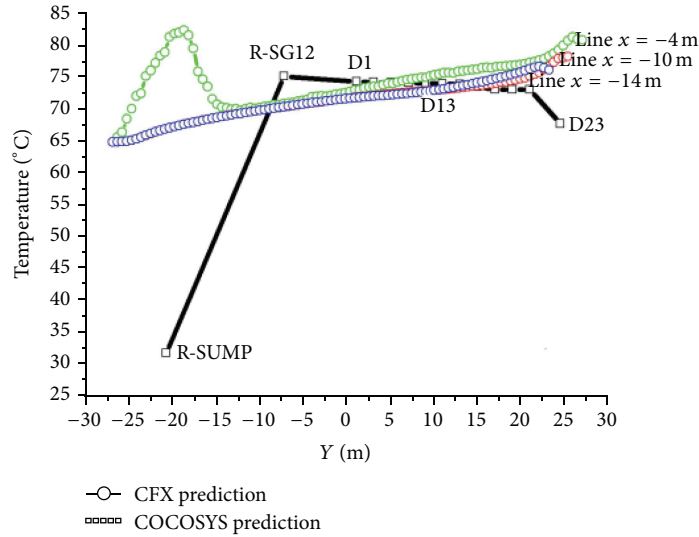


FIGURE 7: Comparison of temperature distribution.

2.3. *Convective Case.* For the sake of ensuring the comparability between CFD and COCOSYS, the following should be mentioned here:

- (1) The size of the system under consideration makes the computations very time-consuming. The running time (or CPU time) is in the range of 2 months per run to reach thermal equilibrium with CFD if the convective heat transfer coefficient is about $10 \text{ W}/(\text{m}^2 \cdot ^\circ\text{C})$; this large computational overhead strongly limited the scope of analyses. So, here, both COCOSYS and CFD have the same outside convective heat transfer coefficient $100 \text{ W}/(\text{m}^2 \cdot ^\circ\text{C})$. Steady state results are compared for COCOSYS CFX model.
- (2) In order to eliminate the wall dynamic inertia delay, measures of higher structure conductivity, lower density, and heat capacity are taken in COCOSYS. Thin shell and plate model with ignoring wall thickness are used in CFD to separate containment enclosure and environment, while it affects the dynamic process, but the steady state will not be affected principally.

There are 14 layers (R-SUMP, R-SG12, D1, D3, D5, D7, D9, D11, D13, D15, D17, D19, D21, and D23) in COCOSYS model, so 14 points are used for plotting the COCOSYS predicted data (Figure 2).

Three vertical lines ($x = -4 \text{ m}$, $x = -10 \text{ m}$, and $x = -14 \text{ m}$ in Figure 1) are taken in CFX model to represent the 14 layers zones in COCOSYS model (Figure 2).

Comparisons of right part zones between COCOSYS prediction and CFX prediction are shown in Figure 7.

It can be readily seen that near the heat source zone (R-SG12 in COCOSYS, $x = -4 \text{ m}$ in CFX), the temperatures increase rapidly along the vertical height. The COCOSYS predicted results from zone D1 to zone D21 are similar to the results from CFX; D23 temperature decreasing shown in Figure 7 near the wall can be predicted by COCOSYS. But

the increasing feature of temperature in the dome predicted by CFX cannot be predicted by COCOSYS.

CFX predictions (line $x = -4 \text{ m}$, line $x = -10 \text{ m}$, and line $x = -14 \text{ m}$) show that the temperature increases slowly from the height of 3 m to 25 m and maintains a relatively high temperature, which implies that most energy is stored in the upper region. In the upper part of the containment the temperature increases again due to the shape of the dome in which the heat can be accumulated. It is apparent to observe from temperature contour map in Figure 8 that the temperature decreases near the wall of the dome, these considerations are seen more clearly in terms of plane contour map, and the reason is that the outside wall is convection boundary condition.

CFX predictions (line $x = -10 \text{ m}$ and line $x = -14 \text{ m}$) show that thermal stratification is more pronounced from $y = -23 \text{ m}$ to $y = 0 \text{ m}$, which can be seen in temperature contour map (Figure 8); COCOSYS cannot predict thermal stratification, because R-SG12 is big control volume using the equilibrium zone model; the volume temperature is assumed to be mixed homogeneously as zone temperature from the thermodynamic point of view; the detailed information cannot be obtained from COCOSYS model.

This feature can be verified from the comparison of horizontal temperature distribution for the zones of R-ANN12, SG12, SG34, and R-ANN34 (Figure 9(a)) and the zones of D45, D1, D2, and D46 (Figure 9(b)), the dotted red line is the CFX prediction result, and the black line is the COCOSYS prediction result; the maximum temperature distribution is very well predicted by the CFX, which would be complicated to simulate using COCOSYS; the use of the COCOSYS led to somewhat less accurate results.

On the other hand, the horizontal line along X direction shows that there is no change of the temperature except in region near the thermal plume and boundary wall region.

From Figure 10, it can be seen that the buoyant convection flow is strong on the upper surface of heat source, indicating

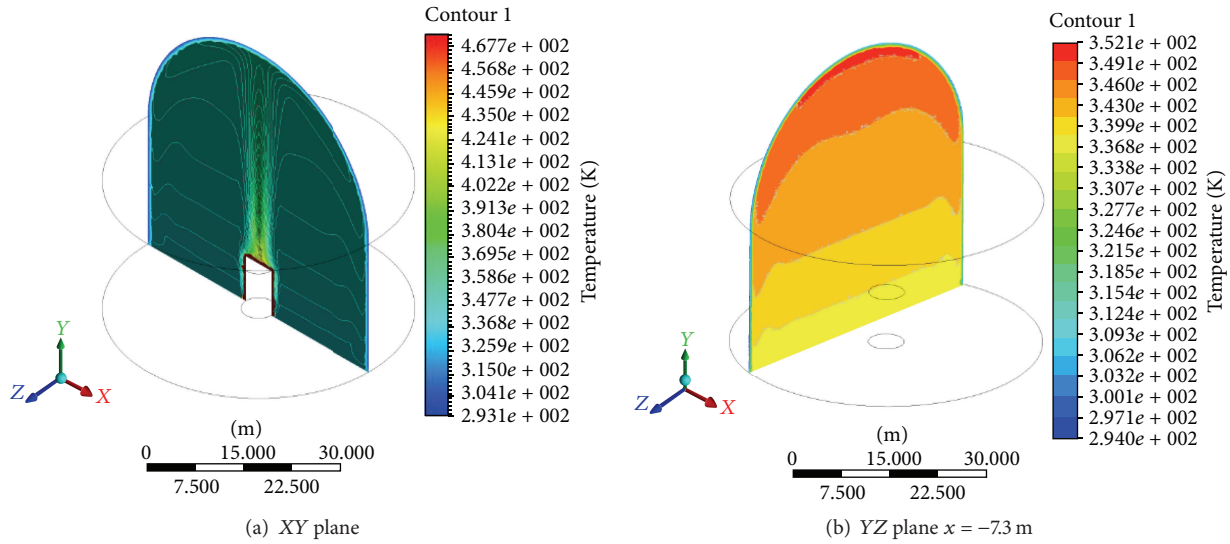


FIGURE 8: Contour plot of the temperature.

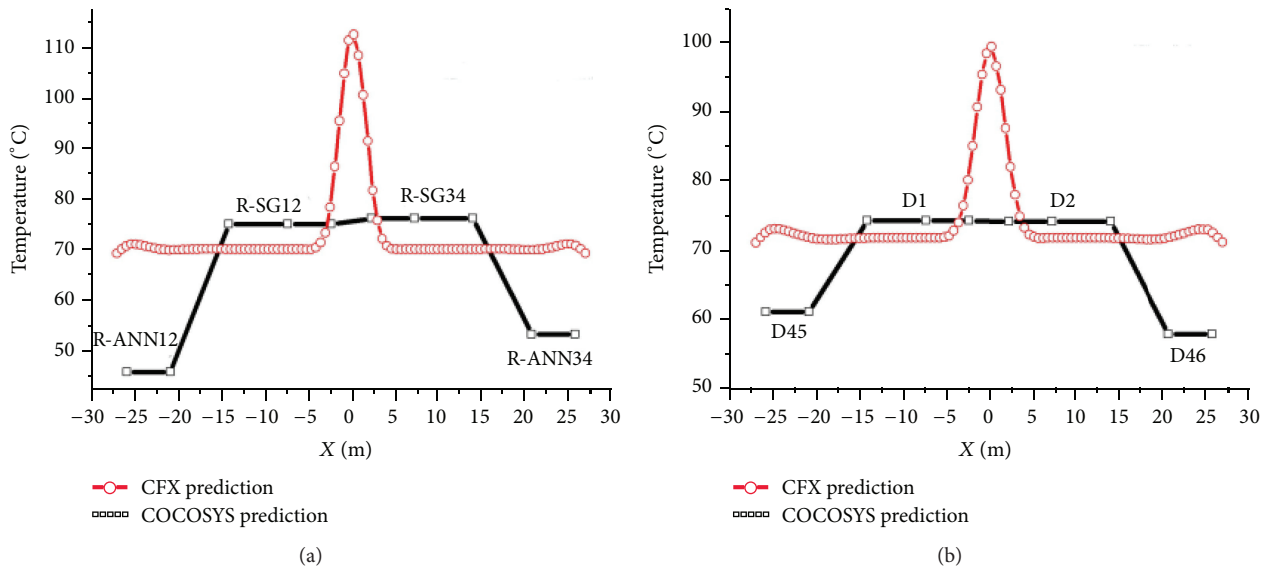


FIGURE 9: Horizontal temperature distribution.

the strong effect of the natural convection; the weak convection dominant areas are in the two sides of heat source, which suggests an influence of temperature stratification.

For comparison purpose of two boundary conditions, the flow configurations and temperature profiles are different; from Figure 11, it is worth noting that thermal stratification area under convection boundary is smaller than that under the adiabatic boundary. When strongly stratified, enclosure's ambient temperature can be considered one-dimensional, with negligible horizontal gradients except in narrow regions beside the boundary and heat source; on the other hand, there is no thermal stratification area inside the dome area.

3. Conclusion

Main conclusions for separate-effect plume (due to a heat source) simulation between COCOSYS and CFX can be summarized as follows.

Temperature in the upper part of the enclosure is higher for both adiabatic and convection boundary condition; this can be predicted by both COCOSYS and CFX.

Convection intensity affects concentration and temperature stratification; both COCOSYS and CFX can predict that there is no temperature stratification in the upper region of enclosure. Temperature stratification exists in the lower

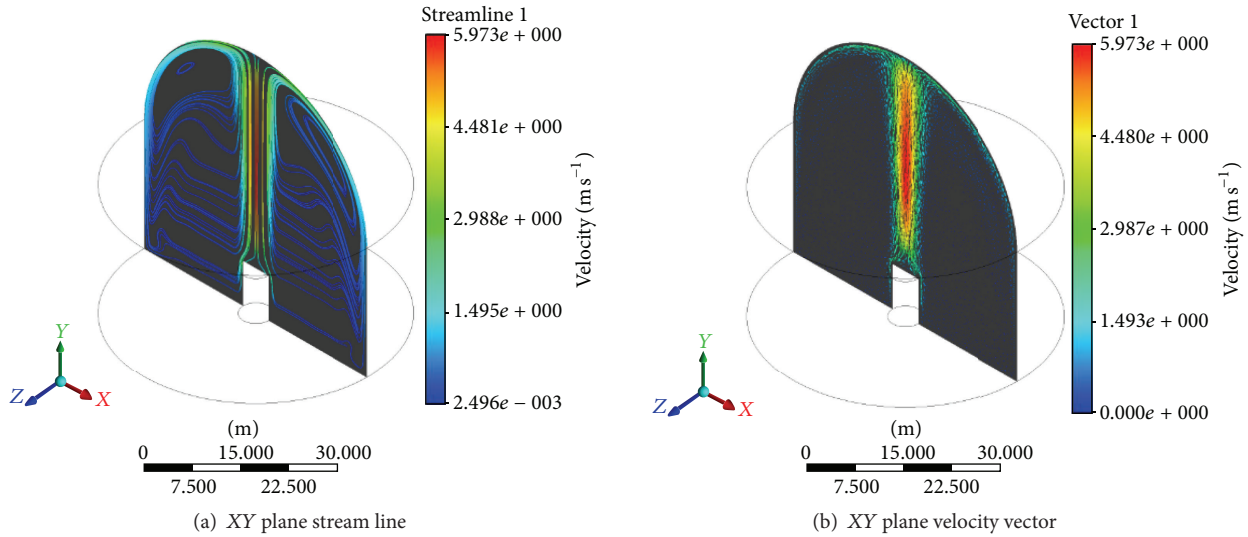


FIGURE 10: Stream lines and velocity vector.

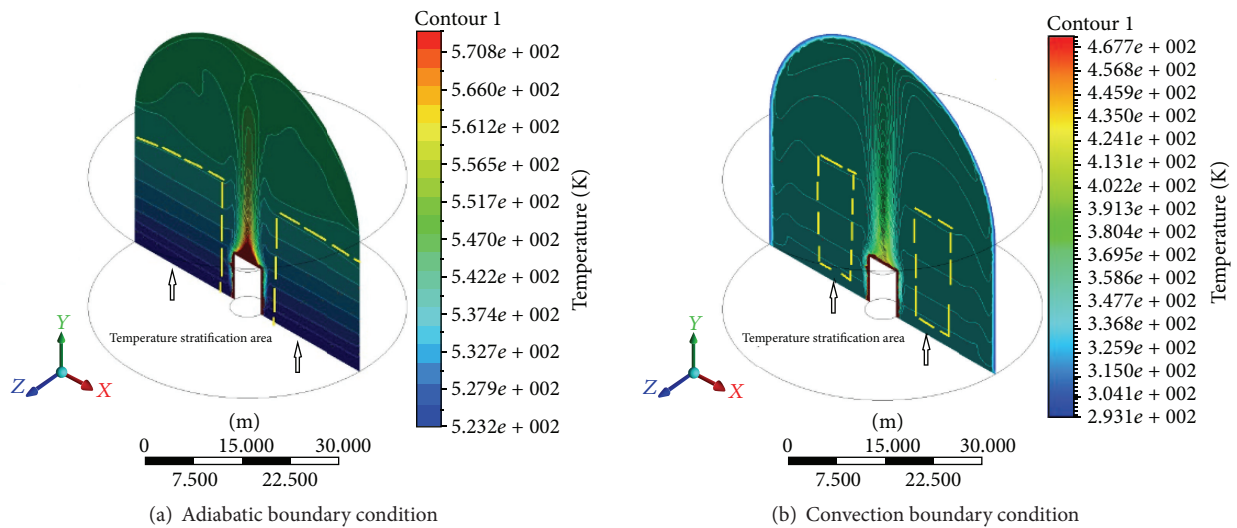


FIGURE 11: Comparison of thermal stratification area.

region of enclosure except in the region near the thermal plume.

Boundary condition affects the temperature stratification. Temperature stratification area under adiabatic boundary condition is bigger than the area under convection boundary condition; CFX are able to predict this phenomenon; however, COCOSYS are not able to predict this phenomenon.

CFX can predict local temperature of thermal plume, while COCOSYS cannot predict local temperature of thermal plume at present nodalisation.

Boundary condition affects the predicted average temperature. The average temperature in enclosure predicted by COCOSYS is overestimated compared to that predicted by CFX under the same adiabatic boundary condition; the average temperature in enclosure predicted by COCOSYS is

underestimated compared to that predicted by CFX under the convection boundary condition.

Competing Interests

The authors declare that they have no competing interests.

Acknowledgments

This work is supported by the National Science Foundations of China (51176132). The corresponding author gratefully acknowledges the support of K. C. Wong Education Foundation and DAAD. The corresponding author is approved to use COCOSYS code in KIT Germany.

References

- [1] W. Breitung and P. Royl, "Procedure and tools for deterministic analysis and control of hydrogen behavior in severe accidents," *Nuclear Engineering and Design*, vol. 202, no. 2-3, pp. 249–268, 2000.
- [2] B. R. Sehgal, "Stabilization and termination of severe accidents in LWRs," *Nuclear Engineering and Design*, vol. 236, no. 19–21, pp. 1941–1952, 2006.
- [3] J. Xiao and J. R. Travis, "How critical is turbulence modeling in gas distribution simulations of large-scale complex nuclear reactor containment?" *Annals of Nuclear Energy*, vol. 56, pp. 227–242, 2013.
- [4] N. Agrawal, A. Prabhakar, and S. K. Das, "Hydrogen distribution in nuclear reactor containment during accidents and associated heat and mass transfer issues—a review," *Heat Transfer Engineering*, vol. 36, no. 10, pp. 859–879, 2014.
- [5] S. Mizokami, D. Yamada, T. Honda, D. Yamauchi, and Y. Yamanaka, "Unsolved issues related to thermal-hydraulics in the suppression chamber during Fukushima Daiichi accident progressions," *Journal of Nuclear Science and Technology*, vol. 53, no. 5, pp. 630–638, 2016.
- [6] D. Paladino, M. Andreani, R. Zboray, and J. Dreier, "Toward a CFD-grade database addressing LWR containment phenomena," *Nuclear Engineering and Design*, vol. 253, pp. 331–342, 2012.
- [7] A. Dutta, I. Thangamani, V. Shanware et al., "Experiments and analytical studies related to blowdown and containment thermal hydraulics on CSF," *Nuclear Engineering and Design*, vol. 294, no. 1, pp. 233–241, 2015.
- [8] M. Povilaitis, T. Kačėgavičius, and E. Urbonavičius, "Simulation of the ICE P1 test for a validation of COCOSYS and ASTEC codes," *Fusion Engineering and Design*, vol. 94, no. 1, pp. 42–47, 2015.
- [9] I. Kljenak, M. Kuznetsov, P. Kostka et al., "Simulation of hydrogen deflagration experiment—benchmark exercise with lumped-parameter codes," *Nuclear Engineering and Design*, vol. 283, pp. 51–59, 2015.
- [10] M. Hashim, Y. Ming, and A. S. Ahmed, "Review of severe accident phenomena in LWR and related severe accident analysis codes," *Research Journal of Applied Sciences, Engineering and Technology*, vol. 5, no. 12, pp. 3320–3335, 2013.
- [11] D. C. Visser, N. B. Siccama, S. T. Jayaraju, and E. M. J. Komen, "Application of a CFD based containment model to different large-scale hydrogen distribution experiments," *Nuclear Engineering and Design*, vol. 278, pp. 491–502, 2014.
- [12] St. Kelm, M. Klauck, S. Beck et al., "Generic containment: detailed comparison of containment simulations performed on plant scale," *Annals of Nuclear Energy*, vol. 74, pp. 165–172, 2014.